

# Rotary shear experiments on glass bead aggregates:

Stick-slip statistics  
and parallels with natural seismicity

Evangelos Korkolis

Utrecht Studies in Earth Sciences  
No. 195

Members of the thesis committee:

**Prof. dr. Emily Brodsky**

Department of Earth and Planetary Sciences  
University of California, Santa Cruz  
Santa Cruz, California, United States of America

**Dr. Cristiano Collettini**

Dipartimento di Scienze della Terra, Sapienza - Università di Roma  
Rome, Italy

**Prof. dr. Karin Dahmen**

Department of Physics, University of Illinois at Urbana-Champaign  
Urbana, Illinois, United States of America

**Prof. dr. Karen Daniels**

Department of Physics, North Carolina State University  
Raleigh, North Carolina, United States of America

**Prof. dr. William Ellsworth**

Department of Geophysics, Stanford University  
Stanford, California, United States of America

This study was conducted at the High Pressure and Temperature  
Laboratory, and the Seismology Group at the Department of Earth Sciences,  
Utrecht University, Utrecht, The Netherlands

This study was funded by the European Research Council

Printed by: Ipskamp Printing B.V.

© 2019 Evangelos Korkolis

ISBN/EAN: 978-90-6266-553-2

Cover sketch (by Luuk Hunfeld):

Characteristic and Gutenberg-Richter quake size distributions. Both types can be produced in the laboratory (Chapter 5), but which one is the most appropriate to describe natural seismicity?

Cover design: Margot Stoete

**Rotary shear experiments  
on glass bead aggregates:  
Stick-slip statistics  
and parallels with natural seismicity**

**Rotatie-schuifexperimenten  
op aggregaten van glas korrels:  
Stick-slip statistieken  
en parallellen met natuurlijke seismiciteit**  
(met een samenvatting in het Nederlands)

**Proefschrift**

ter verkrijging van de graad van doctor aan de  
Universiteit Utrecht  
op gezag van de  
rector magnificus, prof.dr. H.R.B.M. Kummeling,  
ingevolge het besluit van het college voor promoties  
in het openbaar te verdedigen op  
woensdag 9 oktober 2019 des ochtends te 10.30 uur

door

**Evangelos Korkolis**

geboren op 24 maart 1986  
te Athene, Griekenland



**Promotoren:**

Prof. dr. C.J. Spiers

Prof. dr. J.A. Trampert

**Copromotor:**

Dr. A.R. Niemeijer

Dit proefschrift werd mogelijk gemaakt met financiële steun van de Europese Onderzoeksraad (European Research Council)



# Contents

<b>Summary</b>	<b>xi</b>
<b>Samenvatting</b>	<b>xiii</b>
<b>1 Introduction</b>	<b>1</b>
1.1 Phenomenology of seismicity . . . . .	2
1.2 Geological and mechanical considerations for brittle deformation in the lithosphere . . . . .	6
1.3 Can we assess seismic hazard? . . . . .	8
1.4 Beyond consensus phenomenology: the case of waiting times . .	10
1.5 Modeling seismicity as a complex system . . . . .	12
1.6 This work . . . . .	14
<b>2 Stick-slip statistics from large displacement granular friction experiments</b>	<b>17</b>
2.1 Abstract . . . . .	17
2.2 Introduction . . . . .	17
2.3 Methods . . . . .	20
2.3.1 Sample material . . . . .	20
2.3.2 Rotary Apparatus (RAP) . . . . .	20
2.3.3 Experimental procedure . . . . .	21
2.3.4 Data processing . . . . .	23
2.4 Results . . . . .	28
2.4.1 Mechanical behavior . . . . .	28
2.4.2 Distribution of AE sources . . . . .	30
2.4.3 Juxtaposing mechanical and AE data . . . . .	30
2.4.4 Distributions of AE properties and stress drops . . . . .	33
2.4.5 Post-mortem observations . . . . .	38
2.5 Discussion . . . . .	40
2.5.1 What do the estimated AE source locations represent? .	40

2.5.2	Influence of sample thickness evolution on AE productivity	41
2.5.3	Implications for granular micromechanics . . . . .	41
2.5.4	Comparison with seismicity . . . . .	42
2.6	Conclusions . . . . .	44
<b>3</b>	<b>Spatiotemporal correlations of granular avalanches revealed by recurrence time distributions</b>	<b>47</b>
3.1	Abstract . . . . .	47
3.2	Introduction . . . . .	48
3.3	Methods . . . . .	50
3.4	Results . . . . .	52
3.5	Discussion . . . . .	56
3.6	Conclusions . . . . .	62
3.7	Supplementary material . . . . .	64
3.7.1	Details about the statistical treatment of the data . . .	64
3.7.2	Examples of fitting the Corral distribution . . . . .	65
3.7.3	Reproducibility of RT distributions . . . . .	67
3.7.4	RT distributions of slices . . . . .	71
3.7.5	Controlling the torsional stiffness of the apparatus . . .	73
<b>4</b>	<b>Influence of pore water and shear configuration on the mechanical behavior of glass bead aggregates</b>	<b>75</b>
4.1	Abstract . . . . .	75
4.2	Introduction . . . . .	76
4.3	Methods . . . . .	78
4.4	Results . . . . .	79
4.5	Discussion . . . . .	84
4.6	Conclusion . . . . .	90
<b>5</b>	<b>A laboratory perspective on the Gutenberg-Richter and Characteristic Earthquake models</b>	<b>91</b>
5.1	Abstract . . . . .	91
5.2	Introduction . . . . .	92
5.3	Methods . . . . .	94
5.4	Results . . . . .	98
5.5	Discussion . . . . .	107
5.6	Conclusions . . . . .	114
5.7	Supplementary material . . . . .	115

<b>6</b>	<b>Concluding remarks and outlook</b>	<b>117</b>
6.1	Key findings . . . . .	117
6.2	Contribution to understanding natural seismicity . . . . .	120
6.3	Improvements and suggestions . . . . .	121
6.3.1	Apparatus improvements . . . . .	121
6.3.2	Method improvements . . . . .	122
6.3.3	Suggestions for further research . . . . .	124
	<b>References</b>	<b>127</b>
	<b>Acknowledgements</b>	<b>143</b>
	<b>Curriculum Vitae</b>	<b>145</b>



# Summary

The goal of predicting earthquakes remains elusive despite decades of instrumental observations and research, and a much longer historical record. Even the practice of seismic hazard analysis is a topic of heated debate, in part due to our inability to accurately determine the rate and size distribution of earthquakes that a fault can produce. The main reason for these deficiencies is the lack of a validated, physics-based theory of earthquakes. Heuristic attempts to discover patterns in seismicity based on its phenomenology have produced ambiguous and sometimes contradicting results, due to the relatively short instrumental record of big earthquakes compared to their rate of occurrence.

From a geodynamics perspective, earthquakes are bursts of energy release as the lithosphere is loaded due to the motion of tectonic plates at rates of a few centimeters per year. Similar behavior, known as crackling, is observed when shearing granular aggregates. Loosely packed particles behave collectively as a fluid, giving rise to small instabilities only. At a critical packing fraction, the size distribution of the instabilities approaches power law scaling. This suggests that the aggregate is at a phase transition and that long-range correlations are a key characteristic of its macroscopic behavior. Above the critical packing fraction, the collective behavior of the particles is similar to that of a solid. In that solid-like regime, the aggregates alternate between power law distributed event sizes and quasi-periodic stick-slip. A significant number of laboratory studies have employed granular media to explore the dynamics of critical systems in the context of seismicity and fault gouge rheology. These studies have been performed either at low normal stress ( $< 1$  MPa) or to limited shear displacements ( $< 50$  mm), and often under dry conditions. It is not known whether the macroscopic behavior of granular aggregates remains the same under higher normal stress and larger displacements, or in the presence of pressurized water. If not, is it possible to determine what mechanisms are responsible for the change?

The rotary shear experiments presented in this thesis expand the envelope of the experimentally tested conditions up to 8 MPa normal stress and 165 mm

of shear displacement, *simultaneously*. This enabled us to infer the emergence of correlations under these conditions, through changes in the statistics of granular avalanches. Because the elevated stress conditions do not allow direct visual observation of the glass bead samples, a specially developed AE monitoring system was used to detect and locate the source of crackling. Chapter 2 describes the apparatus and the methods used and discusses the reproducibility of stick-slip statistics. Chapter 3 is devoted to the study of waiting time (WT) distributions of AE events. It is shown that the rescaled WT data can be fit by a gamma distribution, whose power law exponent is positively correlated with normal stress. The gamma fit implies the existence of correlations between AE (and thus slip) events, while the positive correlation between normal stress and the shape of the gamma distribution suggests that the rescaled WTs are sensitive to changes in the rigidity of the load-bearing framework of the aggregate. Chapter 4 demonstrates that the mechanical behavior of the glass bead aggregates changes dramatically in the presence of pressurized pore water, likely due to subcritical cracking. This means that soda-lime glass beads and water are not a suitable combination to investigate purely mechanical effects of pore fluid pressure and effective normal stress, nor is the addition of water a recommended way to control sample humidity. Chapter 5 shows that it is possible to generate quasi-periodic events or power law crackling by choosing an appropriate particle size distribution. The system can spontaneously transition between these two regimes. This implies that faults may be inherently capable of either mode of slip (quasi-periodic or power law distributed) and that short periods of observation, that are comparable to the recurrence interval of big earthquakes, could greatly bias our assessment of their seismic potential.

The findings of this thesis highlight the importance of emergent, long range correlations in sheared granular media, as a function of experimental conditions. We infer that the key parameter that determines the scaling of avalanche statistics is the packing fraction, which in turn depends on normal stress, wear rate, and particle size distribution.



# Samenvatting

Het kunnen voorspellen van aardbevingen blijft een moeilijk te bereiken doel, ondanks tientallen jaren aan observatie via meetinstrumenten en onderzoek, en een nog veel langere historische registratie. Seismische gevarenanalyse is onderwerp van verhitte discussie, mede door ons onvermogen om accuraat te kunnen vaststellen wat de frequentie en grootte-verdeling van aardbevingen is die een breuk kan voortbrengen. De voornaamste reden voor deze tekortkomingen is het gebrek aan een gevalideerde, op fysica gebaseerde theorie van aardbevingen. Heuristische pogingen tot het ontdekken van patronen in seismiciteit hebben dubbelzinnige en soms tegenstrijdige resultaten opgeleverd, voornamelijk door de relatief korte meetperiode in vergelijking met het herhalingsinterval van grote aardbevingen.

Vanuit geodynamisch oogpunt komt tijdens een aardbeving plotseling energie vrij, die in de lithosfeer wordt opgebouwd als gevolg van toenemende spanningen door de beweging van tektonische platen. Deze platen bewegen ten opzichte van elkaar met een snelheid van enkele centimeters per jaar. Vergelijkbaar gedrag, bekend als “geknetter” (crackling noise), wordt waargenomen wanneer korrelaggregaten worden afgeschoven. Een losse pakking van deeltjes (korrels) gedraagt zich collectief als een vloeistof, waarbij alleen kleine instabiliteiten ontstaan. Bij een kritieke pakkingsdichtheid benadert de grootte-verdeling van de instabiliteiten die van een schaalverdeling volgens een machtsfunctie. Dit suggereert dat het aggregaat zich op een faseovergang bevindt en dat het macroscopisch gedrag wordt gekarakteriseerd door ruimtelijk en temporeel gecorreleerde instabiliteiten. Boven deze kritische pakkingsdichtheid is het collectieve gedrag van de deeltjes vergelijkbaar met dat van een vast medium, waarin de verdeling van instabiliteiten wisselt tussen een machtsfunctie en quasi-periodieke stick-slip. In laboratoriumonderzoek wordt veelal gebruik gemaakt van granulaire media (korrelaggregaten) om de dynamiek van instabiele systemen te bestuderen in de context van seismiciteit en de reologie van breukgesteente (breukmeel). Deze studies zijn uitgevoerd onder

lage normaalspanning ( $<1$  MPa) of met kleine schuifverplaatsingen ( $<50$  mm), veelal onder droge condities. Het is tot op heden onbekend of het macroscopische gedrag van zulke korrel-aggregaten hetzelfde blijft onder hogere normaalspanning en grotere verplaatsingen, of in aanwezigheid van water op een bepaalde druk. Zo niet, is het dan mogelijk om te bepalen welke processen voor deze verandering zorgen?

De rotatie-schuifexperimenten die in dit proefschrift gepresenteerd worden, vergroten het bereik van de experimenteel onderzochte condities *gelijktijdig* naar 8 MPa normaalspanning en 165 mm schuifverplaatsing. Dit heeft ons in staat gesteld om de correlaties die onder deze condities beginnen te ontstaan af te leiden uit veranderingen in de statistieken van de instabiliteiten. Door het toepassen van deze verhoogde normaalspanningen was directe observatie van de glaskorrelaggregaten tijdens de experimenten onmogelijk. In plaats daarvan is er gebruik gemaakt van een speciaal ontworpen akoestische-emissie (AE) meetsysteem om het geknetter te detecteren en te lokaliseren. Hoofdstuk 2 beschrijft de experimentele opstelling en methodes, en de reproduceerbaarheid van de instabiliteit-statistieken. Hoofdstuk 3 is gewijd aan de verdeling van herhalingstijd in AEs. Er wordt aangetoond dat de herhalingstijd data beschreven kan worden door een gamma-verdeling waarbij de exponent van de machtsfunctie positief correleert met de normaalspanning. De overeenkomst met deze gamma-verdeling impliceert dat de akoestische emissies (en dus lokale verplaatsingen) gecorreleerd zijn. De positieve correlatie tussen normaalspanning en de vorm van de gamma-verdeling suggereert dat de (geschaalde) herhalingstijden gevoelig zijn voor verandering in de stijfheid van de spanning-dragende structuur binnen het aggregaat. Hoofdstuk 4 laat zien dat het mechanisch gedrag van de glaskorrelaggregaten drastisch verandert wanneer water (op druk) als poriënvloeistof aanwezig is, waarschijnlijk als gevolg van sub-kritieke breukvorming in de korrels. Dit betekent dat sodakalkglaskorrels en water niet de juiste combinatie is om de mechanische effecten van porievloeistofdruk en effectieve normaalspanning te onderzoeken. Daarnaast is het toevoegen van water als middel om het vochtgehalte van het aggregaat te controleren, niet aan te raden. Hoofdstuk 5 laat zien dat het mogelijk is om instabiliteiten te generen die of quasi-periodiek optreden, of verdeeld zijn volgens een machtsfunctie, door de juiste korrelgrootteverdeling te kiezen. Het systeem kan spontaan wisselen tussen deze twee vormen van instabiliteit. Dit impliceert dat breuken van nature in staat zijn tot beide vormen van episodische verplaatsing (quasi-periodiek of verdeeld volgens een machtsfunctie). Om die reden kunnen korte periodes van observatie,

vergelijkbaar met het herhalingsinterval van grote aardbevingen, een verkeerd beeld geven van hun seismische potentie.

De bevindingen van dit proefschrift benadrukken het belang van interne correlaties in ruimte en tijd tussen instabiliteiten die zich ontwikkelen bij afschuiving van granulaire media. Deze correlaties zijn gevoelig voor de toegepaste experimentele condities. Wij leiden hieruit af dat de pakkingsdichtheid de belangrijkste parameter is die de schaalverandering van de instabiliteitsstatistieken bepaalt, welke op zijn beurt afhangt van de normaalspanning, de mate van slijtage van de korrels, en de korrelgrootteverdeling.

*(translated from the original by Luuk Hunfeld and Tim Wolterbeek)*



# Chapter 1

## Introduction

Our planet, Earth, is a complex system. Complex systems are those whose macroscopic behavior is the outcome of the nonlinear interactions between its constituent parts. Certain facets of complexity on Earth are familiar to most people, even non-specialists: the prime example is weather, a phenomenon that arises from the interaction of various agents in the earth's surface and the atmosphere above it. Another example is seismicity, i.e. the occurrence of earthquakes. For the lay person, earthquakes are simply the characteristically unpleasant, occasionally damaging and sometimes lethal shaking of the earth's surface due to deformation of the lithosphere. The lithosphere is fragmented into several closely packed tectonic plates. Because the latter are constantly in motion relative to each other (Turcotte and Schubert, 2002), they deform both at the edges as well as internally, just like two springs that are pressed slowly against each other, all the while storing elastic energy. When there is sudden slip at the interface with a neighboring plate, or when part of the plate itself breaks thereby creating a "fault", a portion of the elastic energy is released in the form of elastic waves. When these waves eventually reach the surface and shake the ground they are felt by us or recorded by seismometers as earthquakes.

Just like extreme weather, "extreme" earthquakes can cause problems for society in a variety of ways. They can damage or destroy infrastructure by shaking, or by inducing landslides, liquefaction, and tsunamis. They can also be detrimental to individuals and societies by inducing fear, panic, injury, and death. Relevant statistics for casualties and economic losses can be found in Snieder and van Eck (1997). It is therefore desirable to predict the occurrence of such events. Here prediction means knowledge of an earthquake's origin time, location and magnitude prior to its occurrence. Useful predictions for society would be those that have relatively small uncertainties associated with

the parameters of interest. Predictions would be most robust if they were based on complete knowledge of the mechanisms that generate seismicity, as well as complete knowledge of the values of the relevant variables (e.g. stress, temperature, mineral composition) everywhere in the lithosphere. However, the lithosphere is not nearly as accessible for observation and sampling as the atmosphere is in the weather example, because it is solid, opaque, and has vast volume; it is roughly 50 to 150 km thick, depending on geographic location. For comparison, the deepest borehole ever drilled stopped at approximately 12 km below ground level, in Kola Peninsula, Russia. Therefore, the “generating model” of earthquakes is not well understood (epistemic uncertainties), and the full state of the system, as a function of time cannot be fully measured (aleatory uncertainties); (Stein and Friedrich, 2014). This means that the ideal scenario of complete knowledge of the physical mechanisms and the state of the lithospheric system is currently not feasible and will likely remain so in the foreseeable future. Because of this, we are forced to use other approaches to study seismicity and to try to project its occurrence in the future as best as we can. Before we discuss such approaches it is useful to introduce the phenomenology of natural earthquakes, i.e. what is known about seismicity based on historical and instrumental records. This will be followed by a discussion of relevant mechanical considerations and geological evidence about deformation in the lithosphere. In this chapter we do not consider earthquakes generated by volcanic activity, collapse of underground caves, meteor impacts, and human activities such as mining, drilling and nuclear explosions, unless explicitly stated.

## 1.1 Phenomenology of seismicity

Seismology is, to a significant degree, observational and data-driven. The basic laws of earthquake occurrence are empirical and were established after the advent of seismometers in the dawn of the 20th century. They are the following: the Gutenberg-Richter law of frequency-magnitude distribution, the Omori-Utsu law of aftershock decay, Båth’s law for the maximum magnitude of an aftershock, and Aki’s scaling law for seismic spectra (Fowler, 2004; Madariaga, 2009; Scholz, 2002; Utsu, 2002). Because of their empirical nature, these laws do not reveal the physical mechanisms that produce seismicity, but they certainly constrain what the apparent outcome of the mechanisms’ collective action is. In this section we will discuss observational evidence about the size, location, and frequency of tectonic earthquakes.

The size of an earthquake is typically reported in terms of its “magnitude”. Different types of magnitude exist, such as local ( $M_L$ ), body-wave ( $mB$ ),

surface-wave ( $M_s$ ), and duration ( $M_d$ ). The general formula for magnitude scales is (Fowler, 2004; Bormann, 2012):

$$M = \log_{10}\left(\frac{A}{T}\right) + q(\Delta, h) + c \quad (1.1)$$

where  $M$  is the magnitude,  $A$  is the amplitude, and  $T$  the period of the phase of interest;  $q(\Delta, h)$  is a function that accounts for attenuation as a function of epicentral distance  $\Delta$  and focal depth  $h$ ; and  $c$  is a constant that accounts for seismometer and site response.

Another way to measure the size of an earthquake is by its scalar seismic moment  $M_0$ , assuming a double-couple source mechanism due to unstable slip on the fault plane. Unlike the magnitude types discussed above, seismic moment is a physical quantity related to the seismic source.  $M_0$  can be calculated from the formula (Madariaga, 2009):

$$M_0 = GAD \quad (1.2)$$

where  $G$  is the shear modulus of the rock in the vicinity of the fault,  $A$  is the area of the slip surface and  $D$  is the average amount of slip. These parameters are difficult to estimate, let alone measure, because the majority of faults are buried deep in the lithosphere and are thus inaccessible. Some faults break through the Earth's surface, permitting direct measurement of displacement at those locations. Instead, the seismic moment can be calculated from a seismogram (Bormann, 2012):

$$M_0 = 4\pi d\rho v^3 \frac{u_0}{R} \quad (1.3)$$

Here,  $d$  is the hypocentral distance,  $\rho$  is the average rock density,  $v$  is the wave velocity in the vicinity of the source,  $u_0$  is the amplitude of the flat portion (low frequency) of the displacement spectrum of the seismic source, and  $R$  a correction term for wave radiation. The source spectrum is calculated from the corrected spectrum of the seismogram (Bormann, 2012). The scalar seismic moment can be converted to moment magnitude via the following relationship (Hanks and Kanamori, 1979):

$$M_w = \frac{2}{3}\log_{10}(M_0) - 6 \quad (1.4)$$

where  $M_0$  is measured in Nm. Equation 1.4 shows that a unit increase in moment magnitude results from a 31.6 times increase in seismic moment.  $M_w$  has become the standard scale for reporting the size of significant earthquakes.

What is the distribution of earthquake magnitudes globally and regionally? Data show that the logarithm of the number of earthquakes above a certain

magnitude in an arbitrary region,  $\log_{10}N(M)$ , scales linearly with magnitude,  $M$ , as follows (Kanamori and Brodsky, 2004):

$$\log_{10}N(M) = A - bM \quad (1.5)$$

In the formulation of equation 1.5, which is known as the Gutenberg-Richter (G-R) law,  $A$  is indicative of the amount of seismic activity in the region of interest, and  $b$  describes the relative abundance of small and large earthquakes. It has been found that  $b \approx 1$  for both global and regional seismicity, despite the diversity of tectonic environments around the world (Scholz, 2015). Thus, the G-R law reflects seismological observations that there is a tenfold decrease in the number of earthquakes per unit increase in the magnitude. This reveals the preferred mode of slip in the lithosphere: not by equally sized events but by a distribution that contains much fewer big events than small ones. From equations 1.4 and 1.5 we can see that there is a power law (Pareto) relationship between seismic moment  $M_0$  and  $\log_{10}N(M)$  (Kagan, 1994). The exact shape of the right tail of the distribution is subject to a longstanding debate in the seismological community because of its fundamental implications for how faults slip and the possibility of earthquake prediction. Due to the importance of this topic, we will discuss it in greater detail later in this introduction. Before proceeding to describe other features of seismicity, it is important to remark that power law distributed slip has also been observed in laboratory compression or shear experiments on nanocrystals and microcrystals, bulk metallic glasses, rock samples, and granular media (Uhl et al., 2015) and induced earthquakes in mines (Boettcher and McGuire, 2009). The apparent universality of slip statistics across such vastly different spatial scales is an astonishing observation that keeps drawing the interest of physicists, seismologists, and material scientists alike.

The vast majority of earthquakes occur along the boundaries of tectonic plates. In fact one can delineate rather accurately the boundaries of the tectonic plates by overlaying a map of global seismicity onto the world map (Scholz, 2002). The most common types of plate boundaries are divergent, such as mid-ocean ridges; convergent, such as in the eastern Mediterranean, Japan, Cascadia, and Chile; and transform, such as the San Andreas fault in California, and oceanic fracture zones. Analysis of the source mechanisms of earthquakes shows that, to first order, divergent boundaries are associated with normal faulting, convergent boundaries with thrust faulting, and transform boundaries with strike-slip faulting. In practice, geometrical and mechanical considerations result in diverse mixtures of source mechanisms in each plate boundary. The largest earthquakes recorded to date have occurred in convergent boundaries; they are known as megathrust earthquakes in



subduction zones (Scholz, 2002). The largest event on record is the 1960  $M_w$  9.5 Chile earthquake. Historical and instrumental records of seismicity also contain instances of intraplate earthquakes. Compared to earthquakes in convergent boundaries, big intraplate earthquakes are rare. Nevertheless consideration has to be given to intraplate seismicity for societal reasons, particularly when developing critical infrastructure such as nuclear power plants.

A striking feature of regional seismicity is temporal clustering. Earthquakes tend to occur in sequences that typically contain one big event, often at the very beginning of the sequence, and a number of smaller events, distributed according to the G-R law. The magnitude of the mainshock, i.e. the biggest event in the cluster, is usually about 1.2 units larger than the second biggest event; this observation is known as Båth's law (Shcherbakov et al., 2015). Those events that precede the mainshock are called foreshocks. Events that follow the mainshock are called aftershocks. Data show that the rate of aftershocks,  $n(t)$ , at time  $t$  after the mainshock is given by the formula (Utsu, 2002):

$$n(t) = K(t + c)^{-p} \quad (1.6)$$

where  $K$ ,  $c$ , and  $p$  are empirical constants, with  $p$  between 1 and 1.5. Equation 1.6 is known as the Omori-Utsu law. A number of empirical relationships that link the size of the mainshock with the extent of the aftershock area have been proposed. Aftershocks are thought to occur due to changes in the stress field in the vicinity of the fault that generated the mainshock, that bring nearby faults closer to failure and frictional instability. Foreshock sequences are, perhaps unfortunately, not nearly as common nor as consistent with the Gutenberg-Richter and Omori-Utsu laws, as aftershock sequences. If a cluster of earthquakes does not fit the (foreshock -) mainshock – aftershock paradigm, it is classified as an earthquake swarm.

Conventional seismological wisdom holds that mainshocks occur at a constant rate in a time-independent fashion. In other words, the null hypothesis is that mainshocks in, for example, the eastern Mediterranean region are not related to mainshocks in the Japan trench. This view assumes that the generating model is a Poisson point process (Molchan, 2005) with exponentially distributed waiting times, i.e. the times between consecutive events. The memoryless property of the exponential distribution guarantees that waiting times are independent and thus the only information we have about the process is its average rate (Frank, 2009, 2014). In order to apply the Poisson model to seismicity, earthquake catalogs have to be declustered so that the remaining events are independent (Zaliapin et al., 2008; Zaliapin

and Ben-Zion, 2013). Various methods exist to decluster catalogs, but their effectiveness and indeed the practice of declustering itself have been criticized (Luen and Stark, 2012; Mulargia et al., 2017). Evidence for weak correlations between mainshocks has been presented by Kagan and Jackson (1991a).

To summarize, the well established empirical features of seismicity are the following: 1. the vast majority of earthquakes occur along tectonic plate boundaries, with few intraplate events; 2. catalogs of global and regional seismicity show that event sizes (magnitudes) follow the Gutenberg-Richter law; 3. the aftershock rate follows the Omori-Utsu law. Foreshocks are not as common as aftershocks. By itself, earthquake phenomenology does not reveal the physics behind seismicity, yet it provides constraints for models of the complex system that the lithosphere is.

## 1.2 Geological and mechanical considerations for brittle deformation in the lithosphere

This section describes the current understanding of what causes tectonic earthquakes. For a detailed treatment of the topic see Scholz (2002). As has been mentioned already, earthquakes are the result of localized, unstable, brittle or frictional deformation of the Earth's lithosphere. This deformation is believed to occur under constant loading rate conditions, since the rate of plate motion is assumed to be constant in geologic time. Regardless of regional differences, we can generalize by stating that rocks in the lithosphere are loaded at a slow rate (millimeters to centimeters per year) over periods ranging from tens to millions of years, whereas fault slip associated with big earthquakes may last approximately  $10^1$  to  $10^2$  seconds (Ben-Zion, 2008). Simple mechanical considerations suggest that in the brittle domain, once shear stress exceeds the shear strength of the rock in an arbitrarily small volume of the lithosphere, sudden slip will occur either on a preexisting shear fracture, i.e. a fault, or on a newly formed one. Similarly, the interface between two neighboring tectonic plates can also be considered a fault, and can host slip. Evidence of brittle deformation of the Earth's lithosphere can be found on various geographic locations on the planet's surface.

The view described in the paragraph above has inspired a family of simple earthquake models under the assumption of constant loading rate. Let us consider a single fault in an otherwise homogeneous, infinite volume of rock, that is loaded at a constant rate, under constant confining stress. If the shear stress at failure and the resulting amount of slip are constant, one expects periodic earthquakes of similar size, i.e. characteristic earthquakes (CEs); (Youngs and Coppersmith, 1985). This is known as the uniform cyclic

model which forms the basis of the concept of seismic (or earthquake) cycles. Support, sometimes partial, for the Characteristic Earthquake model comes from a variety of studies (Field et al., 2017; McGuire, 2008; Schwartz and Coppersmith, 1984; Wesnousky, 1994; Williams et al., 2017). There exist two popular variations of the uniform cyclic model (Scholz, 2002). If a variable amount of slip occurs when a fixed shear stress threshold is reached, then one can predict the time of the next earthquake as long as the time and slip of the previous earthquake are known. This is known as the time-predictable model. A second variation of the uniform cyclic model assumes that while the peak shear stress is not fixed, the post-failure residual stress is. This is known as the slip-predictable model, because the slip of the next earthquake can be predicted, assuming the time of the previous one is known.

These conceptual earthquake models can be used to estimate the seismic potential of a region containing one or more faults. This can be achieved via numerical modeling of the frictional strength and stability of individual faults. But which rock types and conditions favor brittle or unstable frictional deformation, i.e. fracture propagation and unstable slip on faults? What portion of the stored elastic energy is converted to elastic waves? How much time does it take for a material to develop or regain its frictional strength? Broadly speaking, answering such questions is necessary to understand the seismic potential of a fault and therefore to put constraints on the location, time, and size of future earthquakes. Since we cannot manipulate the lithosphere itself, answers to such questions have to come from laboratory experiments, by testing the frictional strength and stability of intact rocks and rock-rock interfaces. Because brittle deformation results in abrasive wear and cataclasis, faults are often filled with rock fragments, that are collectively referred to as fault gouge (Chester and Chester, 1998; Engelder, 1974). Therefore, apart from experiments on rocks, it is necessary to evaluate the frictional strength and stability of fault gouges of different compositions and under various conditions.

An open issue is how to upscale laboratory results, that are typically obtained from samples with dimensions in the centimeter scale, to the kilometers and above scale that modeling aims to address. Few laboratory studies on meter scale samples exist; while these constitute about an order of magnitude increase from classic laboratory experiments, they are still several orders of magnitude away from some aspects of natural earthquakes, e.g. rupture length. One way to link the laboratory domain with the domain of natural earthquakes is to study a natural environment where some human control is possible, such as mines (Goodfellow and Young, 2014).

We can generalize, by stating that laboratory experiments are used to

develop constitutive laws for the frictional behavior of fault materials (rocks and gouges), that are in turn used in theoretical and numerical models of faults to provide estimates of their seismic potential. This represents the forward modeling approach to achieving a physics-based understanding of the mechanisms that cause earthquakes.

### 1.3 Can we assess seismic hazard?

We mentioned that epistemic and aleatory uncertainties in our view of the lithosphere imply that a full description of seismicity based on the physical mechanisms operating at every scale is currently infeasible. Therefore, deterministic earthquake prediction is also infeasible at the moment. Another option for short-term forecasting, i.e. hours to weeks, would be the discovery of precursory phenomena. While several possibilities have been proposed, none have been shown to be robust enough for operational use; for reviews see Geller (1997); Stark (1997); Turcotte (1991). Pending the development of a theory of seismicity and the discovery of trusted precursory phenomena, our options are limited to assessments of long-term seismic hazard, i.e. years, decades or more. The ability to produce accurate, long-term forecasts of seismicity is a necessary step toward minimizing the earthquake risk faced by our society. However, is it possible to accurately assess the seismic hazard in a region of interest, based on earthquake phenomenology together with what is currently known about deformation in the lithosphere? The following discussion is focused on seismic sources and their seismic potential only. We do not discuss ground response and its quantification. Reviews of seismic hazard assessment can be found in Bommer (2002); Klügel (2008); Mulargia et al. (2017); Stein et al. (2012); Stirling (2014); Wang (2011).

One way to assess the seismic potential of faults in a geographic region is by estimating the so called “maximum credible magnitude” for every known fault in the area. This approach is used in deterministic seismic hazard analysis (DSHA); (Klügel, 2008; Stein et al., 2012; Wang, 2011). Equations 1.2 and 1.4 show that magnitude is a function of fault dimensions and the amount of seismic slip. The dimensions of a fault could be estimated via geophysical surveying or geological arguments, whereas the possible amount of seismic slip can be constrained using geomechanical experiments and modeling. Overall, the main idea behind DSHA is to estimate seismic hazard for several credible scenarios. This method is typically used in the design phase of critical infrastructure, such as nuclear power plants.

A different and perhaps more popular approach is the probabilistic

assessment of a region's seismic potential (Klügel, 2008; Stein et al., 2012; Stirling, 2014; Wang, 2011). The challenge here is to estimate the probability of occurrence of various earthquake magnitudes. This can be performed in the Poisson process framework, i.e. by assuming that earthquakes occur independent of each other, at a constant average rate. This is known as time-independent (TI) probabilistic seismic hazard analysis (PSHA). A different approach is to make use of the characteristic earthquake model. This is time-dependent (TD) PSHA, since the time to the next earthquake on a particular fault is controlled by the seismic cycle.

The validity of the results of deterministic and probabilistic seismic hazard analyses are subject to epistemic uncertainties. We do not know where all the faults are and what are the prevailing geomechanical, chemical, and hydrological conditions. It is not possible to predict the amount of slip that will occur during the next earthquake on a particular fault. For certain implementations of PSHA in particular, the assumption of the Poissonian generative model is arbitrary; clustering of earthquakes, seemingly periodic events, and evidence of static and dynamic triggering (Hill, 2008; King et al., 1994) suggest that seismicity is correlated. The Characteristic Earthquake model has been criticized for not complying with data showing earthquake clustering and for being outperformed by random chance (Kagan et al., 2012; Rong et al., 2003). At least in some cases it is not possible to determine which model describes the seismicity of a fault using paleoseismological studies, due to the challenges associated with the detection, dating, and correlation of slip events in the geological record (Stein, 1995; Weldon, 2005; Weldon et al., 2004). Earthquakes with multi-fault ruptures, such as the 2016  $M_w$  7.8 Kaikoura event, cast further doubt on the validity of the CE model. In some countries, e.g. Italy and Haiti, national seismic hazard maps were updated after the occurrence of “unexpected”, destructive earthquakes (Stein et al., 2012, 2015). The 2011  $M_w$  9.1 Tohoku earthquake is perhaps the most infamous recent example of an unexpectedly big earthquake. And while seismic activity is common along most plate boundaries, relatively little is known about intraplate seismicity. Regions currently considered aseismic may simply host unknown faults with very long recurrence times. Currently, the length of the earthquake record and the source of information (instrumental seismology, paleoseismology, historical records) heavily affect the way experts estimate seismic potential and the quality of their estimation. Finally, the PSHA practice of treating observed rates of seismicity as probabilities has attracted criticism for being inconsistent with the concept of probability (Mulargia et al., 2017).

In summary, it is the same epistemic and aleatory uncertainties that

prevent us from predicting earthquakes in a fully deterministic way, together with the limited record of seismicity (i.e. data sparsity and scarcity), that undermine the efforts for calculating the true seismic potential of faults. Clearly, reducing epistemic uncertainties is key to improving DSHA and PSHA.

## 1.4 Beyond consensus phenomenology: the case of waiting times

The widely accepted laws of seismology discussed in section 1.1, are empirical. The following analogy illustrates their usefulness and limitations: Most car drivers know by word of mouth that they should change the engine oil approximately every 5000 kilometers. While they may not know exactly how an internal combustion engine works and what is the exact role of oil in its operation, they do understand that oil lubricates the various moving parts of the engine. They also know, sometimes due to personal experience, that not changing the oil will result in engine problems in the long run. However, if drivers possessed the knowledge and the tools to monitor the status of the engine in detail, they would be able to anticipate situations where an early oil change is necessary, i.e. before the 5000 km mark, or when it is safe to extend the oil change to 6000 or 7000 kilometers. Similarly, the Gutenberg-Richter and the Omori-Utsu laws do reveal some information about the internal workings of the lithosphere, but not enough to allow accurate estimation of seismic hazard. For example, the observed frequency-magnitude distribution in a particular geographic region may suggest that there are two M 6 earthquakes per year *on average*. No information is given by this distribution on where and when these earthquakes could occur. In addition, there may be less or more than two M 6 earthquakes in that region in a particular year. Such problems maintain the drive to extract more information from earthquake catalogs.

As discussed in section 1.1, the rate of aftershocks typically follows the Omori-Utsu law, which is a power law. The situation regarding mainshocks is more complicated, as has been described in sections 1.1, 1.2, 1.3. An effort to create a unifying law for the waiting time  $\Delta t$  of earthquakes can be found in the work of Bak et al. (2002), who linked the waiting time and frequency-magnitude distributions as a function of the size of the geographic region under consideration. In the wake of that work, Corral (2004) showed that the probability density of waiting times,  $D(\Delta t)$  of worldwide seismicity, as well as several distinct geographic regions in different geotectonic environments (Japan, Iberian Peninsula, Southern California, British

Islands), can be described by:

$$D(\Delta t) = Rf(R\Delta t) \quad (1.7)$$

where  $R$  is the mean rate of occurrence in the region of interest.  $R$  is defined as the ratio of the number of events  $N$  divided by the total amount of time between event 1 and event  $N$ .  $f(R\Delta t)$  is a scaling function that can be approximated by the gamma distribution:

$$f(\theta) = C\theta^{-(1-\gamma)}\exp\left(\frac{-\theta^\delta}{B}\right) \quad (1.8)$$

with  $\delta \approx 1$ ,  $\gamma \approx 0.67$ , and  $C \approx 0.5$ . Here  $\theta = R\Delta t$ . This result suggests the existence of correlations beyond the domain of aftershocks, in sharp contrast with the Poisson model, which predicts exponentially distributed probability densities and thus a lack of correlation between events. Instead, the gamma distribution suggests that some kind of correlation exists, apart from the aftershock regime. Unfortunately, by itself the distribution does not identify the physical mechanisms that cause the said correlation. Interestingly, equation 1.8 has been shown to apply to induced seismicity as well as rock fracture and uniaxial compression experiments (Davidsen et al., 2007; Davidsen and Kwiatek, 2013). This suggests that the underlying processes may be similar across scales. Corral (2005) showed that another consequence of the gamma distribution is the decrease in hazard, which is defined as the ratio of the probability density to the complementary distribution function, with increasing time since the last event. Using conditional probability distributions, Corral (2006) found that there is an inverse relationship between the magnitude of event  $X$  and the waiting time ( $t_{X+1} - t_X$ ) until the next, a positive relationship between  $\Delta t_n$  and  $\Delta t_{n+1}$ , and no correlation between the magnitudes of successive events. These findings appear to contradict the Characteristic Earthquake model which predicts that faults produce (quasi-) periodic events with approximately the same magnitude. Recall here that the CE model is often used in probabilistic seismic hazard analysis. Note however that the Corral distribution applies to regions rather than individual faults.

The use of Equation 1.8 is empirical, just like the Gutenberg-Richter and Omori-Utsu laws, therefore it does not fully reveal the underlying physical processes that generate the observed behavior. Hainzl et al. (2006) showed that waiting time distributions for earthquakes in California, similar to the one predicted by equation 1.8 can be obtained with the ETAS model, i.e. Poissonian mainshocks and Omori-Utsu type aftershocks. However, they suggested that the Corral distribution can be used to quantify the number of

mainshocks in a catalog, as opposed to using more classic approaches for declustering. The view that equation 1.8 arises simply as a combination of the Poisson model for mainshocks and the Omori-Utsu law for aftershocks has been supported theoretically by Molchan (2005) and Saichev and Sornette (2007). Thus, it is not broadly accepted that the Corral distribution is universal, nor that it reveals the operation of some previously unknown physical mechanisms.

An empirical, unified law for the recurrence of earthquakes has been proposed in the form of a gamma distribution for waiting times. Corral's findings challenge some aspects of the current understanding of seismicity, i.e. the randomness predicted by the Poisson model and the quasi-periodic behavior predicted by the Characteristic Earthquake model. Due to the lack of a physics-based theoretical underpinning, the significance of these findings in relation to seismicity is contested, as shown above. It is not known whether the gamma distribution reveals the operation of unknown physical mechanisms, or whether it arises as the result of some combination of known ones.

## 1.5 Modeling seismicity as a complex system

The complex system approach to seismicity is motivated by the phenomenology of earthquakes and by aspects of fault mechanics. As stated at the beginning of this introduction, complex systems involve constituent elements that interact deterministically but non-linearly with each other, yet the collective macroscopic behavior of the system is richer than expected. Some common examples of complex systems are the weather, traffic, the stock market, and modern western economies (Tranquillo, 2019). These systems are prone to instabilities due to random perturbations. The perceived unpredictability of complex systems stems from the fact that it is either infeasible or impractical to track the behavior of each individual constituent. This then justifies the use of statistical and probabilistic methods in the study of these systems, even though they are not truly random, as is the case with radioactive decay. In the lithosphere there is a finite but practically uncountable number of rock elements that interact by deforming brittlely or frictionally<sup>1</sup>, however the combined outcome is not one of random slips and shaking, but one that obeys the empirical laws described earlier. Complex systems often exhibit scale invariance, as suggested by the

---

<sup>1</sup>The Frivolous Theorem of Arithmetic (“most natural numbers are very, very, very large”, from [mathworld.wolfram.com/FrivolousTheoremofArithmetic.html](http://mathworld.wolfram.com/FrivolousTheoremofArithmetic.html)) indicates that the number of interactions is very, very, very large.



emergence of power laws (Shcherbakov et al., 2015); and chaotic behavior, i.e. high sensitivity to initial conditions (Lorenz, 1963). Below we will briefly describe some of the classic models that have been used to simulate seismicity. Detailed reviews of these and other models can be found elsewhere (Rundle et al., 2003; Scholz, 2002; Shcherbakov et al., 2015).

One of the early attempts to simulate seismicity with a simplified analog system was the Burridge-Knopoff (BK) spring-block model. A number of blocks of known mass lie on a frictional surface. The blocks are connected with each other and to a driving plate via Hookean springs. The driving plate is displaced at a constant rate, which causes the springs to store elastic energy that is occasionally released when one or more blocks slide. Depending on the type of friction law used, the BK model can produce power law slip or characteristic event statistics, or an intermediate regime where the system switches between power law and characteristic events (“mode-switching”).

Another popular class of models are of the cellular automata (CA) type. CA models consist of cells, or nodes, on a grid. Each cell has certain properties, for example a value of strength and a value of stress applied to the cell. The stress applied to the entire assembly of cells is increased iteratively. Whenever the amount of stress applied to a cell exceeds its strength, the cell fails, the stress drops to a residual value, and the excess stress is redistributed to the neighboring cells, which may also “fail” if their strength is overcome. The size of an event is proportional to the amount of cells that “failed”. Examples include the forest fire, the Rundle-Jackson-Brown (RJB), and the Olami-Feder-Christensen (OFC) models. Unlike the BK model that uses a friction law, the RJB and OFC models use stress thresholds. Both the RJB and OFC models can be used to investigate the effect of long range interactions (coupling) between cells or nodes, which can be modeled via additional springs. Spatially varying failure thresholds can be implemented in the OFC model to simulate asperities.

Granular aggregates, for example tapioca particles, plastic disks, and glass beads, exhibit sudden bursts of slip when sheared at a constant rate of displacement (Dalton and Corcoran, 2001; Jiang et al., 2017; Lherminier et al., 2019). This behavior is known as crackling noise (Sethna et al., 2001). Crackling noise and seismicity share some characteristics, such as similar exponents for the frequency-size or frequency-magnitude distributions and mode switching. For granular media, these results can be understood in the context of phase transitions. Loose particles behave collectively as a fluid, producing small size events, whereas well confined particles in a jammed state (Cates et al., 1998) behave as a solid, producing a mix of characteristic and power law distributed slip instabilities. These macroscopic

characteristics can be captured by a lattice model for sheared granular media (Dahmen et al., 1998, 2011; Fisher et al., 1997), which is based on mean-field theory and the cellular fault model by Ben-Zion and Rice (1993). The position of the system in the phase diagram is determined based on the packing fraction, the coupling between lattice points, and the frictional weakening that occurs during slip.

To conclude, a number of numerical and physical analogs have been used to explain the complex nature of seismicity. These analog systems are characterized by intermittency (crackling), quasi-periodic or power law frequency-size statistics, and long-range interactions between constituent elements. Laboratory-based studies on the rheology of granular media and the resulting stick-slip statistics, have focused on experiments either at low normal stress, typically less than 1 MPa (Denisov et al., 2016; Lherminier et al., 2019), or at relatively small shear strains (Anthony and Marone, 2005; Johnson et al., 2013; Mair et al., 2002; Scuderi et al., 2014, 2015). Therefore, extrapolation is necessary to infer the behavior of granular media at higher normal stresses and larger shear displacements. Data obtained at higher normal stresses and large shear displacements are necessary to test the wider applicability of theoretical models (Dahmen et al., 2011; Uhl et al., 2015).

## 1.6 This work

In this work, we study the statistics of crackling noise from sheared layers of glass beads at elevated normal stresses (2 to 8 MPa) and at large shear strains (over 40). We use the frequency-size and waiting time distributions of crackling events to infer the state of the load-bearing framework of the aggregates, under various combinations of applied normal stress, load point velocity, machine stiffness, and particle size distribution.

Chapter 2 describes the rotary shear apparatus used in this thesis. The high stresses that develop during our experiments require that the samples are confined in steel rings, that do not allow direct observation of particle interactions. Because of this we developed an acoustic emission (AE) monitoring system that we use to estimate where crackling noise is generated. We present the results of four experiments under the same conditions and discuss the reproducibility of stick-slip statistics. In Chapter 3 we investigate the effect of normal stress, rate of rotation, and machine stiffness on the waiting times between AE events. The results show that the waiting times can be described by a gamma distribution with power law exponents ranging from 0 to 0.2 (see parameter  $1 - \gamma$  in equation 1.8), depending on normal stress. The rate of rotation and machine stiffness do

not have a clear effect on the exponent. We propose that waiting times are sensitive to the rigidity of the load-bearing framework, which increases with increasing normal stress. The majority of the experiments presented in this work have been performed at ambient relative humidity conditions. One way to remove humidity as a variable is by saturating the pores of the aggregates with water. Incidentally, by pressurizing the water in the pores we can investigate phenomena related to the principle of effective normal stress (e.g. cyclic loading). In Chapter 4 we show that the soda lime glass beads that we use in our samples are sensitive to time-dependent subcritical cracking, which results in drastically different frictional behavior compared to the dry case. We suggest that for future experiments a pore fluid that is chemically inert with respect to soda lime glass (e.g. decane or silicone oil) should be used instead of water. In Chapter 5 we show that our laboratory system can generate characteristic or power law distributed slip events depending on sample properties and normal stress. The samples also exhibited brief periods of mode-switching. These results suggest that faults may be inherently capable of generating characteristic and Gutenberg-Richter earthquakes, which can complicate efforts to assess seismic hazard. Conclusions and suggestions for future work are discussed in Chapter 6.



## Chapter 2

# Stick-slip statistics from large displacement granular friction experiments

### 2.1 Abstract

Is it possible to infer the microstructural state of a granular aggregate undergoing shear, based on statistical descriptions of its macroscopic behavior? Here, we take a necessary first step toward answering this question by examining the reproducibility of the statistics of stress drop, acoustic emission amplitude and recurrence time. We report on the results of friction experiments on glass beads gouges, performed in a rotary shear configuration. Our system exhibits some remarkable similarities but also notable differences from natural seismicity. We find that stress drop and acoustic emission amplitude, an analog for earthquake magnitude, are proportional and that both follow power law distributions that are truncated at their higher end. Our data also show that slip instabilities are correlated in time, much like natural and induced seismicity, but their nucleation sites are uniformly distributed in space. We conclude that our experimental approach generates statistically reproducible results, and that therefore it can be used to further investigate the sensitivity of statistics to systematic variation of the loading parameters.

### 2.2 Introduction

The relationship, causal or not, between small and large magnitude frictional instabilities is of central interest in the study of earthquakes. In

many regions around the world, the lithosphere deforms episodically at a variety of spatial and temporal scales (Ben-Zion, 2008). Typically, small magnitude deformation occurs much more frequently than large magnitude deformation. These characteristics present us with two challenges when we try to project seismicity patterns into the future. First, if we want to describe seismicity statistically, the uncertainty of our estimation increases as a function of magnitude, due to the lack of data. Because our oldest instrumental records date back to about a century only, there has been an ongoing discussion about the statistical model of the observed magnitude distribution of earthquakes (Kagan et al., 2012; Parsons and Geist, 2009; Wesnousky, 1994). For example, the choice between a variant of the Gutenberg-Richter model and the Characteristic Earthquake model has implications about the maximum expected magnitude of an earthquake, which is important for hazard assessment and policy making (Field et al., 2017; Marzocchi and Zechar, 2011; Stein et al., 2012). Second, if we wish to understand how deformation mechanisms operating at the microscale relate to the macroscopic frictional behavior of seismogenic faults, we have to establish reliable descriptors at both scales. Furthermore, we have to determine whether certain phenomena at the microscale are reliable forerunners of large magnitude events at the macroscale.

Studies of exhumed faults and drilled fault cores have revealed the presence of a granular layer, known as gouge, that is the product of wear and tear due to fault motion. The importance of interfaces, also known as “third-bodies”, has long been acknowledged in the field of Tribology (Godet, 1990). Indeed, it has been shown that the frictional stability of the gouge layer dominates the sliding behavior of the interface that it resides on. Laboratory experiments (Daniels and Hayman, 2008; Liu et al., 1995; Mandl et al., 1977; Radjai et al., 1998; Howell et al., 1999; Majmudar and Behringer, 2005) and Discrete Element Method (DEM) simulations (Aharonov and Sparks, 2002, 2004) have revealed that inside a stressed granular medium, groups of particles, known as grain bridges or force chains, support most of the imposed forces. From a mechanical point of view, the stick-slip behavior that certain granular media exhibit when sheared, is attributed to the recurrent generation, buckling, and eventual failure of such force chains. Numerous studies have focused on the effect of parameters such as particle characteristics and size distribution, layer thickness, relative humidity and loading velocity on the characteristics of unstable, stick-slip behavior of sheared granular layers (Anthony and Marone, 2005; Dorostkar et al., 2017a; Ferdowsi et al., 2013; Losert et al., 2000; Mair et al., 2002; Mair and Abe, 2008; Mair and Hazzard, 2007; Morgan and Boettcher, 1999; Nasuno et al., 1997; Scuderi et al., 2014, 2015). Overall,

these studies have attempted to interpret the macroscopic frictional behavior in the context of particle-scale interactions and the sensitivity of the latter to the investigated parameters.

Another way to obtain information about the microstructure of a deforming material is via acoustic emission (AE) monitoring. A material under stress can generate AE signals when elastic energy is released due to changes in its microstructure. Three very attractive aspects of AE monitoring are that it is passive, unlike other ultrasound-based methods, non-invasive, and it can provide information in near real-time if required by the application. Therefore, it is the ideal tool in numerous settings, such as structural health monitoring of aircraft, ships, bridges and tunnels, but also in materials science research (Grosse and Ohtsu, 2008). Various AE methods have been employed in experimental rock deformation (Lei and Ma, 2014; Lockner, 1993).

AE monitoring has also been employed in the study of deforming granular media (Michlmayr et al., 2012). Mair et al. (2007) monitored the rate of AE generation while shearing mm-thick layers of F110 sand and glass beads, using a double direct shear apparatus. One of their major findings is that the mean number of AE events per second decreases substantially within the initial 9 mm of displacement and remains stable thereafter. They attributed the initial elevated AE productivity to particle comminution and suggested that a steady-state rate is reached due to strain-localization within zones of reduced particle size. Using a similar approach, Johnson et al. (2013) showed that in the regime of regular stick-slip, micro-slip and AE activity increase log-linearly with time, prior to each main stress drop. Johnson and coworkers did not observe any evidence of slip events being triggered by AEs. Jiang et al. (2017) monitored AE rates and amplitudes while shearing cm-thick layers of glass beads at conditions relevant for landslide initiation, using a rotary shear apparatus. Their experiments show that stress drops and AE amplitudes scale linearly in log-log space. Another important finding was that the onset of AE events preceded the onset of the associated stress drop, which they interpreted as the result of local slip events leading to a larger sample-wide failure.

The studies mentioned in the previous paragraph have established temporal correlations between deformation and AE events. Drawing from their conclusions, the question is whether spatial patterns exist in the distribution of AE source locations. The existence or lack of such patterns will provide insight on whether different size AEs and stress drops can be causally linked, over what distance, and what time window. Such correlations could be the key to understanding the physical mechanisms that cause stick-slip instabilities. To this end, we use a rotary shear apparatus to

investigate the effect of large displacement on the evolution of the mechanical and acoustic properties of glass bead layers. Large total displacement produces a large collection of AE events, which is important for statistical treatment. We have advanced the state of the art of AE monitoring in this type of friction experiments, by locating the origin of the detected AE events. Such data, together with post-experimental sample analyses provide us with new insights about particle scale phenomena and how they link to sample-scale behavior. The aim of this chapter is to demonstrate the reproducibility of certain statistical descriptors of frictional instabilities in sheared granular assemblages and make a preliminary attempt at linking these descriptors with the microstructural state (e.g. porosity and rigidity) of the samples.

## 2.3 Methods

In this section we discuss the sample material and the experimental apparatus we used, as well as the experimental protocols and analyses we performed to obtain our results.

### 2.3.1 Sample material

We performed rotary shear experiments (r086, r097, r101, and r103) on dry glass bead aggregates. We chose glass beads as the sample material because of their tendency to exhibit stick-slip behavior and produce AE while sheared at room temperature conditions and at load point velocities relevant for seismic nucleation ( $<100 \mu\text{m/s}$ ). Furthermore, it is a well-studied material that has previously been used in numerous laboratory studies before (Anthony and Marone, 2005; Mair et al., 2002; Scuderi et al., 2014, 2015; Nasuno et al., 1997). In addition, the spherical shape of the beads is a close physical analog to the disk-shaped and spherical particles commonly used in DEM studies of sheared granular aggregates (Mair and Hazzard, 2007; Morgan and Boettcher, 1999; Morgan, 1999, 2004; Guo and Morgan, 2007). The initial particle size of the sample material was in the range of  $200 \mu\text{m}$  to  $900 \mu\text{m}$  with a dominant size of  $477 \mu\text{m}$ . The starting layer thickness was about 4.5 mm.

### 2.3.2 Rotary Apparatus (RAP)

For this study, we used a newly developed rotary shear apparatus (Figure 2.1). The rotary shear configuration allows us to investigate the evolution of AE characteristics over large shear displacements, unlike other common experimental designs (e.g. direct-shear, triaxial compression). The apparatus



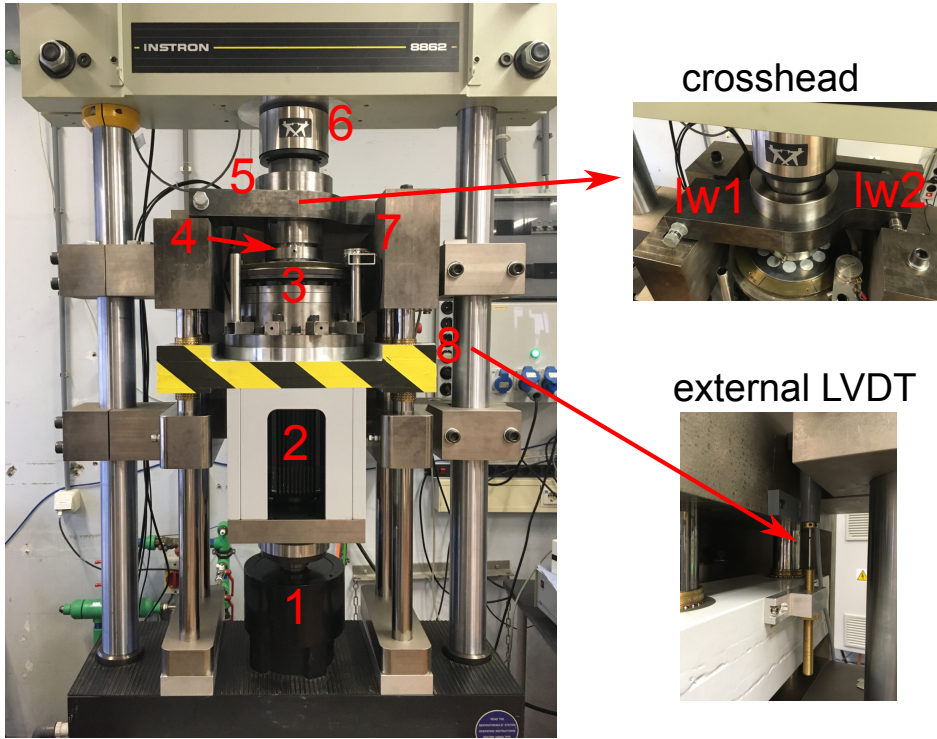
consists of a torque reaction frame that is housed inside an Instron 8862 testing machine equipped with a servo-controlled electromechanical actuator that may be operated either in position control ( $\pm 50$  mm range,  $5 \mu\text{m}$  resolution) or in load control mode ( $\pm 100$  kN range,  $0.008$  kN resolution). The torque reaction frame was manufactured by Tevel Techniek bv. A Parker MH205 motor provides rotary motion to the driving plate via a 1:160 harmonic drive gearbox. The motor and gearbox system was assembled by VarioDrive. Using the motor's onboard servo-controller, it is possible to control either the rotation rate (and thus shear displacement) or the torque (and thus the shear stress) imposed by the driving platter. In this study, we apply a constant rate of rotation. A pair of load cells ( $20$  kN range,  $0.008$  kN resolution), mounted on opposite sides of a horizontal steel block ("crosshead"), measure the reaction force of the frame due to the rotation imposed by the motor. The reaction force is converted to reaction torque and subsequently to shear stress on the sample. Axial displacement is also measured by an external linear variable differential transducer (LVDT;  $\pm 0.5$  mm range,  $0.1 \mu\text{m}$  resolution), installed at the side of the frame, at the height of the sample chamber. The driving platter is equipped with two angular potentiometers ( $0.001$  degrees, or about  $0.74 \mu\text{m}$  resolution) that measure its rotation. The resolution values reported here have been calculated with the respective transducer(s) at constant load or constant position, at steady state conditions, and reported as six standard deviations. A PT100 element is used to monitor the ambient temperature. A wall-mounted Fischer thermometer-hygrometer is used to measure the ambient relative humidity.

### 2.3.3 Experimental procedure

We conducted four, nominally identical experiments at  $8$  MPa effective normal stress and a rotational rate of  $0.02$  degrees/s, which corresponds to  $15 \mu\text{m/s}$  at the mean radius of the sample ( $42.5$  mm). The duration of the pre-compaction period, maximum displacement, total number of AE triggers, ambient temperature, and relative humidity are listed in Table 2.1.

Prior to each experiment, a known mass of the sample material, approximately  $30.20$  g, was funneled into the annular cavity formed by the bottom piston ring with the inner and outer confining rings. The amount of sample used was chosen such that the initial thickness of the resulting layer would be between  $4.5$  mm and  $5$  mm, at  $40\%$  initial porosity. The layer was flattened using a ring-shaped aluminum block and a bull's eye level was used to verify the result. The top piston ring was then installed, closing the annular cavity. The height of the sample assembly was measured ( $\pm 0.05$  mm) in four locations at  $90$ -degree intervals and the relative offset of two

a. Rotary Shear Apparatus



b. Sample chamber & piezoelectric transducers

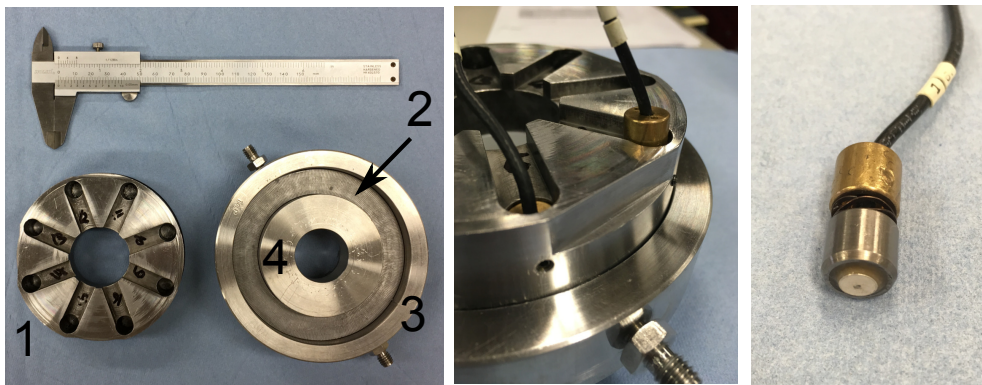


Figure 2.1

**Figure 2.1:** (a) View of the Rotary Shear Apparatus (RAP). 1: Instron actuator. 2: MH205 motor. 3: Harmonic drive and rotating platter. 4: Sample chamber. 5: Crosshead, equipped with two load cells (*lw1*, *lw2*) for measuring traction. 6: Instron load cell. 7: Angular potentiometer (1 of 2). 8: external LVDT. (b) Sample chamber and piezoelectric transducers. (b, left) 1: Top piston. 2: Bottom piston. 3: Outer ring with two fluid ports. 4: Inner ring. The outer diameter of the sample cavity is 10 cm and the inner diameter 7 cm. 150 mm caliper for scale. (b, middle) close-up view of the assembled sample chamber. One piezoelectric transducer has been properly installed (left), whereas a second one has been partially inserted into its slot. A small screw is used to fix the brass cap against the steel piston. (b, right) A piezoelectric transducer. The piezoelectric element (white disk) is 5 mm in diameter. The casing has an outer diameter of 10 mm. When installed, the piezoelectric elements lie approximately 5 mm away from the sample.

reference points, one on the top piston and one on the bottom piston, was calculated by measuring their respective azimuths using a repurposed microscope stage ( $\pm 0.5^\circ$  resolution). Subsequently, all 16 AE transducers were installed, and the sample assembly was placed into the apparatus, with the bottom piston interlocking with the driving platter. The actuator was then moved upwards, lifting the driving platter and the sample assembly up and interlocking the top piston with the crosshead. After establishing axial touch, the actuator was switched to load control mode and the target total normal load was applied gradually over a period of 60 s. To shear the sample at a constant rate, clockwise rotation was applied by the Parker motor for about 3 hours. At that point, a brief counter-clockwise rotation ( $2^0$ - $3^0$ ) was performed to remove the shear load. Subsequently, normal stress was reduced gradually, over a period of 60 s. After the experiment, the height of the sample assembly and the relative angular offset between the two pistons were measured again. Finally, the sample was retrieved and prepared for particle size analysis and observation with a tabletop scanning electron microscope (SEM).

### 2.3.4 Data processing

#### Mechanical data

We calculated the apparent coefficient of friction as the ratio of shear stress to normal stress. Shear stress was calculated by converting the time series of the load, recorded by the two load cells installed in the crosshead, to torque on

**Table 2.1:** *Table of experiments.*

Exp. ID	$t_{pc}$ (s)	Max. LPD ( $^{\circ}$ ; mm)	N	% N successfully located	T ( $^{\circ}$ C)	RH (%)
r086	694	195;145	41918	89	23	62
r097	484	222; 165	52765	88	23	50
r101	1240	233; 173	49045	87	20	50
r103	1888	223; 165	33567	90	20	50

the sample and dividing by the surface area of the piston ring. As the normal stress was servo controlled, variations in friction largely reflect variations in shear stress. The thickness of the sample at any point during the experiment was obtained using the time series of the two LVDTs and the measurement of the sample chamber’s thickness after the experiment. To account for the distortion of the apparatus, we subtracted from the axial position record the product of the machine’s axial compliance and the change in normal stress at every time step. The incremental relative angular displacement of the two piston rings was calculated using the time series of the angular potentiometers and the measurement of the final angular offset. Load point displacement is expressed either in degrees or in millimeters referenced to the mean radius of the sample.

Visual comparison of the mechanical and AE data revealed that the AE system is more sensitive to small size events. Thus, the time series of AE triggers was used as a reference to find stress drops in the shear stress data. Note that this is the opposite approach from e.g. Goebel et al. (2012). The following automated procedure was used to measure the stress drop associated with each AE trigger event. First, the timestamp of the trigger block was used to determine the equivalent time window (6 ms-long, corresponding to the length of each AE record) of mechanical data. Second, a moving average filter (10 samples-long window) was applied to the time series of the shear stress. Next, the minimum shear stress in the window was found. Finally, the maximum shear stress value between the start of the window and the time corresponding to the minimum shear stress was picked.

### Locating the source of acoustic emission events

We estimated 1D source locations of acoustic emission events by automatically picking first arrival times of the fast, longitudinal waves and inverting them for minimum time-of-flight ( $t_0$ ), source location azimuth ( $\theta_0$ ), and apparent wave propagation velocity ( $v_0$ ). A single velocity model was assumed, based on the fact that the dominant wavelength of the AE

waveforms is larger or at least comparable to the distance between the sample and the nearest AE transducers. We define the minimum time-of-flight  $t_0$  as the time-of-flight from the source to the receiver that records the earliest arrival. The source location ( $\theta_0$ ) is expressed as the azimuth along the mean circumference of the sample ( $r_{\text{mean}} = 42.5$  mm), referenced to the top, stationary piston. We chose to solve for one spatial dimension instead of three ( $r_0, \theta_0, z_0$ ) because the estimated errors in the radial and vertical dimensions ( $r_0$  and  $z_0$  respectively) are comparable to the sample size in those dimensions (radial size of the sample: 15 mm; sample height: between 5 mm and 2 mm, depending on the initial height and the amount of compaction during the experiment). Therefore, we fixed  $r_0 = 42.5$  mm and  $z_0 = 0$  mm, with zero height referring to the middle of the sample. Tests using calcite powder, a material that exhibits stable sliding and does not produce AE under the same experimental conditions, revealed that the apparatus does not produce detectable signals. Thus, all of the AE events recorded during the experiments discussed here must have originated from within the aggregates. A reliable method for automatic first arrival picking of earthquake signals and acoustic emissions is based on the Akaike Information Criterion (Akaike, 1971). An AIC-based characteristic function can be evaluated by applying equation 2 from Zhang et al. (2003) on a seismogram:

$$AIC(x) = x \log(\text{var}(s[1, x])) + (N - x - 1) \log(\text{var}(s[x + 1, N])) \quad (2.1)$$

where  $s$  is a seismogram of length  $N$ , and  $x$  is a variable that takes any value in the window  $[1, N]$ . The signal onset should coincide with the global minimum of the AIC function (Figure 2.2a, bottom panel). However, depending on the type of signal onset and the signal to noise ratio of the waveform, the global minimum of the AIC function may be shifted in time. To overcome this problem, the AIC formula should be computed only for the part of the seismogram that includes the signal's onset, instead of the entire seismogram. Perhaps the most commonly used method for seismic and acoustic event detection is some variation of the short-term/long-term average (STA/LTA) method Allen (1978). The downside of this method is that the analyst must choose the optimum lengths of the short- and long-term average windows and select a threshold value for automatic picking. Because the waveforms we recorded for each event differ in phase and amplitude depending on the distance of each receiver from the source, we opted for a more hands-off approach: higher order statistics have previously been used as a method for detecting the signal onset Küperkoch et al. (2010). The expanding kurtosis of an AE waveform reaches its maximum shortly after the transition from noise to an AE signal. For each individual waveform, we calculated an expanding kurtosis function in order to estimate the approximate onset of the AE signal

(Figure 2.2a, middle panel). Subsequently, we selected a 200  $\mu s$  long window of the waveform, such that the window terminated at the onset time estimated by the peak of the expanding kurtosis function. The length of that window was preselected based on the dimensions of the sample and the expected maximum travel time between the source and the farthest receiver. We then applied the AIC formula to that subset of the waveform to obtain a more accurate onset time (Figure 2.2a, bottom panel). The accuracy of the picked onsets was improved by applying a low-pass filter (600 kHz cutoff frequency) to the waveforms before submitting them to the procedure described above.

The next step in locating the azimuth of the AE sources was the inversion of the observed arrival times. Because the sample chamber is ring shaped, for each event we used picks from AE receivers located within line-of-sight of the approximate source location. This choice has two advantages: first, we do not have to search for complicated wave paths to account for the time delays observed in the onsets of the signals recorded at receivers located farther than about  $70^\circ$  from the presumed source location; and, second, the receivers in the proximity of each AE event typically show high signal-to-noise ratio (SNR) and impulsive onsets compared to low SNR and emergent onsets at receivers farther away or on the far side of the piston rings (Figure 2.2b). High SNR and impulsive onsets present a more favorable scenario to both manual and automatic picking, resulting in more reliable picks. Due to the spacing of the AE receivers and depending on the relative offset of the top and bottom piston arrays at the time of the event, between 5 and 7 receivers receive a direct first wave from the source. For each event, we ran an iterative scheme that minimized the sum of the squared differences between observed and predicted onset times,

$$m_{(t,\theta,v)} = \sum_{i=1}^n (t_i^0 - t_i^p)^2 \quad (2.2)$$

where  $m_{(t,\theta,v)}$  is the misfit at  $(t, \theta, v)$ ,  $n$  is the total number of receivers used in the calculation,  $t_i^0$  is the observed arrival time at receiver  $i$ , and  $t_i^p$  is the predicted arrival time for receiver  $i$ . The scheme uses the BFGS method developed by Broyden, Fletcher, Goldfarb and Shanno Nocedal et al. (2006). The predicted onset times correspond to direct waves in a single velocity mode since the dominant wavelength of the AE signals is comparable to the dimensions of the structure in which the signals propagate. We obtained a measure of the uncertainty in each solution by estimating the standard errors of the parameters we inverted for ( $t_0$ ,  $\theta_0$ , and  $v_0$ ) from the Hessian matrix supplied by the BFGS minimizer. We report uncertainties as two standard deviations, i.e. twice the standard error of each parameter. Our criteria for

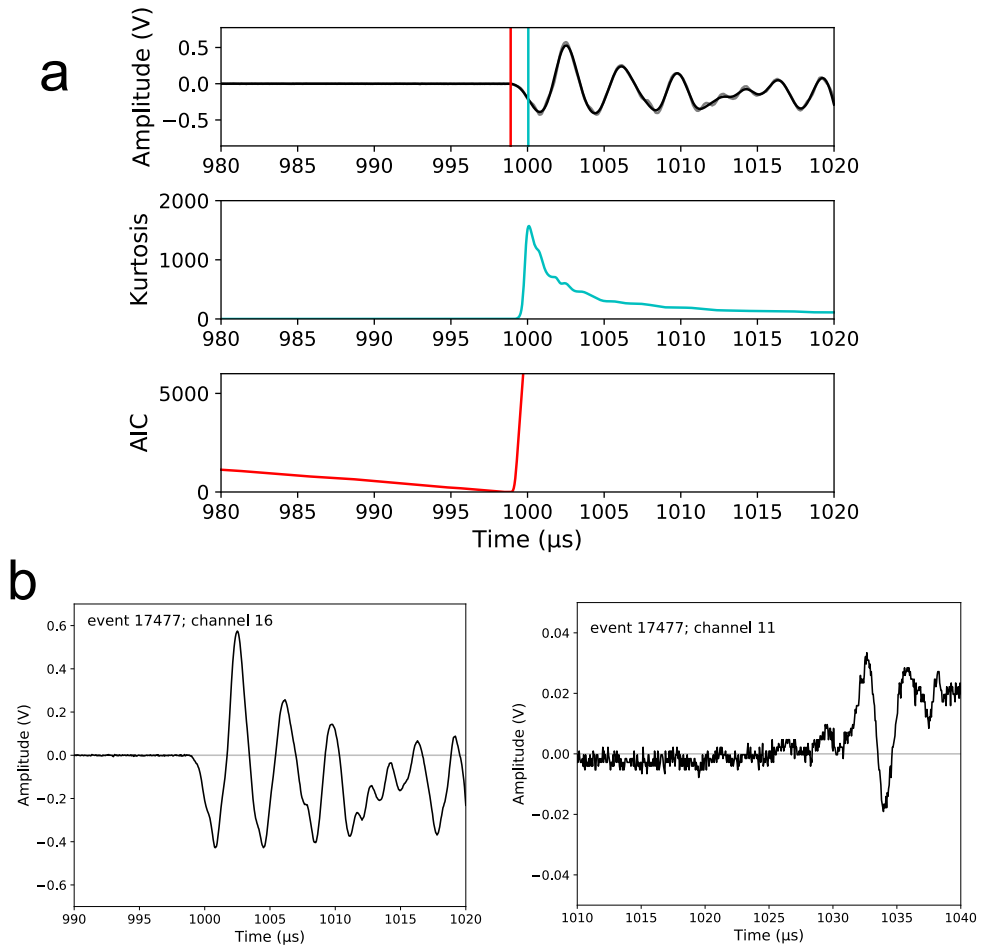


**Figure 2.2:** (a) Example of the automatic picking procedure. Data from experiment r086, event 17477, transducer 16 (top, stationary piston). (Top panel) Filtered signal (black), with kurtosis (cyan) and AIC (red) picks. A low pass Butterworth filter with 600 kHz corner frequency has been applied to the raw signal (grey) prior to the automatic picking procedure. (Middle panel) The expanding kurtosis characteristic function. (Bottom panel) The AIC characteristic function calculated for a portion of the signal. The first arrival corresponds to the global minimum of the AIC CF. (b) Comparison of signal onsets at two different transducers inside the top, stationary piston for event 17477. (Left) Impulsive onset recorded by the nearest transducer. (Right) Noisy signal and emergent onset (from about 1020  $\mu\text{s}$  onward), recorded by the transducer that was positioned 135 degrees away from the one in the left panel.

accepting a solution are as follows: 1) the minimization must have terminated successfully, 2) the estimated  $t_0$  must be reasonable based on the dimensions of the sample and the maximum possible travel distance between the source and the nearest receiver ( $7 \mu\text{s}$  for about 10.6 mm at 1500 m/s), and 3) the estimated velocity must be positive and not exceed the longitudinal wave velocity in steel (about 5800 m/s). Typically, more than 80% of the total number of trigger events per experiment are successfully processed (Table 2.1).

We validated this method experimentally by performing glass capillary fracture tests between the steel piston rings. The fracture of a glass capillary produces a sharp force pulse that sends elastic waves through the steel pistons. The AE receivers record the signals and the resulting waveforms can be used to estimate the location of the fractured tube. By performing multiple tests at different locations along the piston rings and for various relative offsets between the top and bottom receiver arrays, we determined that the mean uncertainty in the source azimuth, given as 2 standard deviations, is about  $\pm 3.5$  degrees ( $\pm 2.6$  mm).

### Measuring the size of AE events

For every event, we measured the maximum amplitude recorded by each of the 16 receivers and defined the characteristic amplitude for that event as the median of those 16 maximum values. The squared median can be used as a proxy for signal energy. We use the median value as a representative amplitude in order to suppress the effects of receiver-to-piston coupling and wave interference. We should emphasize that whereas the AE source locations are based on first arrival times, the maximum amplitudes were measured on the complete, 6 ms long waveforms.

### Post-mortem sample analysis

Particle size analysis was performed using a Mastersizer S device. We present the results of the particle size analyses as percent volume of each fraction versus the logarithm of particle size in micrometers. Scanning electron photomicrographs of particles from r086 were obtained using a JEOL JCM-6000 tabletop SEM.

## 2.4 Results

### 2.4.1 Mechanical behavior

The mechanical data from all four experiments indicate irregular stick-slip behavior (Figure 2.3). Apparent friction remained within a constant



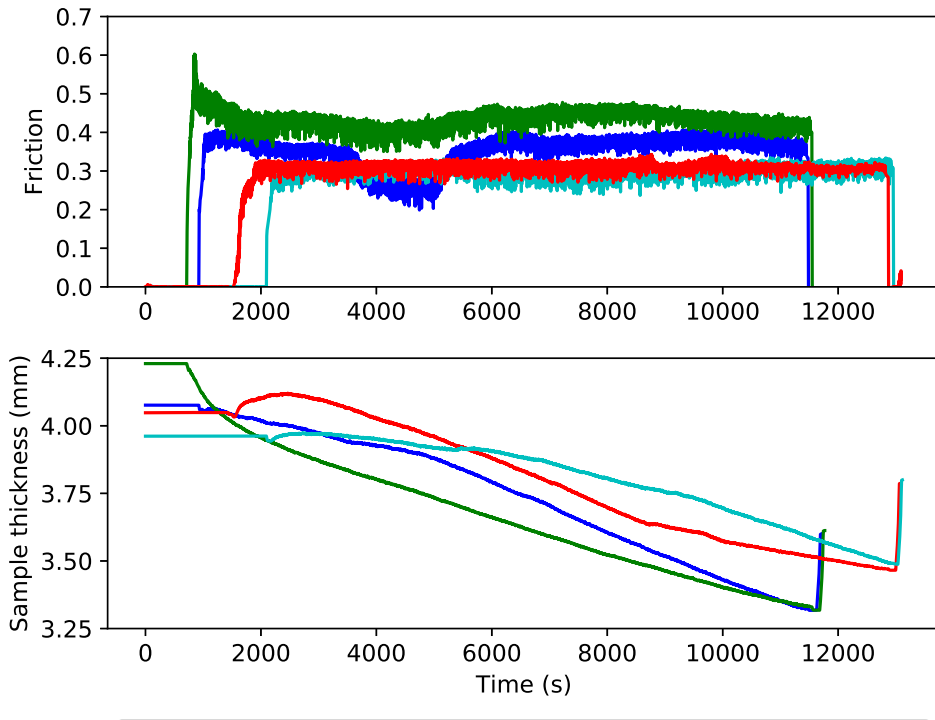


**Figure 2.3:** Friction and sample thickness time series. The coloring scheme is the same in both panels. The apparent friction shown here is the ratio of shear to normal stress. The thickness data shown in this figure have been obtained via the external LVDT. Note that episodes of strain hardening and weakening are more prominent in r086 and r097 than in r101 and r103. The peak strength of about 0.6 observed in r097 (green) is due to a temporary re-adjustment of the load cells inside the crosshead.

frictional envelope between 0.2 and 0.6, with the largest stress drops reducing the measured shear stress by about 1 MPa. Experiments r086 and r097 experienced some long-term strain hardening and weakening. The peak in strength, approximately 0.6, seen shortly after the initiation of shearing during experiment r097, was due to manual re-adjustment of the load cells in the crosshead. All of the recorded stress drops were partial, meaning that none of the samples experienced measurable zero apparent friction at any time during shearing. In one of the experiments (r101) the frictional envelope became narrower toward the end of the experiment.

LVDT records as well as benchtop measurements showed that by the end of each experiment, the samples had experienced net compaction (Figure 2.3,

lower panel; Figure 2.4, top panel). The compaction rate varied within the same experiment but also between experiments, and in two cases (r101 and r103) there was a period of apparent net dilation that commenced shortly after the start of shearing. Individual slip events exhibited inconsistent volumetric behavior, with some events dominated by net compaction whereas other by net dilation (Figure 2.6). Overall, our results show a more complicated volumetric response compared to previous work (Anthony and Marone, 2005; Jiang et al., 2017).

## 2.4.2 Distribution of AE sources

Figure 2.5 shows the spatial distribution of AE sources, indicated by the black circles, versus time, for experiment r103. In all of the experiments, the spatial distribution of AE sources during pre-compaction and the first 1000 s of shearing ( $20^\circ$ , or 15 mm of displacement) is different than in the rest of each experiment. To investigate the sensitivity of the distribution of AE events early in an experiment to variations in the thickness of the sample along the ring, we quantified the AE productivity, defined as the number of AE events per mm of displacement, per quadrant. Figure 2.4 (bottom panel) shows that the AE productivity during pre-compaction and the first  $20^\circ$  of displacement was larger at the initially thickest part of each sample. Interestingly, in r086 and r097 there were about 10 to 20 times more AE events generated per mm of displacement at the thickest part of the sample, compared to the thinnest one. In r101, the ratio was reduced to about 4:1, whereas in r103 the ratio was about 2:1. Experiment r103 had the smallest variability in initial sample thickness (Figure 2.4, top panel). In fact, the initial sample thickness measured at the two thickest positions was the same and equal to 4.45 mm, which provides an explanation for the difference in behavior compared to the other three experiments plotted in Figure 2.4 (bottom panel).

## 2.4.3 Juxtaposing mechanical and AE data

In order to better understand the relationship between the mechanical behavior of our samples and the sources of elastic waves inside them, it is instructive to look at small time windows (order of 10 s). Figure 2.6 shows friction, sample thickness, and load point displacement data from a 9 s long part of experiment r103. Also shown are the calculated AE source locations, indicated by the black circles. The size of the circles scales with the characteristic amplitude of the respective AE event. The selected time window contains data that are representative of other parts of r103, but also of the other three experiments. The excerpt contains three AE events of

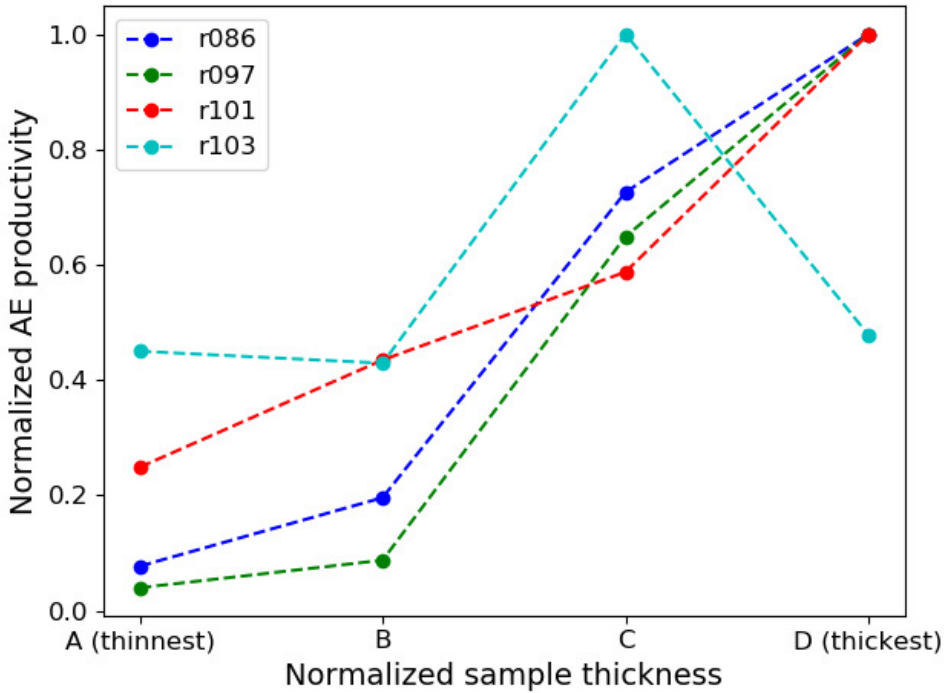
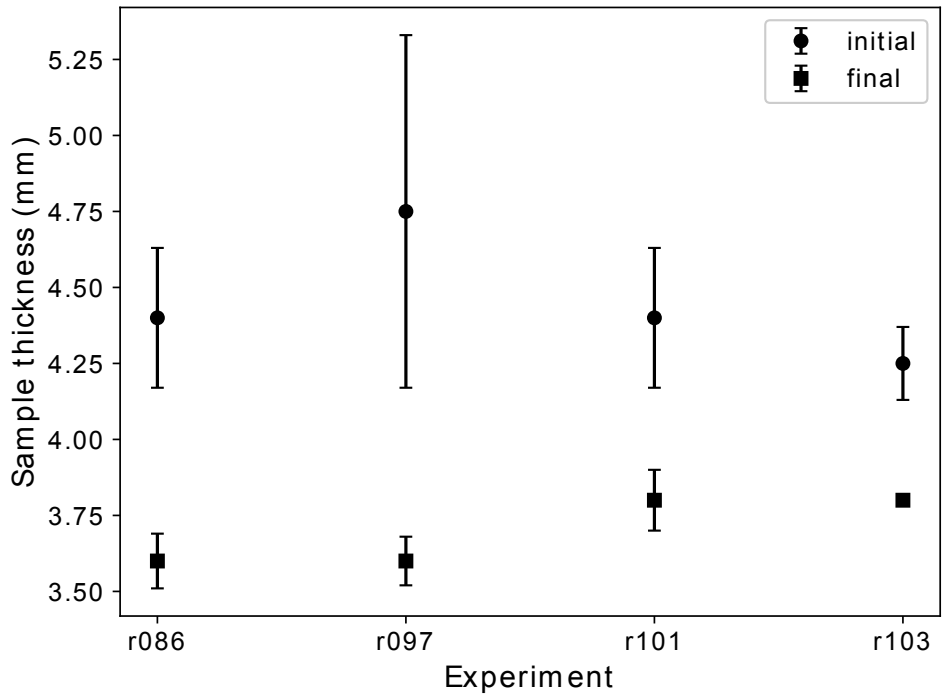
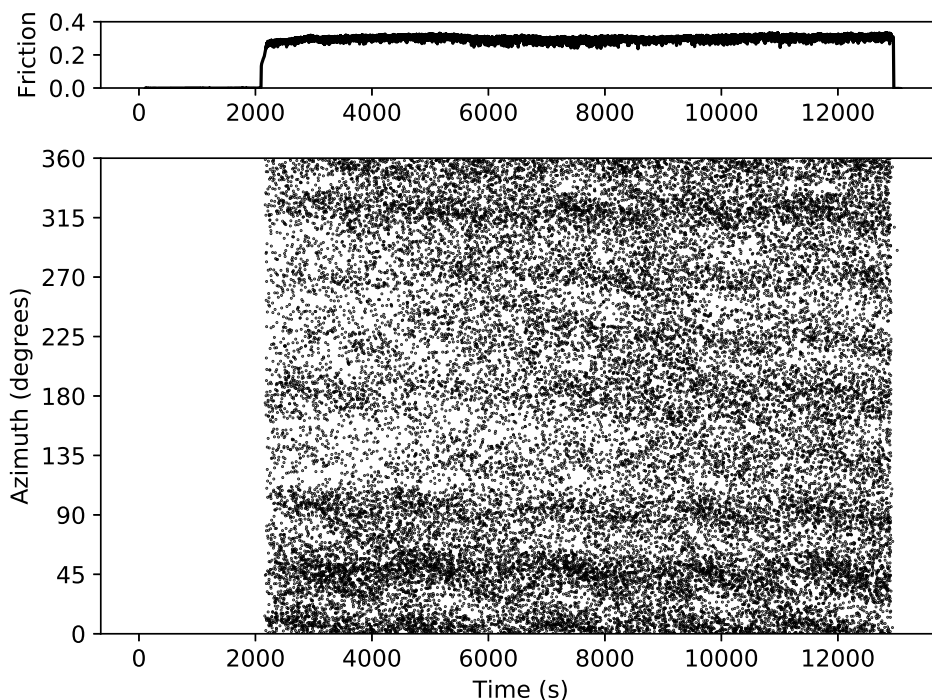


Figure 2.4

**Figure 2.4:** (top panel) Data from benchtop (i.e. no normal stress) measurements of sample thickness, before and after every experiment. The measurements were performed using a caliper with  $\pm 0.05$  mm resolution. The circles and squares represent the mean of four measurements at four locations. The bars represent one standard deviation. (bottom panel) Normalized AE productivity versus normalized initial sample thickness, for the pre-compaction period plus the first 1000s of shearing. Starting thickness measurements were performed in 4 locations along the piston rings (A, B, C, D) prior to each experiment. AE productivity was higher at the thickest part of the sample in all experiments. Note that in experiment r103, the initial sample thickness in positions “C” and “D” was the same and equal to 4.45 mm.



**Figure 2.5:** Friction and AE source locations versus time. Data from experiment r103. A detail of this plot can be seen in Figure 2.6.

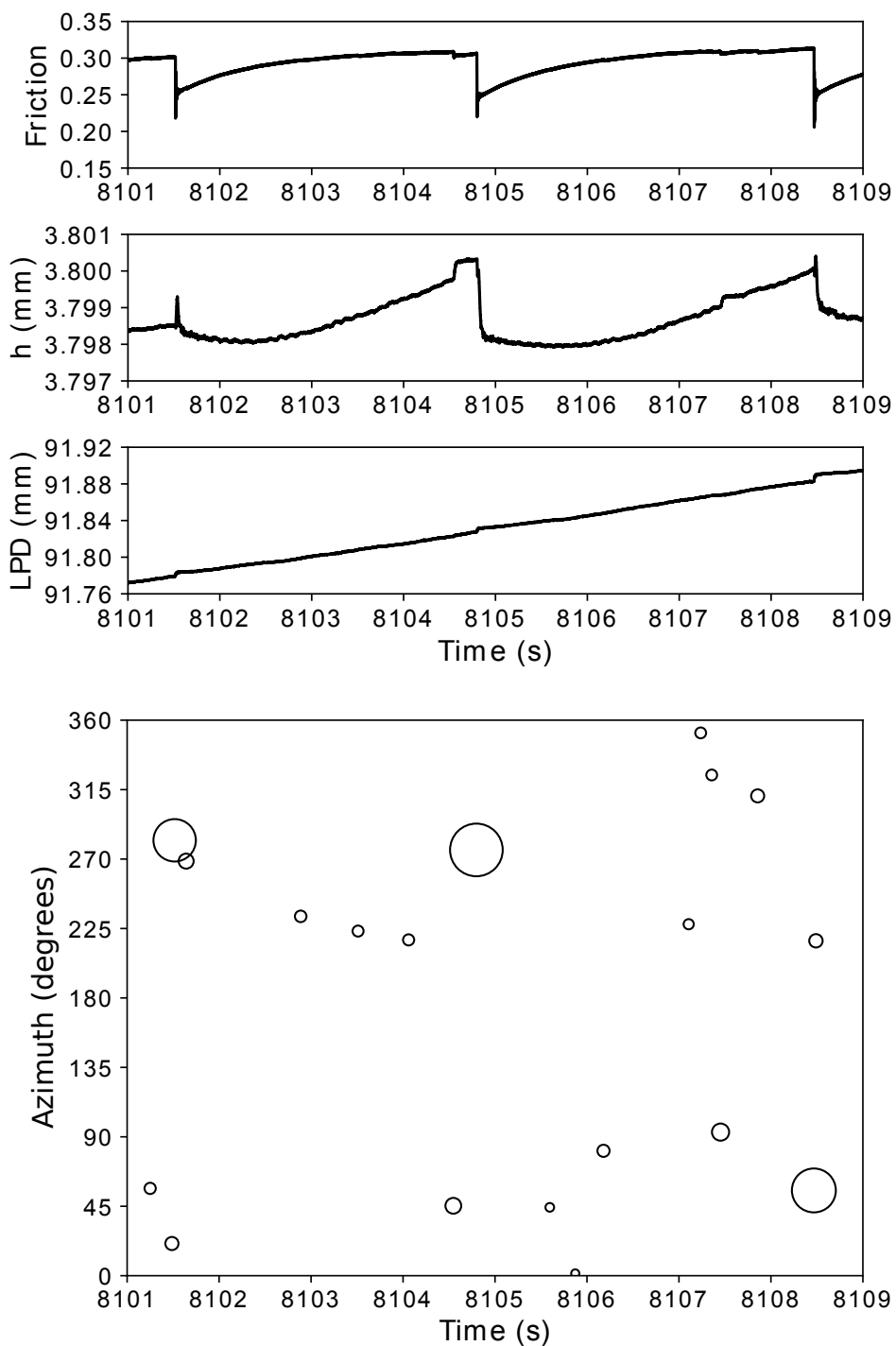
large amplitude, that were also associated with stress drops of about 0.8 MPa, rapid volumetric change and slip. Several smaller, in terms of characteristic amplitude, AE events occurred between the three major events, but their signature in the mechanical data is more difficult to discern. The figure suggests that perhaps there is a relationship between the magnitude of stress drop and the characteristic amplitude of the associated acoustic emission. It further suggests that macroscopic changes in stress, volume and displacement are only visible for events with a characteristic amplitude larger than a certain threshold.

In general, stress drop values and squared characteristic amplitudes are proportional in log-log space (Figure 2.7). The scatter is larger for characteristic amplitudes smaller than 0.05 V than for larger amplitudes. Nevertheless, the data from all four experiments share similar characteristics. Note that the maximum stress drop values and characteristic amplitudes are similar among the experiments.

#### 2.4.4 Distributions of AE properties and stress drops

We examine the complementary (survivor) cumulative distributions (CCDs) of characteristic amplitudes, stress drops, recurrence times, and source locations to determine whether they show any scaling properties. All of the distributions represent data that span the duration of shearing, excluding the first 1000 s of it. This means we have excluded events that occurred during axial loading, pre-compaction, the initial 1000 s of shearing, and shear and axial unloading. Instead, we are focusing on the “steady state” shearing, including the long-term periods of strain weakening and hardening seen in r086 and r101.

The characteristic amplitudes and stress drop distributions (Figure 2.8) show similar scaling behavior. This is expected, based on the approximately proportional scaling between the two quantities (Figure 2.7). The characteristic amplitude distributions (bin size = 0.05 V) show three distinctive segments: a relatively flat part up to 50 mV, followed by a linear part with a slope  $b \sim 1$ , that transitions into a steeply dipping ( $b \sim 10$ ) third segment beyond 600 mV. The transition from the first to the second segment indicates the lowest characteristic amplitude, in this case  $\sim 50$  mV, for which our AE catalogs can be considered complete. Similarly, for the stress drop distributions (bin size = 0.005 MPa), the catalog appears complete down to at least 0.005 MPa and it features a sharp drop-off beyond 0.3 MPa. In general, the range of linear behavior is rather narrow (1 to 2 decades), as is often the case for experimental studies of this type (Dalton and Corcoran, 2002; Daniels and Hayman, 2008; Denisov et al., 2016).

*Figure 2.6*

**Figure 2.6:** Representative mechanical and AE data, from experiment r103. From top to bottom, friction, sample thickness  $h$  ( "down" is compaction, "up" is dilation), load point displacement (LPD), and AE locations (dots) versus time. Three large events and a number of smaller ones can be seen. Uncertainty in the source locations is typically  $\pm 3.5$  degrees. The data shown here are representative of other parts of r103, but also of the other three experiments.

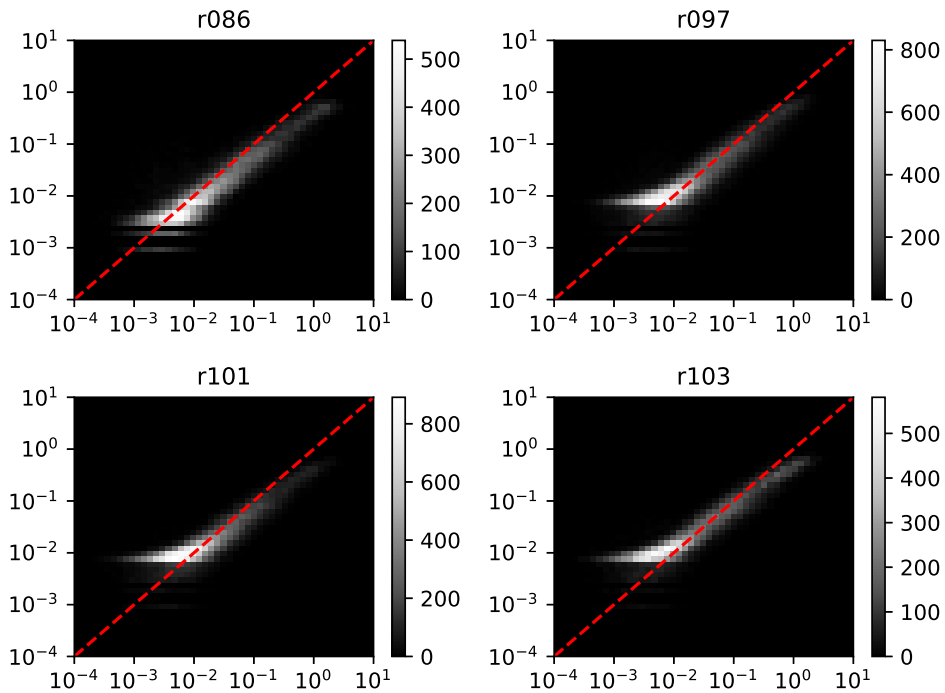


**Figure 2.7:** 2D histograms of stress drop (MPa) versus squared AE amplitude ( $V^2$ ), for all experiments. The slope of the red dashed lines is  $b = 1$ . The noise level for the AE amplitudes is less than 0.02 V on average and for the stress drops less than 0.02 MPa.

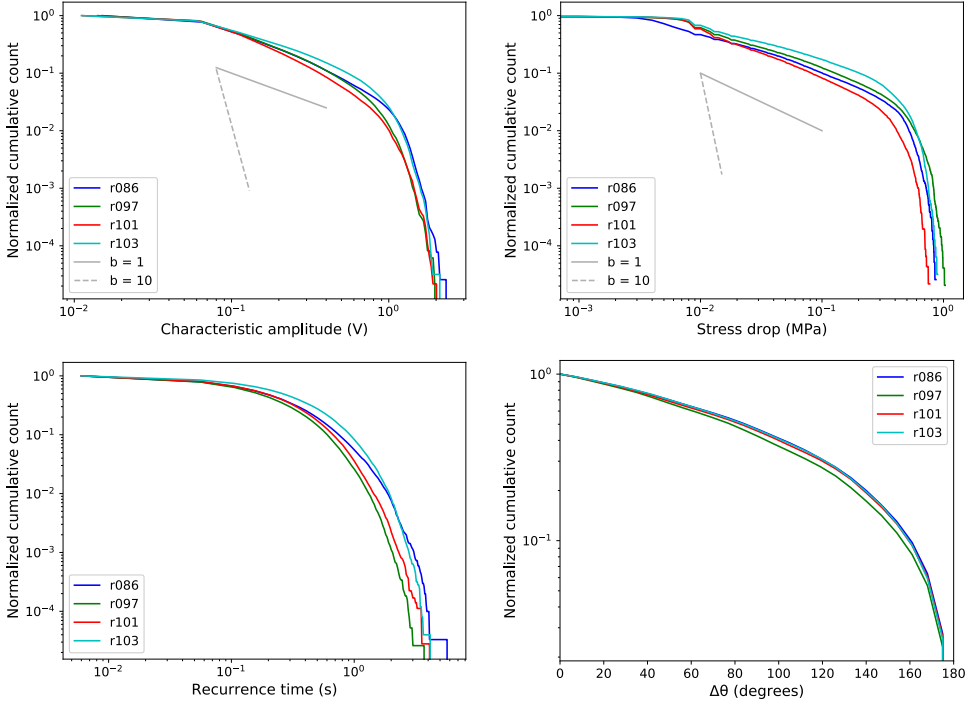


**Figure 2.8:** (top left) CCDs of characteristic amplitude. The amplitude of completeness is about 50 mV (for a noise level of less than 0.02 V), followed by a linear segment with  $b \sim 1$ , followed by a sharp drop-off beyond 0.6 V. The maximum characteristic amplitudes recorded in each of the four experiments are comparable (about 2 V). The truncation at large amplitudes is probably due to the size of the sample. (top right) CCDs of stress drops. The catalog appears to be complete down to 5 kPa, with a linear segment ( $b \sim 1$ ) that extends up to about 0.3 MPa, followed by a sharp drop-off. Note that the maximum stress drops recorded in each of the four experiments lie between 0.75 MPa and 1 MPa. The truncation at large stress drops is probably due to the size of the sample. (bottom left) CCDs of recurrence time. Note the similarly shaped distributions of all four experiments. (bottom right) CCDs of the distance  $\Delta\theta$  between consecutive events for each experiment. The bin size is  $7^\circ$ , based on the average  $\pm 3.5^\circ$  uncertainty of the AE source locations.



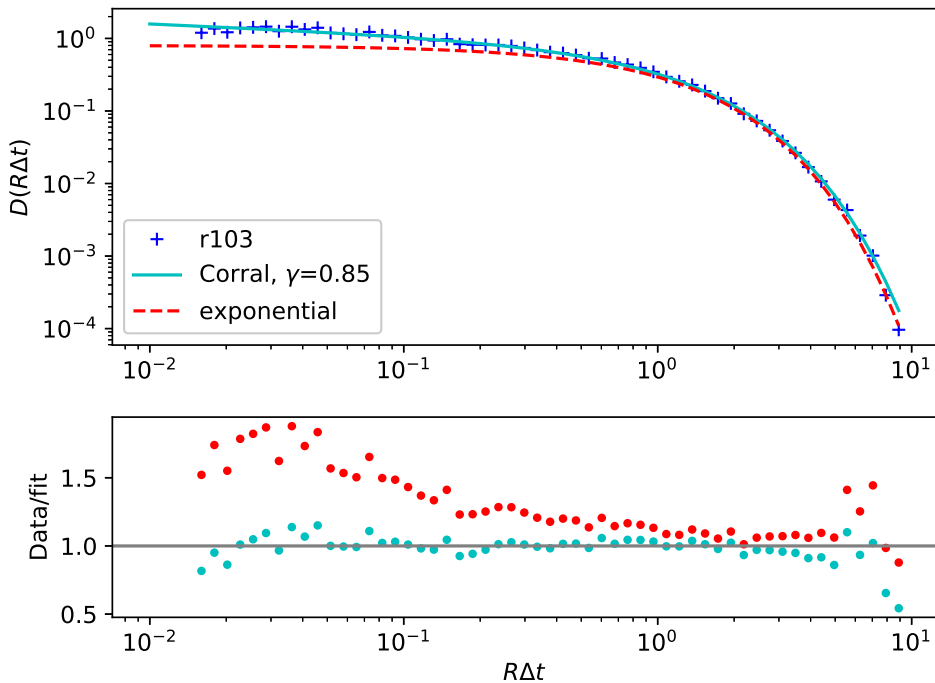


**Figure 2.9:** (top panel) RT distribution of r103 and comparison with the probability density of the Corral (gamma) and exponential distributions. (bottom panel) Ratio of the data to the Corral (cyan) and exponential (red) distributions. Note that the Corral distribution can describe the entire range of  $R\Delta t$  better than the exponential distribution.

The recurrence time (RT) CCDs (bin size = 0.05 s) of all four experiments are similarly shaped and terminate between 3s and 6s (Figure 2.8). For RTs longer than 0.8 s, data from r086 show a slight deviation from the trend of the other three experiments. Figure 2.9 shows that the discrete distributions of RTs from r103 (as a representative case for all of the experiments) can be described by a modified gamma distribution (Corral, 2004; Davidsen et al., 2007; Davidsen and Kwiatek, 2013):

$$f(\theta) = C\theta^{-(1-\gamma)}\exp\left(\frac{-\theta^\delta}{B}\right) \quad (2.3)$$

where  $\theta = \Delta t / \langle \Delta t \rangle$  are the recurrence times  $\Delta t$  normalized by the mean recurrence interval  $\langle \Delta t \rangle$ , and  $C$ ,  $\gamma$ ,  $B$  are constants.

Our ability to locate the source of the majority of AE triggers allows us

to investigate the distribution of spacing of consecutive events (Figure 2.8). All four experiments show very similar scaling (bin size =  $7^\circ$ ), with values for r097 lying slightly below those of the other experiments at distances beyond  $30^\circ$ . It is worth noting that the catalog of AEs used for investigating inter-event distances does not include those events that occurred during the first 1000 s of shearing, so as to minimize potential bias introduced by the initial homogeneity of the sample layers.

We note that further filtering of the data that is plotted in these distributions does not alter their shape significantly, with the exception of the RT distributions. For example, using only events associated with stress drops of 0.5 MPa and above will shift the RT plots to the right. Nevertheless, it is not the purpose of this chapter to investigate such effects.

Time-lapse plots of the characteristic amplitude distributions are able to capture the evolution in frictional behavior that we observe in r101. Figure 2.10 shows a side by side comparison of the characteristic amplitude and stress drop distributions from r101 and r103, for six consecutive 30-minute windows, the first one of which begins 1000 s after the start of shearing. In each case, the black curves show the distributions of all of the events included in the 6 windows. The plots for r103 show that the distributions of characteristic amplitudes and stress drops remain consistent throughout the experiment. This is also the case for r086 and r097 (not shown). However, the plots for r101 show that these distributions changed during the last hour of the experiment. More specifically, the number of small events increased in proportion to large events. Moreover, the upper end of the distributions moved to the left, indicating truncation at smaller values than earlier in the experiment. An additional observation is that in both experiments, the number of AE events per window, shown in parentheses in the legends, increased over time. This does not apply to the last one (6<sup>th</sup> window), which contains fewer events due to the cessation of shearing during that window. A similar increase in the AE rate as a function of displacement was observed in r086 and r097 as well.

### 2.4.5 Post-mortem observations

Post-experiment visual examination of the samples showed evidence of particle size reduction, in the form of very fine powder. The concentration of powdered material was consistently higher along the boundary between the sample and the rotating piston, forming a cohesive layer. In experiment r097 a small patch of cohesive, comminuted material was also found on the stationary piston. Particle size analysis on randomly selected portions of the salvaged samples showed that, indeed, finer material was generated during each experiment (Figure 2.11, colored curves). A significant amount of the

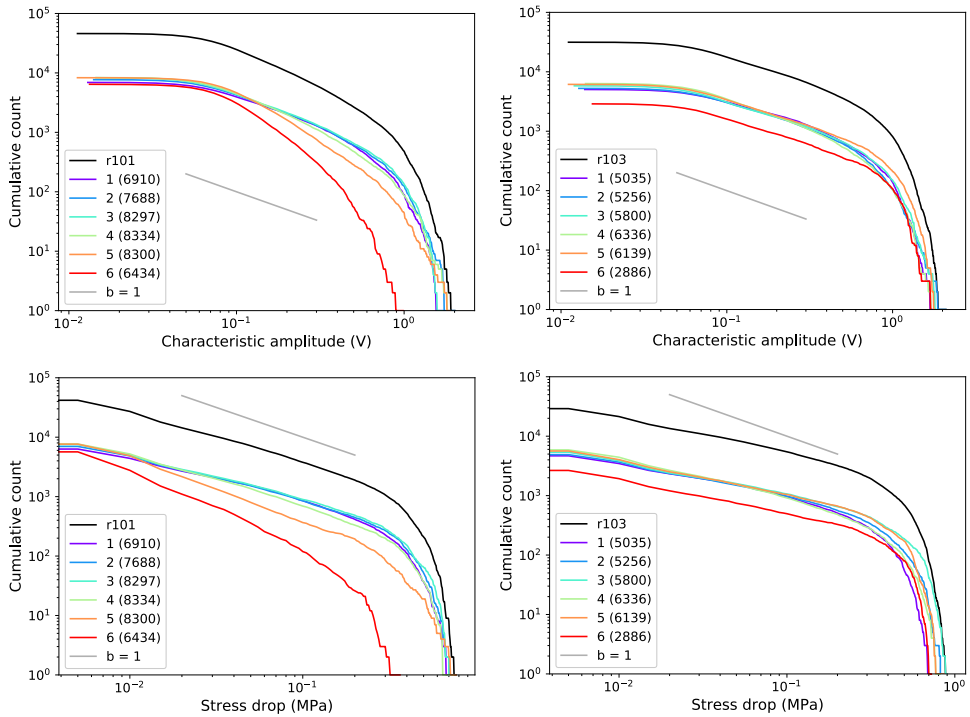


**Figure 2.10:** Time-lapse distributions of AE characteristic amplitudes and stress drops for r101 (left) and r103 (right). The black lines include all the events detected during shearing, excluding those that occurred during the first 1000 s of shearing. Each colored line represents 30 minutes. The number of events that occurred during each window is shown in parentheses. The shape of the curves from r103 is representative for r086 and r097 as well. Note the change in proportionality of small and large events in r101 during the last two windows (orange and red curves) of the experiment.

finer material has a particle size of about  $75 \mu\text{m}$ . SEM photomicrographs of glass beads from r086 (Figure 2.11 a, b, and c) show that particles were damaged to varying degrees. The majority of the inspected particles showed evidence of surface wear. Some particles appeared to be intact and only very few were missing large parts.

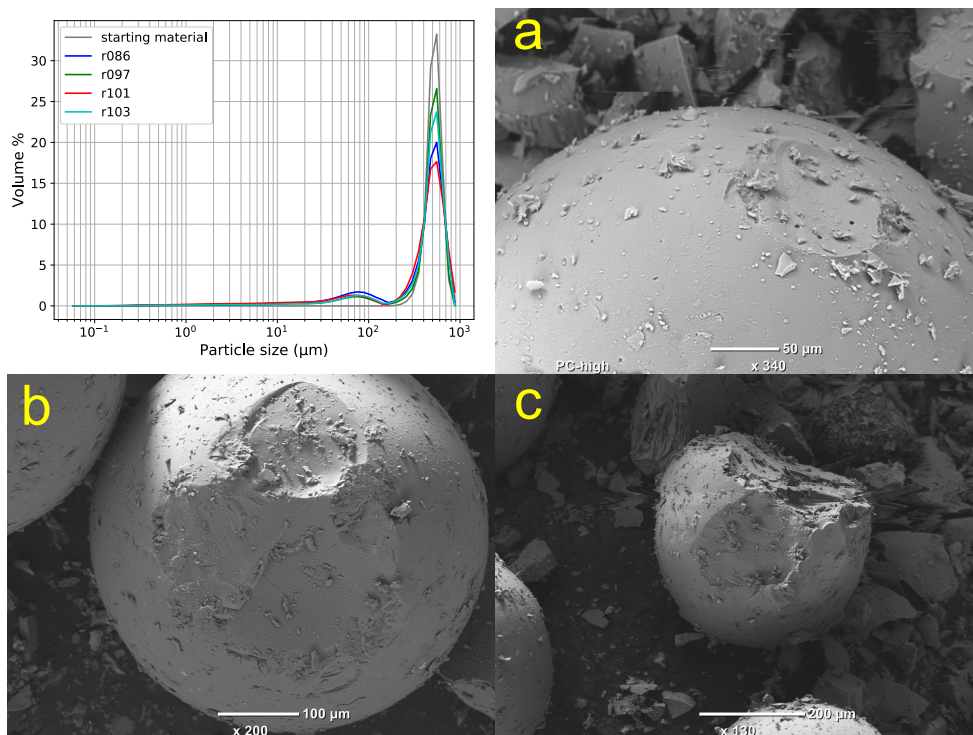


**Figure 2.11:** (top left) Particle size analysis (in  $\mu\text{m}$ ) of the starting material (grey) and of the salvaged samples (colored). Note the appearance of particles smaller than  $150\ \mu\text{m}$  in the salvaged samples. These particle sizes were not present in the starting material. (a, b, c) Post-experiment SEM micrographs of damaged glass beads from sample r086. The flakes covering the beads are a by-product of frictional wear.

## 2.5 Discussion

### 2.5.1 What do the estimated AE source locations represent?

The primary type of data we used to calculate AE source locations was first arrival times of AE signals. In particular, we measured the arrival times of the first wave to reach each receiver. We assume that the possible sources of elastic waves are either due to frictional interactions, i.e. rolling and/or sliding, between particles, or between particles and the walls of the sample chamber, or due to particle abrasion. In this context, we posit that each AE hypocenter represents the location of the initial force chain failure, that eventually lead to a cascade (avalanche), i.e. an instability accompanied by a stress drop.

### 2.5.2 Influence of sample thickness evolution on AE productivity

Prolonged shearing reduced the variability in initial sample thickness (Figure 2.4) as well as the average sample thickness itself (Figure 2.3). For the first 1000 s of shearing, the initially thickest part of the sample was the source of more AE events per mm of displacement than the thinnest part (Figure 2.4). The initial variability in sample thickness is either due to local differences in the concentration of particles or local differences in the microstructure, i.e. the arrangement of the particles. Since the starting particle size distribution is relatively narrow (Figure 2.11), the latter option seems more plausible.

We mentioned earlier that the volumetric response of our samples appears to have been more complicated (Figure 2.6) than that reported by other authors (e.g. Jiang et al. 2017; Anthony and Marone 2005). It is possible that this difference is due to the position of the LVDT that is responsible for measuring normal displacement (Figure 2.1). In its current position, the LVDT measures the vertical displacement of the gearbox housing (which sits just below the bottom piston) relative to the frame of the apparatus. The measurement is performed at the edge of the frame, whereas the sample assembly is situated at the center, along the axis of rotation. These characteristics could result in over- or underestimation of the true change in sample thickness, unless the volumetric response is homogeneous along the sample.

### 2.5.3 Implications for granular micromechanics

The consistent shape of the normalized CCDs of RTs and inter-event distance in Figure 2.8 (bottom row) suggests that, for the particular set of experimental conditions used here, sample variability does not affect the frequency of frictional instabilities and the spatial distribution of the nucleation sites. The inter-event distance CCDs suggest that the AE events originate from uniformly distributed loci. The distributions of RTs (Figure 2.9) can be described by a modified gamma distribution, similar to what other authors have shown for natural and mining-related seismicity, as well as rock fracture experiments (Corral, 2004; Davidsen et al., 2007; Davidsen and Kwiatek, 2013). Contrary to the exponential distribution, that describes a “memoryless”, randomly repeating process, the gamma distribution implies the presence of “memory” in the system. The mechanism that gives rise to such a property is not known.

The significant variability in friction (Figure 2.3) is likely due to the

inconsistent behavior of the load cells that are used to measure reaction torque (lw1 and lw2 in Figure 2.1). Subsequent calibration tests have shown that they respond non-linearly to forces that are not aligned perpendicular to their load-sensing elements. Figure 2.12 shows that although the apparent torsional stiffness measured during stress drops is variable, stress drops are overall proportional to displacements. This suggests that the proportionality between stress drop and AE characteristic amplitude (Figure 2.7) is also valid. However, due to the non-linear behavior of the force transducers we are unable to determine the absolute values of shear stress, nor the accuracy of the value of individual stress drops.

Our post-experimental particle size and SEM analyses suggest that particle slip occurs mainly with surface damage to the particles involved, similar to what other authors have observed (Scuderi et al., 2014, 2015). The generation of particles of 30-105  $\mu m$  in diameter (Figure 2.11, colored curves in top left panel) during shearing is in agreement with the size of the surface scars on the larger particles, as seen in the SEM photomicrographs (Figure 2.11, top right and bottom left).

#### 2.5.4 Comparison with seismicity

Our laboratory approach is a simplified analog of natural frictional interfaces inside granular or pulverized materials. In particular, the experiments we present here were designed to simulate an interface that slides intermittently, rather than continuously, while being loaded at a constant displacement rate. That is a laboratory approximation of the sliding behavior of locked, seismogenic fault zones. The distributions of AE amplitudes and stress drops show linear portions, similar to frequency-magnitude distributions that describe natural seismicity (Ben-Zion, 2008) as well as other granular systems (Michlmayr et al., 2012). Another feature of the distributions of stress drops and AE characteristic amplitudes is the exponential truncation at their respective high ends. This feature is similar to the truncation of frequency magnitude distributions of natural earthquakes (Sornette and Sornette, 1999). In our case, the truncation at high stress drops/characteristic amplitudes is probably due to the finite size of the sample, and the applied normal stress; parameters that can easily be changed to test this hypothesis. These parameters impose a limit on the maximum released energy per frictional instability because they control the maximum amount of stress drop and slip. The overall shape of our distributions is similar to the Gutenberg-Richter model rather than the Characteristic Earthquake model discussed in Wesnousky (1994). However, it is possible that using a narrower initial particle size distribution of glass

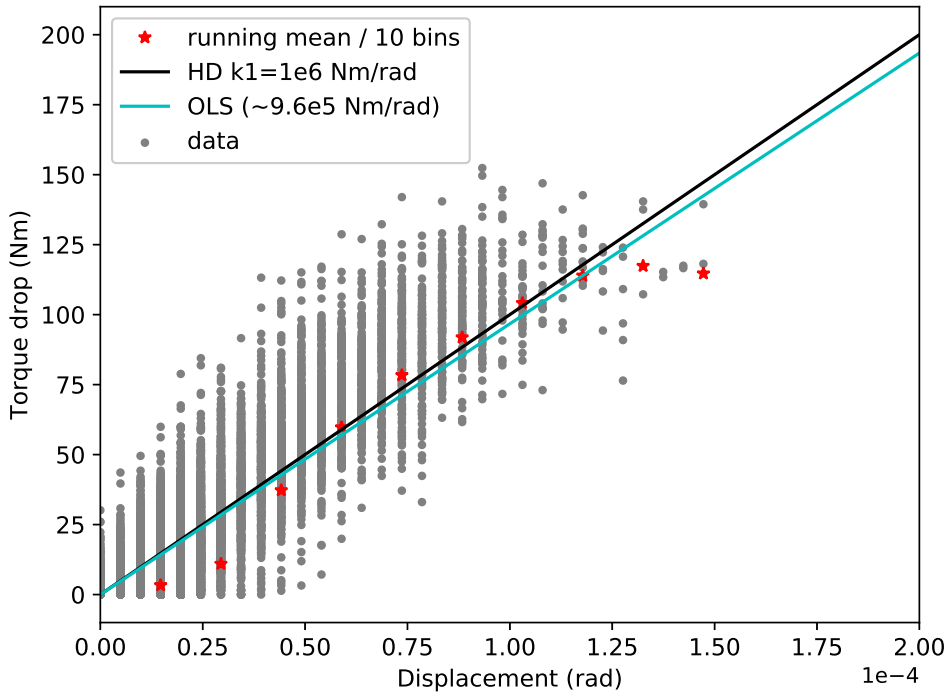


**Figure 2.12:** Torque drop (stress drop equivalent) versus associated displacement, for r103. The “binning” effect is due to the poor resolution of the displacement sensor. Note that the slope of the linear fit with zero intercept (cyan line) is similar to the torsional stiffness of the harmonic drive (black line), as stated by the manufacturer. The position of the lines relative to the data suggests that the distribution of torque drops for small ranges of displacement are skewed. The mean stiffnesses obtained from 10 consecutive bins are shown in red stars.

beads, or piston rings with larger grooves would lead to distributions that resemble the characteristic earthquake model. That would be due to the fact that in a narrow PSD situation, the number of feasible particle arrangements are fewer than in a wide PSD situation, assuming that particles do not break. Another notable similarity between our experiments and nature is the scaling of recurrence time distributions. This is particularly interesting, as one would reasonably expect that conditions of our experiments are drastically different than the ones that prevail in natural fault zones. Finally, we observe a proportionality between stress drop and AE characteristic amplitude, which can be considered as a proxy for magnitude. This is in

contrast with the generally assumed absence of scaling of stress drop with magnitude for natural earthquakes (Cocco et al., 2016). It is important to note that the features we have observed emerge from the purely mechanistic perspective of our experiments. In nature, there are numerous additional effects to consider, such as the presence of pore fluids, elevated temperature, chemical processes (Niemeijer et al., 2012) and complex fault zone geometry (Faulkner et al., 2010).

## 2.6 Conclusions

Capturing the properties of natural seismicity that are necessary for assessing earthquake hazard poses two major challenges, depending on the approach taken. On the one hand, statistical approaches suffer from the paucity of data of large magnitude earthquakes due to the limited period of instrumental observation and the inherent scaling of earthquake magnitudes. On the other hand, establishing robust links between the sliding behavior of seismogenic faults and the micromechanical processes operating in their vicinity is not a trivial task. Here we examine whether we can use rotary shear experiments on granular media to reconcile these two approaches. Laboratory experiments offer the opportunity to produce large amounts of data under controlled conditions, that can then be submitted to statistical treatment. We have developed a new rotary shear apparatus, equipped with a state-of-the-art mechanical data acquisition and acoustic emission (AE) monitoring system, that can record data from multiple sensors of various types synchronously. Using data collected at relatively high sampling rates, we were able to correlate the mechanical and acoustic manifestations of stick-slip instabilities. Thus, we have shown that the spatial distribution of force chains in sheared granular layers is widespread, and that during the first few millimeters of displacement, force chain failure is sensitive to pre-existing variability in the layer's thickness. The complementary cumulative distributions of AE amplitudes, as well as the discrete distributions of normalized recurrence times are remarkably similar to the equivalent distributions for natural seismicity. Our results suggest that it may be possible to use these statistics to extract information about the state of the microstructure of glass bead aggregates undergoing shear. Keeping in mind the advantages and limitations of simulating real-world systems with laboratory analogs, the statistics of our system show remarkable similarity to the respective observables of natural seismicity.



## Acknowledgements

We would like to thank Thony van der Gon Netscher and Floris van Oort for constructing the apparatus and for providing technical support. We also thank Eimert de Graaff for designing and manufacturing the AE transducers and Gerard Kuijpers for maintaining them. Hanneke Paulssen is thanked for fruitful discussions during the preparation of the manuscript. Chris Marone is thanked for providing the sample material.



## Chapter 3

# Spatiotemporal correlations of granular avalanches revealed by recurrence time distributions

### 3.1 Abstract

The recurrence time (RT) of natural earthquakes, with the exception of aftershocks, is not completely random, but can be described by the Corral (gamma) distribution. This implies the presence of non-trivial temporal correlations between earthquakes that do not belong to aftershock sequences. Here we demonstrate that this is also the case for stick-slip instabilities in sheared granular aggregates, and study the sensitivity of the RT distributions to the loading conditions. We performed rotary shear experiments on layers of glass beads, to measure the recurrence intervals of acoustic emissions related to stick-slip instabilities. The observed RT distributions are sensitive to the rate of shearing and to the normal stress applied onto the aggregate, and insensitive to the shear stiffness of the loading system. Our results show that there is a transition from approximately constant to time-decreasing hazard rate with increasing normal stress. We suggest that this transition is due to an increase in the rigidity of the load-bearing framework of the granular aggregates at higher confining stress. The exact mechanism for the development of “memory” in the system has yet to be determined.

## 3.2 Introduction

Determining the type of distribution that best describes the recurrence time (RT; also known as waiting time) of earthquakes in a certain region is important because it allows us to assess the rate of large, potentially destructive events. Such an assessment is empirical, as it is based on statistical inference. This is justified by the fact that seismicity exhibits a high degree of complexity (Ben-Zion, 2008; Kanamori and Brodsky, 2004; Shcherbakov et al., 2015). In order to begin to untangle the complexity of such a problem, it is reasonable to consider a simpler system as an analog, particularly one that can be manipulated in the laboratory. Such an analog system, that exhibits similar statistical behavior in terms of recurrence time scaling as natural seismicity, would likely allow us to link statistical observables to the physical mechanisms that give rise to complexity. Subsequently, the challenge would be to draw parallels between the physical mechanisms operating in the laboratory system versus those operating in the natural system.

Classically, mainshocks are considered independent events, resulting from a Poisson process (Utsu, 2002). Thus the probability density distribution of recurrence times  $\Delta t$  between mainshocks should be exponential:

$$D(\Delta t) = \lambda e^{-\lambda \Delta t} \quad (3.1)$$

where  $\lambda$  is the rate of the exponential distribution. However, aftershocks, a prime example of triggered earthquakes, have been shown to decay as described by Omori's law, modified by Utsu (Utsu et al., 1995):

$$n(t) = K(t + c)^{-p} \quad (3.2)$$

where  $n(t)$  is the rate of aftershocks at time  $t$  after the mainshock and  $K, c, p$  are empirical constants, with  $p$  typically between 1.0 and 1.5. One may expect that the RT distribution should be power-law for short RTs, which are dominated by Omori-Utsu aftershock sequences, and exponential for long RTs where Poissonian mainshocks dominate.

More recently, in the wake of the work by Bak et al. (2002) toward a unified law for earthquake recurrence, it has been shown that for natural seismicity (Corral, 2004), induced seismicity (Davidsen and Kwiitek, 2013), rock fracture experiments in the laboratory (Davidsen et al., 2007), and granular media (Chapter 2; also Lherminier et al. 2019) the probability density of RT for events (earthquakes, fractures, or slips) with magnitudes above the magnitude of completeness scales as follows:

$$D(\Delta t) = Rf(R\Delta t) \quad (3.3)$$

where  $R$  is the average rate, defined as the ratio of the number of events,  $N$ , divided by the total amount of time between event 1 and event  $N$  ( $R = \frac{N}{t_N - t_1}$ ), and  $f(R\Delta t)$  a scaling function. If the generating process is stationary,  $f(R\Delta t)$  can be approximated by a modified gamma distribution of the following form:

$$f(\theta) = C\theta^{-(1-\gamma)}\exp\left(\frac{-\theta^\delta}{B}\right) \quad (3.4)$$

where  $\theta = R\Delta t$ , and  $C, \gamma, \delta$ , and  $B$  constants.  $(1 - \gamma)$  is the slope of the power law section, whereas  $\delta$  and  $B$  determine how sharp the exponential truncation is.  $C$  places the entire distribution up or down along the y axis  $D(\Delta t)/R$ . This surprisingly robust result suggests that there is an intermediate regime, between the Omori-Utsu- and exponential-type, with a slope between 0.2 and 0.3 for natural and induced seismicity, as well as for rock fracture experiments. This intermediate-RT power-law scaling suggests that some earthquakes that do not belong to aftershock sequences are also correlated in time. In fact, due to the monotonically decreasing shape of the hazard function of equation (3.4), the probability of another earthquake decreases as time from the last event passes (Corral, 2004, 2005). For comparison, the hazard function of the exponential distribution is constant:  $h(\Delta t) = \lambda$ , where  $\lambda$  is the rate of the exponential distribution. This difference in the hazard functions underlines the necessity of understanding the nature of RT distributions in order to improve probabilistic hazard assessment.

Several authors have argued that the empirical RT scaling proposed by Corral is not universal in time, based on theoretical considerations. It has been shown theoretically by Molchan (2005) that, assuming randomly occurring mainshocks and power-law occurrence of aftershocks, a stationary random process would generate exponentially distributed RTs. Thus equation 3.4 is not universal because it does not describe aftershock sequences that are prevalent at short RTs. Molchan also argued that the parameter  $1/B$  in equation 3.4 is proportional to the number of mainshocks in the catalog. Hainzl et al. (2006) showed that the shape of RT distributions depends on the amount of mainshocks in the catalog and therefore it is not universal. They argued that because of the lack of universality, the shape of the RT distribution can provide information about the frequency-magnitude distribution. Hainzl and coworkers also demonstrated that different types of RT distributions can be explained by the ETAS (Epidemic Type Aftershock Sequence) model, assuming Omori-Utsu-type scaling for short RTs with an exponential drop-off for large RTs without the need for any other mechanisms. A generalization

of the argument of Molchan (2005), as well as further support for the ability of the ETAS model to explain the observed RT distributions were provided by Saichev and Sornette (2007). A very appealing feature of the ETAS-based approaches described here is that they do not make any assumptions about specific events in terms of the foreshock-mainshock-aftershock paradigm.

Here we study a simple laboratory analog system that exhibits RT scaling that is similar to that of natural seismicity. We attempt to link the statistical behavior of RTs of our system to the physical mechanisms that are responsible for its behavior, by investigating the effects of changing the normal stress, rate of rotation and loading system stiffness. Because our experiments are performed at conditions that prohibit us from using direct observation methods, we rely on observables from non-invasive AE methods to understand granular flow in the context of force chain network development and failure. Furthermore, we draw parallels between the mechanical phenomena that occur in our experiments and the much more diverse physicochemical processes that drive natural seismicity, yet give rise to a similar type of complexity.

### 3.3 Methods

We generated laboratory quake catalogs by performing room temperature friction experiments on glass bead aggregates, using the rotary shear apparatus described in Chapter 2. The main advantage of the rotary shear configuration is its capability to achieve large shear displacements. Glass bead aggregates have been previously used to investigate the mechanics of granular shear, due to the spherical shape of the particles, which allows for comparisons with discrete element method (DEM) models of granular flow (e.g. Ferdowsi et al. 2013; Morgan and Boettcher 1999). Glass bead aggregates exhibit stick-slip behavior when sheared at room temperature conditions (See Chapter 2; also e.g. Anthony and Marone 2005; Mair et al. 2002). Glass beads are brittle and chemically inert in the timeframe and under the conditions that prevail in our experiments. The experiments were performed in the non-fracture regime for glass bead aggregates (Mair et al., 2002), using particles with a mean starting diameter of approximately  $500 \mu\text{m}$  (see Chapter 2).

We performed our experiments using the apparatus and procedures described in detail in Chapter 2. The procedure of the experiment is the following: an annular-shaped flat layer (approximately 4.5 to 5 mm thick) of glass beads is confined between two annular steel pistons. Two more rings prevent the sample from spilling from the sides. The entire sample assembly is then placed in the rotary shear apparatus, which is capable of applying

normal stress and can rotate the lower steel piston at a constant rate. The top piston is jammed against a torque reaction frame. The amount of normal stress and the rate of rotation of the loading point are controlled by independent servo-controllers. The apparatus is equipped with several force and displacement transducers that measure normal (axial) force and displacement, torque, and angular displacement. After the experiment, these measurements can be converted to time series of normal stress and displacement, and shear stress (albeit with significant uncertainty as to the absolute value; see Chapter 2) and displacement. For the experiments presented here, we used 5 kN load cells to measure reaction torque, instead of the 20 kN load cells used in Chapter 2. Additionally, an acoustic emission (AE) system allows us to record waveforms (5 ms duration) from an array of 16 transducers installed inside the two steel pistons. This allows us to generate a catalog of AE events containing the triggering timestamps as well as source locations that were calculated using the procedure described in Chapter 2. In brief, we calculated the location of AE sources assuming a single velocity model and linear ray paths, justified by the long period content of the signals.

We investigated systematically the effect of the following three parameters on the recurrence time distributions of AE events: applied normal stress, load point rate of rotation and the torsional stiffness of the apparatus (Table 3.1). The torsional stiffness was controlled by sets of Belleville washers (see section 3.7.5). The more compliant the apparatus is, the larger the amount of potential energy it can store compared to a stiff apparatus, for a given amount of torque or shear stress. It is part of the stored energy that is released, mostly as heat and elastic waves, during a frictional instability.

To obtain the recurrence time (RT) distributions, we followed the procedure outlined in Corral (2004) for each experiment individually. It is important to note that the treatment of RTs does not require prior assumptions about foreshock-mainshock-aftershock relations between events. We began by selecting all of the AE events that occurred during shearing, excluding the first  $20^\circ$  of displacement. We excluded the AEs that occurred during the first  $20^\circ$  of shearing to eliminate any artifacts resulting from variability in the starting microstructure of the samples. Furthermore we excluded events with AE amplitude lower than the amplitude of completeness ( $A_c$ ). We defined  $A_c$  as the peak of the AE amplitude probability density distribution. Subsequently, we calculated the recurrence times  $\Delta t = t_{i+1} - t_i$ , for the  $N$  consecutive AE events. We calculated the probability density  $D(\Delta t)$  by distributing the RTs into bins of exponentially (base of 10) increasing width and then dividing the frequency of each bin by

**Table 3.1:** Table of experiments.  $\sigma_n$ : normal stress. RR: rate of rotation.  $\kappa$ : torsional stiffness of the apparatus.

Experiment ID	$\sigma_n$ (MPa)	RR ( $^\circ/s$ )	$\kappa$
r122	8	0.02	high
r123	8	0.02	high
r124	8	0.02	high
r137	8	0.04	high
r139	8	0.04	high
r136	8	0.08	high
r138	8	0.08	high
r135	8	0.02	low
r127	4	0.02	high
r129	4	0.02	high
r130	4	0.02	med
r132	4	0.02	intermediate
r133	4	0.02	low
r134	4	0.02	low
r126	2	0.02	high

the product of  $(N - 1)$  with the width of that bin.

### 3.4 Results

All of the samples exhibited irregular stick-slip behavior accompanied by acoustic emission events, similar to what has been shown in Chapter 2. We found that, for each experiment, the rolling mean of the rate of events and AE source locations and the rolling variance of the AE source locations remain relatively constant during shearing, so the generating process of AE events can be considered stationary and thus 3.3 and 3.4 are applicable. For all of the experiments, the coefficient of variation, CV (Kagan and Jackson, 1991a), of the RTs remains stable and larger than 1, as long as there is a sufficient number of events that survive the imposed amplitude threshold (Figure 3.1). The probability density distributions  $D(\Delta t)$  of repeat experiments are highly reproducible (see section 3.7.3) and stable in the threshold amplitude range of stable CV.

Increasing the load point rate of rotation or the normal stress results in an increase in the probability density of small RTs and a decrease in the maximum  $\Delta t$  (Figure 3.2). However, the effect of changing shear stiffness was practically negligible.



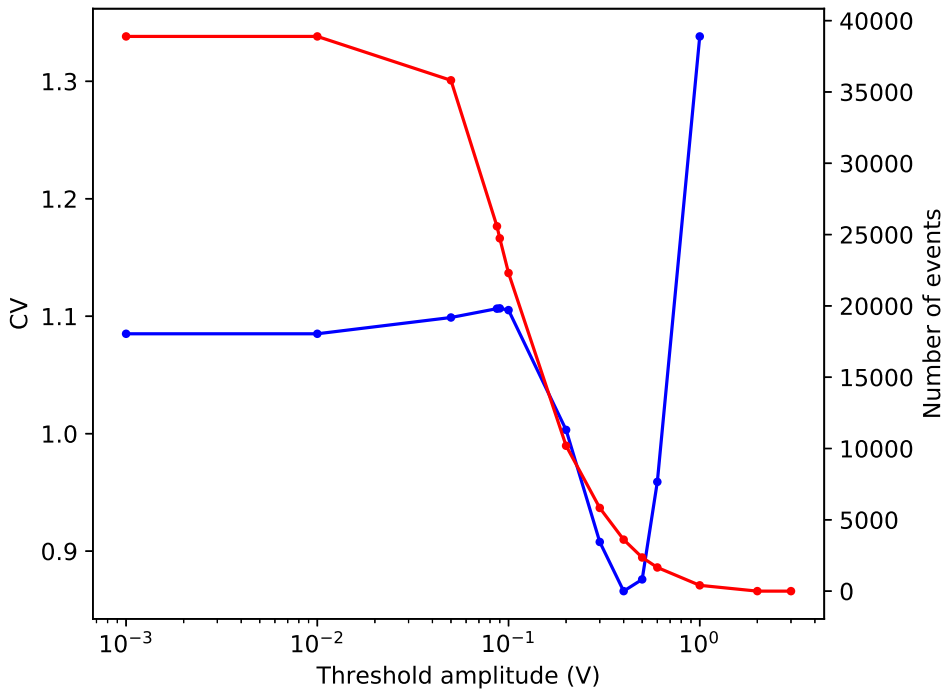


**Figure 3.1:** Change in the coefficient of variation (blue curve) as a function of threshold amplitude, for experiment r122. The number of events with amplitude larger than the threshold are shown in red. The amplitude of completeness ( $A_c$ ) for r122 is 0.083 V, based on the AE amplitude pdf. Note that CV is largely constant and larger than 1 for threshold amplitudes below 0.1 V. Similar curves were obtained for the rest of the experiments presented here, albeit with different peak number of events and maximum AE amplitudes.

The effect (or lack thereof) of changing normal stress, rate of rotation and shear stiffness becomes more apparent when we consider the probability density adjusted by the mean rate of occurrence,  $D(R\Delta t)$ , with  $\theta = R\Delta t$ . Data obtained at different load point velocities or with different torsional stiffness of the apparatus, collapse onto the same respective Corral-type distributions (Figure 3.3, upper panel).

The applied normal stress clearly has an effect on the power-law portion of the Corral distribution (Figure 3.3, lower panel): at the highest normal stress (8 MPa),  $(1 - \gamma)$  is approximately 0.2, whereas at the lowest normal stress (2 MPa),  $(1 - \gamma)$  is approximately 0.07. Thus the data for 2 MPa can almost be fitted with an exponential distribution. The data for the intermediate normal

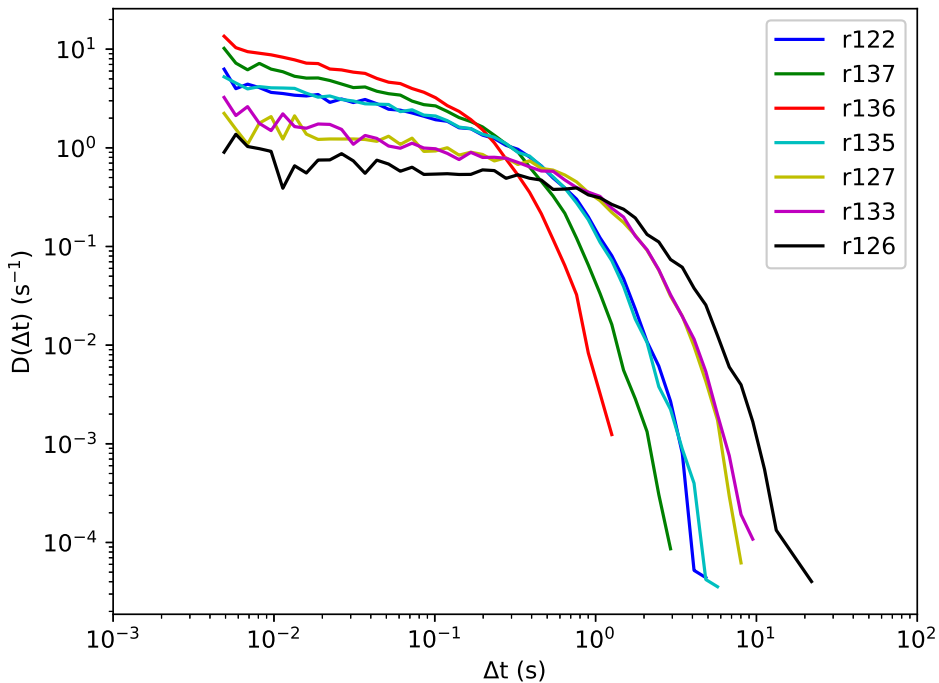


**Figure 3.2:** Probability density distributions of RTs from 4 different experiments. Increasing normal stress (r127 vs r122) and rate of rotation (r122 vs r136) changes the shape of the distribution, whereas lowering the apparatus stiffness (r122 vs r135 and r127 vs r133) does not have any significant effect.

stress (4 MPa) can be described by an intermediate value of  $(1 - \gamma) = 0.1$  approximately. The quoted  $\gamma$  values were obtained via manual optimization of the ratio between the data and the Corral distribution (see examples in the Supplementary material section), using the method of moment estimation to obtain a starting guess. In addition, we used maximum likelihood estimation to fit the standard gamma distribution to the data. The results are shown under section 3.7.

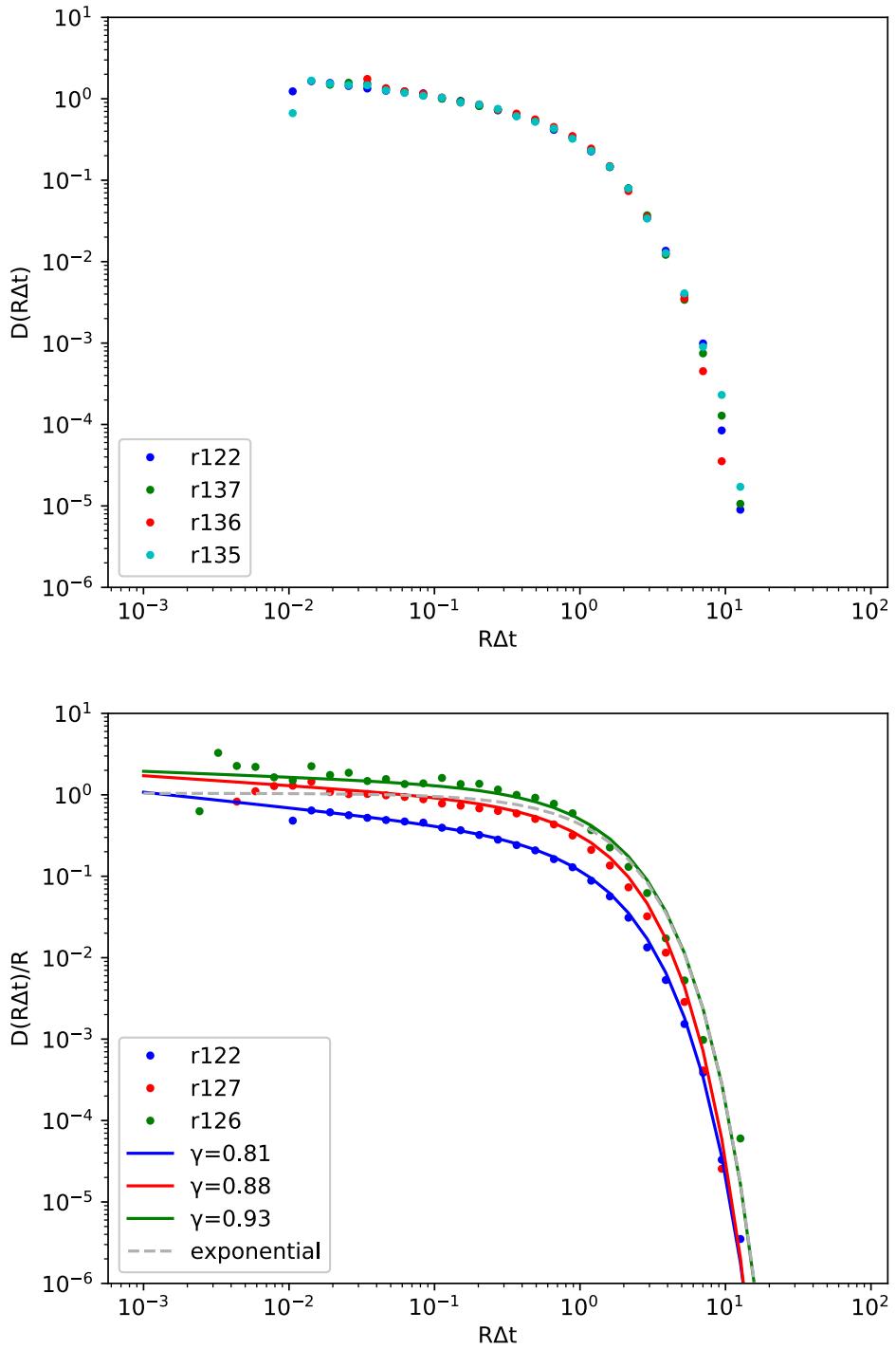


Figure 3.3

**Figure 3.3:** *Upper panel: comparison of the normalized RT distributions for several experiments at 8 MPa. The Corral-type shape ( $1 - \gamma = 0.2$ ) is preserved, regardless of the change in rate of rotation (r136 and r137) or stiffness of the apparatus (r135). Lower panel: Comparison of Corral distributions fitted to three experiments at different normal stresses. Blue: r122; 8 MPa,  $\gamma = 0.81$ . Red: r129; 4 MPa,  $\gamma = 0.88$ . Green: r126; 2 MPa,  $\gamma = 0.93$ . The exponential distribution with rate equal to the green curve is shown for comparison.*

### 3.5 Discussion

This work has four goals: first, to demonstrate that the recurrence time statistics of sheared glass bead aggregates show similar scaling behavior to natural seismicity; more specifically, they can be described by an exponential or a Corral distribution. Second, to determine the sensitivity of the RT distributions to the applied normal stress, rate of rotation, and machine stiffness. Third, to explain the observed RT scaling behavior in terms of the force chain concept and explore its implications for granular flow. And lastly, to draw parallels between our simplified laboratory analog and the crustal systems that host natural seismicity.

Our results clearly demonstrate that the probability density distribution of the raw recurrence times is sensitive to normal stress and rate of rotation but not to the shear stiffness of the loading system. Among these three factors, the sensitivity to rate of rotation is perhaps the least surprising. An increase in the loading rate displaces the truncation of the RT distribution to the left, i.e. to shorter recurrence intervals, while at the same time resulting in an increase of the probability of small RTs. Perhaps the most surprising result is the lack of sensitivity of the RT distributions to the shear stiffness of the loading system. Assuming constant stress drop, sample peak strength and rate of rotation, a decrease in the stiffness of the loading system should result in longer recurrence times between consecutive events. Because the uncertainty in the torque (shear stress) data is significant (see Chapter 2), we have not pursued this further.

Our results show that the slope ( $1 - \gamma$ ) of the normalized RT distributions is positively correlated with normal stress (Figure 3.4). The relationship is linear. For  $1 - \gamma = 0$  in equation (3.4), we obtain the exponential distribution (equation 3.1), which implies that the recurrence times are independent. Note that for  $\delta = 1$  in equation (3.4)  $\lambda = \frac{1}{B}$ , i.e. the rate of the exponential distribution is equal to the inverse of parameter  $B$  in the gamma distribution.

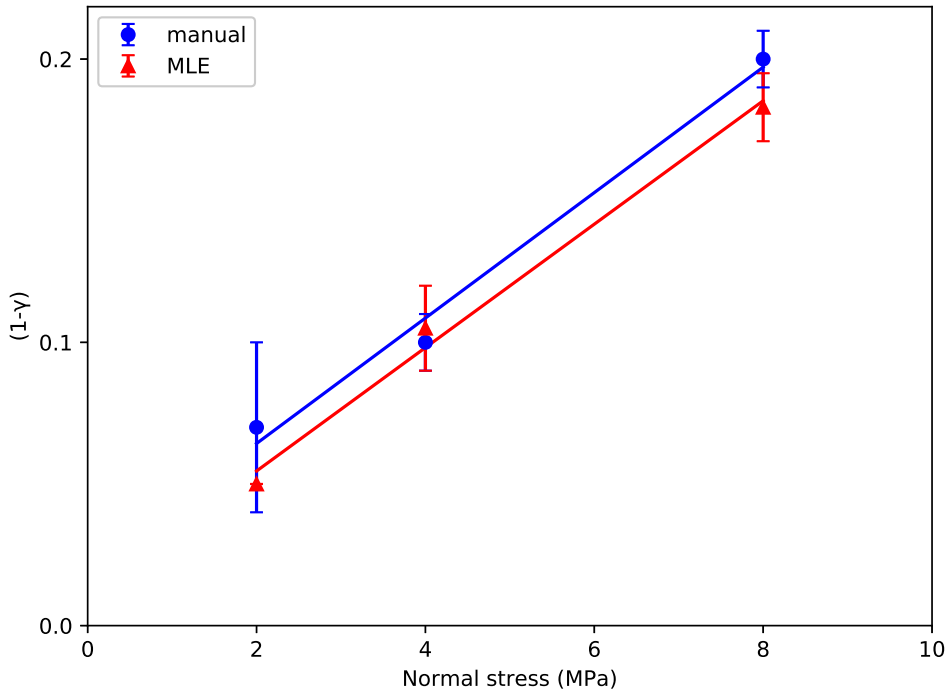


**Figure 3.4:** Values of  $(1 - \gamma)$  over the range of normal stress values of our experiments. Data in blue have been obtained via manual fitting of the Corral distribution; the error bars are indicative of the uncertainty in the estimation of  $\gamma$ . Data in red represent mean  $\gamma$  values, obtained via MLE, from the relevant experiments; the error bars correspond to  $\pm 1$  standard deviation. Both methods show that the slope  $(1 - \gamma)$  of the power-law portion of the Corral (gamma) distribution is proportional (at a rate of approximately  $0.02 \text{ MPa}^{-1}$ ) to the applied normal stress in the range tested (2 to 8 MPa). Values from rock fracture experiments, natural and induced seismicity plot outside the space of this plot, toward its upper-right corner (see Discussion).

Figure 3.4 then shows that upon increasing normal stress a power law regime emerges for  $R\Delta t < 1$ . This suggests the emergence of correlations due to the increase in normal stress, likely because the mechanical coupling between neighboring particles becomes stronger.

Another way to look at the relationship between normal stress and recurrence time distributions, is in terms of the hazard function. Regardless of the distribution, the hazard function  $h(x)$  is given by the formula:

$$h(x) = \frac{f(x)}{S(x)} \quad (3.5)$$

where  $f(x)$  is the probability density function of a continuous random variable  $X$ , and  $S(x)$  is the survivor function. Here  $x = R\Delta t$ . The hazard function of the exponential distribution is constant (equal to the rate parameter  $\lambda$ ), suggesting that at low normal stress (where  $R\Delta t$  scales nearly exponentially), events occur at an approximately constant rate (Figure 3.5). Such a system is “memoryless”. With increasing normal stress to 4 and 8 MPa our data show a clear transition to the Corral (modified gamma) distribution (Figure 3.4, Figure 3.4). Because  $\gamma < 1$ ,  $h(R\Delta t)$  peaks immediately after the last event and decreases with increasing  $R\Delta t$ , until it falls to the “background” rate  $\lambda$  or  $\frac{1}{B}$  (Figure 3.5). This implies the emergence of correlations between recurrence times as a function of increasing normal stress.

We believe that the transition from an exponential to a Corral/gamma distribution (or equivalently, the decrease in  $\gamma$  as normal stress increases) reflects a change in the micromechanics of granular shear. A suitable framework to discuss such a transition in the context of granular media is the concept of force chain networks. Force chains are arrangements of load bearing particles inside a stressed granular medium (Jaeger et al., 1996). Let us consider the case of two granular aggregates with similar particle size distributions: one under low normal stress and the other under high normal stress, yet not so high as to result in particle fracturing (Mair et al., 2002). The aggregate under high normal stress would have a more extended force chain network than its counterpart under low normal stress, because the higher normal stress would likely be experienced by a larger number of grains. The resolved normal stress between contacts of individual particles should be, on average, higher, therefore the mechanical coupling of individual particles would increase. In addition, we expect an increase in the average coordination number, i.e. the average number of particles that are in contact with a given particle (Aharonov and Sparks, 1999). These effects should result in a stronger, more brittle load bearing microstructure. Under low normal stress, such effects should be minimized, resulting in a more limited and compliant force chain network. In other words, we believe that the observed transition can be explained in terms of the change in rigidity of the load bearing framework as a function of normal stress. A rigidity transition related to the solid volume fraction of granular media has been observed in laboratory experiments as well as in numerical simulations (Aharonov and Sparks, 1999; Howell et al., 1999).

To explore the extent of the event correlations implied by the Corral

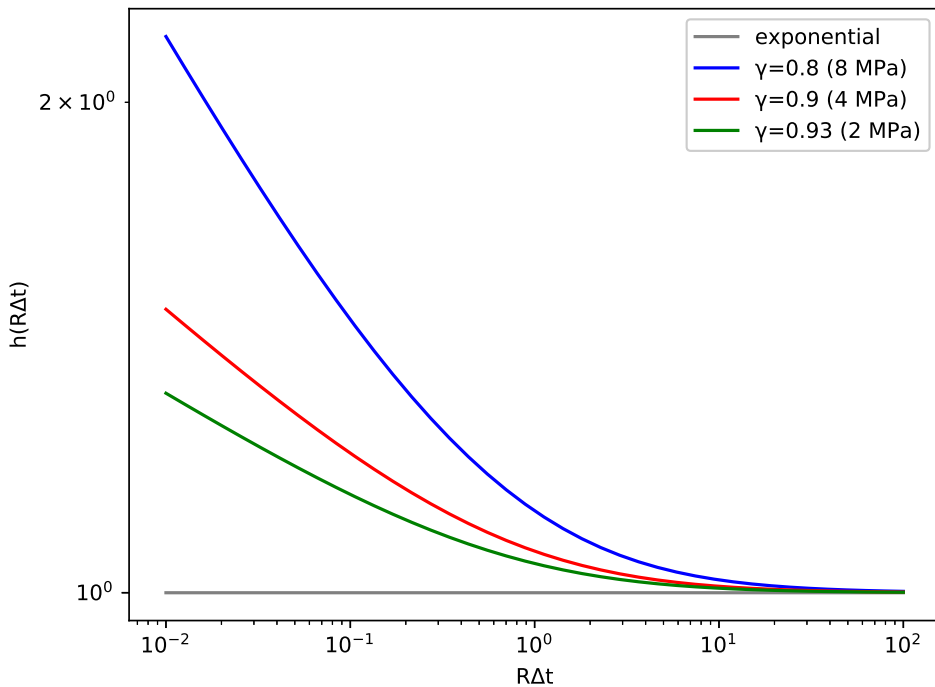


**Figure 3.5:** Hazard function for the exponential ( $\lambda = 1$ ) and the gamma (Corral) distribution (red:  $\gamma = 0.8$  and blue:  $\gamma = 0.9$ ;  $B = 1$  in both cases).

distribution, we performed the following analysis, which is based on the argument by Molchan (2005) and generalized by Saichev and Sornette (2007). Recall that these authors have proven theoretically that stationary seismicity comprised of independent, uncorrelated events should produce exponentially distributed recurrence intervals. Let us examine  $D(R^A \Delta t^A)$  and  $D(R^B \Delta t^B)$  for different regions (“slices”)  $A$  and  $B$  of a sample, as well as  $D(R^{AUB} \Delta t^{AUB})$  for the union  $AUB$ . To perform this analysis we divided the calculated AE source locations into four quadrants:  $q1=[000, 090)$ ,  $q2=[090, 180)$ ,  $q3=[180, 270)$ , and  $q4=[270, 360)$ , with number  $XYZ$  indicating the source location azimuth in degrees, relative to the same reference point in the top, stationary piston. We calculated  $D(R^{qx} \Delta t^{qx})$  for each quadrant  $x = [1, 4]$ , as well as  $D(R^{q1Uq3} \Delta t^{q1Uq3})$  and  $D(R^{q2Uq4} \Delta t^{q2Uq4})$ . For the rates  $R^{q1Uq3}$  and  $R^{q2Uq4}$  we used the mean of  $R^{q1}$ ,  $R^{q3}$  and  $R^{q2}$ ,  $R^{q4}$  respectively. We opted to analyze the unions of remote quadrants to avoid any potential bias due to events originating close to the boundary between two neighboring quadrants. The results for two cases of high and low normal

stress are shown in Figure 3.7 and Figure 3.8 respectively. The shape of the distribution remains the same in the case of r122 (8 MPa), whereas in the case of r126 it turns into exponential. Compared to the distributions for the whole samples, the distributions of the quadrants are shifted higher along the  $y$  axis, due to the different mean rates  $R$  used (see section 3.7.4). Because at high normal stress the shape of the distributions does not change, we infer that there are not only temporal but also spatial correlations between consecutive events with RTs in the power-law range. However at low normal stress, the distributions are exponential, suggesting the lack of correlations between the various slices of the sample.

This analysis provides indirect evidence of spatial correlations of AE source locations in the case of high normal stress, but not in the case of low normal stress. These results support the explanation proposed earlier, namely that the shape of the RT distribution reflects the rigidity of the microstructure of the sample. While it is not clear what the physical mechanism that effects such correlations is, the frictional stability of granular media is susceptible to vibrations (Johnson et al., 2008). Such vibrations can be produced by elastic waves generated during frictional instabilities (AE). It has been shown that the propagation of elastic waves through a granular medium depends on (but also affects) the mechanical coupling of the particles involved in the force chain network (Owens and Daniels, 2011).

Putting the findings of this study in a more general context, we have shown that the recurrence time of slip instabilities in sheared granular media is gamma-distributed, similar to the RTs observed in a number of other natural and artificial settings. The range of  $\gamma$  values we have measured in our experiments are lower than those reported by Lherminier et al. (2019) for rotary shear tests on 2-dimensional cylindrical piles (approximately 0.7), Davidsen et al. (2007) for rock fracture experiments (approximately 0.8), Davidsen and Kwiatek (2013) for induced seismicity (approximately 0.74), and Corral (2004) for natural seismicity (approximately 0.67). It is quite remarkable that all of the systems described above, that span scales from  $10^{-5}$  m to  $10^4$  m and from  $10^{-5}$  s to  $10^3$  s, exhibit very similar RT scaling. In fact, with the exception of the 2D experiments, it appears that there is a smooth transition from exponential to Corral-type RT distributions as a function of normal stress.

Let us now compare our system with natural seismicity. Most earthquakes nucleate in structurally complex parts of the lithosphere (Faulkner et al., 2010), that are hosts to an array of physicochemical processes (Niemeijer et al., 2012). It is therefore not surprising that natural seismicity exhibits complex behavior (Ben-Zion, 2008) that impedes our efforts to assess seismic hazard,



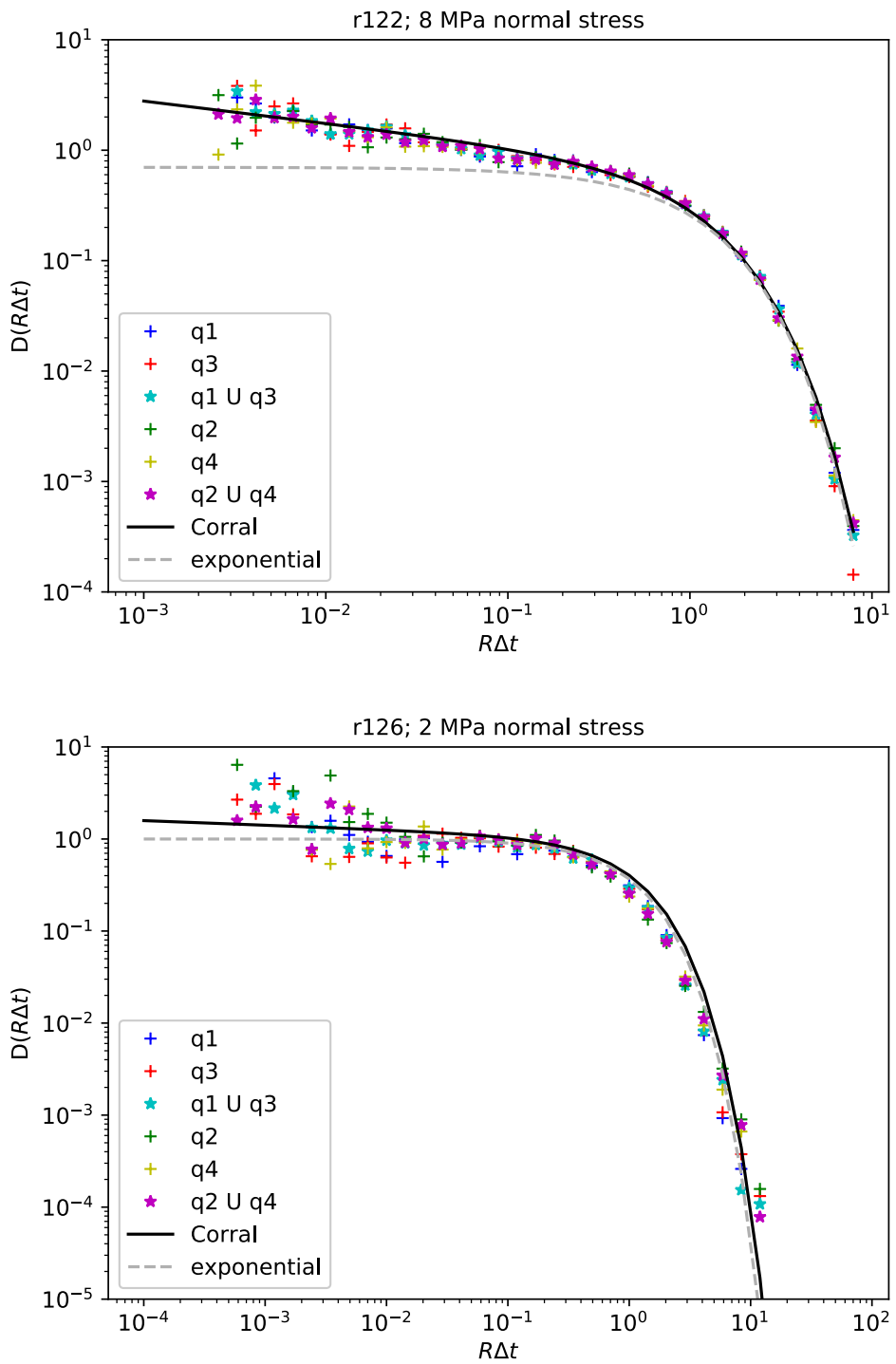


Figure 3.6

**Figure 3.6:** *Normalized probability density distributions of  $R\Delta t$  from experiments r122 (upper panel) and r126 (lower panel). The plots show the distributions of four quadrants and two unions. The exponential (dashed grey line) and Corral (black line) distributions are shown for comparison. In the upper panel (r122),  $1 - \gamma = 0.2$ . In the lower panel (r126),  $1 - \gamma = 0.05$ .*

let alone predict the occurrence of individual earthquakes. Our system has fewer degrees of freedom, yet exhibits comparable macroscopic complexity in terms of recurrence time and failure rate. Note that sheared granular media (both in the laboratory and in DEM simulations) and natural seismicity share similar frequency-magnitude distributions as well (Chapter 2; also Dahmen et al. 2011; Daniels and Hayman 2008; Ferdowsi et al. 2013; Geller et al. 2015; Hayman et al. 2011; Lherminier et al. 2019; Uhl et al. 2015). While this work as is does not identify the possible physical mechanisms behind the spatiotemporal correlations that exist in our system, it does provide strong evidence for their existence. We hope that this will provide further context for explaining the complexity we observe in natural systems.

### 3.6 Conclusions

The type of distribution of recurrence times of earthquakes is of particular interest due to the implications it has for seismic hazard estimation. Previous studies (Corral, 2004; Davidsen et al., 2007; Davidsen and Kwiatek, 2013) have shown that for a diverse set of systems the RT distributions can be described by a modified gamma distribution. Here, we have demonstrated that this is also the case for sheared glass bead aggregates under certain conditions. Furthermore, we have shown that there is a transition from (almost) exponential to Corral/gamma RT distributions, as a function of increasing normal stress. This can be interpreted as the development of “memory” in the system. Changes in the stiffness of the loading system do not affect the shape of the RT distributions significantly. Finally, our data provide indirect evidence for stress-dependent spatial correlations among the nucleation points of frictional instabilities, based on a theoretical argument about the expected statistical behavior of uncorrelated seismicity (Molchan, 2005). We suggest that the stress-dependency of 1) the shape of the RT distributions and 2) the spatial correlations between frictional instabilities, is due to the increase in rigidity of the load bearing framework of the material with increasing normal stress, which allows for more efficient propagation of mechanical vibrations. Nevertheless, the actual mechanisms that give rise to

the observed spatiotemporal correlations between granular avalanches, as well as earthquakes, remain unknown.

## **Acknowledgements**

We would like to thank Roberto Benzi for stimulating discussions and for his advice on the statistics of granular avalanches.

## 3.7 Supplementary material

### 3.7.1 Details about the statistical treatment of the data

In addition to the Corral distribution, we fitted standard gamma and exponential distributions to the  $R\Delta t$  data of each experiment, using MLE from the Scipy 1.1.0 package. Table 3.2, below, shows the results of the gamma parameter estimation, along with the results of the Kolmogorov-Smirnov (KS) test. Decreasing the threshold amplitude below  $A_c$  usually resulted in small changes to the fit parameters and to the KS test results. Two-sample KS tests, using multiple randomly generated distributions based on the fitted parameters, yielded higher  $p$ -values overall.

**Table 3.2:** Amplitude thresholds ( $A_c$ ), number of events ( $N$ ) with amplitude larger than the threshold, gamma distribution parameters ( $\gamma, B$ ), and Kolmogorov-Smirnov test results ( $D$  and  $p$ -value). The fitting was performed using MLE.

Exp. ID	$A_c$ (V)	$N(A > A_c)$	$\gamma$	$B$	$D$	$p$ -value
r122	0.87	25581	0.83	1.18	0.0053	0.47
r123	0.87	27407	0.82	1.19	0.0066	0.18
r124	0.87	26852	0.80	1.22	0.0069	0.16
r137	0.87	21652	0.82	1.20	0.0085	0.09
r139	0.87	16739	0.85	1.14	0.0130	7e-3
r136	0.87	17464	0.87	1.1	0.0092	0.1
r138	0.87	16750	0.84	1.13	0.0154	7e-3
r135	0.87	26778	0.85	1.15	0.0053	0.45
r127	0.043	10970	0.91	1.1	0.0132	0.04
r129	0.043	9783	0.88	1.13	0.011	0.19
r130	0.043	10027	0.84	1.18	0.0101	0.26
r132	0.043	10592	0.88	1.12	0.0156	0.01
r133	0.043	10650	0.87	1.14	0.0152	0.01
r134	0.043	12066	0.88	1.14	0.0093	0.25
r126	0.22	6177	0.95	104	0.0127	0.27

## 3.7.2 Examples of fitting the Corral distribution

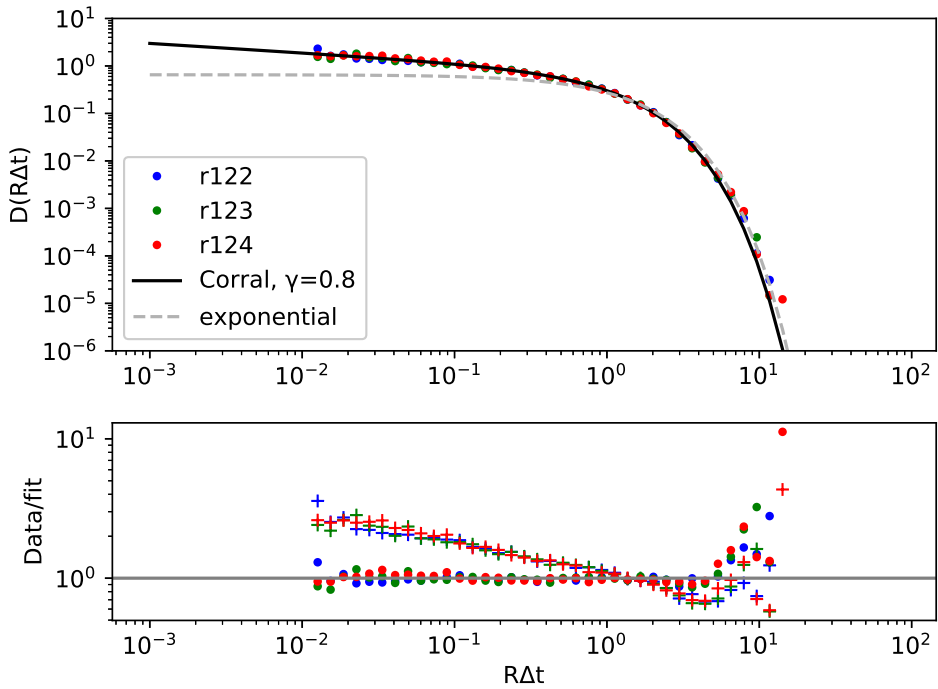


**Figure 3.7:** (top panel) Normalized probability density distributions of experiments  $r122$  (blue),  $r123$  (green), and  $r124$  (red). All three experiments were performed under the same conditions. Note the better fit of the Corral distribution (black line;  $1 - \gamma = 0.2$ ) compared to the exponential distribution (grey dashed line, rate=0.87). (bottom panel) Comparison of the ratio between the probability densities and each of the distributions. Dots correspond to the data/Corral ratio whereas crosses to the data/exponential ratio. The Corral distribution describes the data better than the exponential for a wider range of normalized recurrence times.

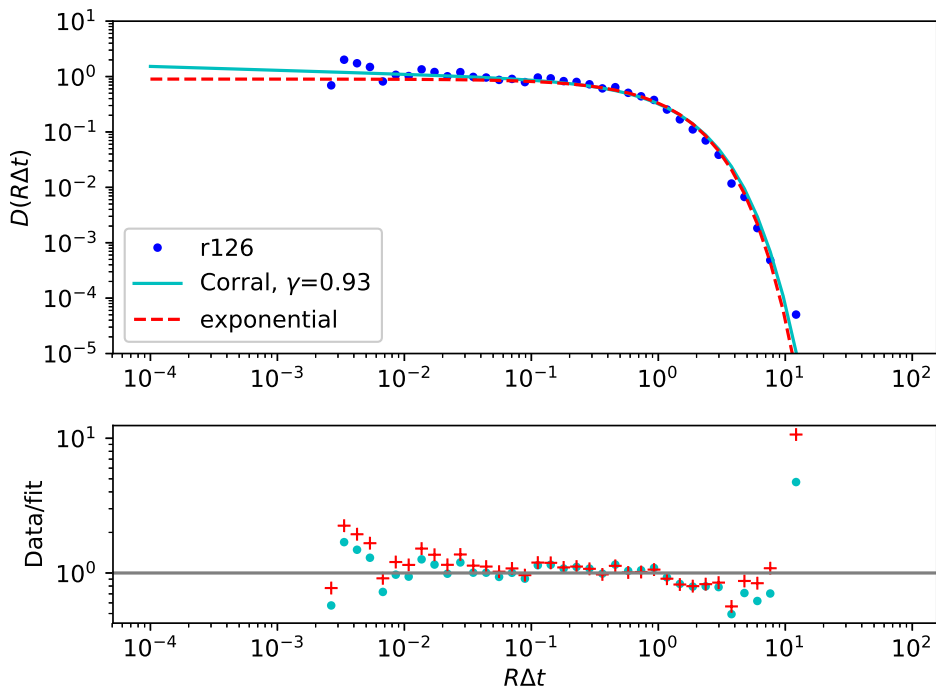


**Figure 3.8:** Normalized probability density for experiment r126 (lowest normal stress, 2 MPa). Note that, compared to the data for 8 MPa normal stress (Figure 3.9), the difference between the exponential (dashed red line, rate=1) and the Corral (cyan;  $1 - \gamma = 0.07$  approximately) fit is less obvious.

## 3.7.3 Reproducibility of RT distributions

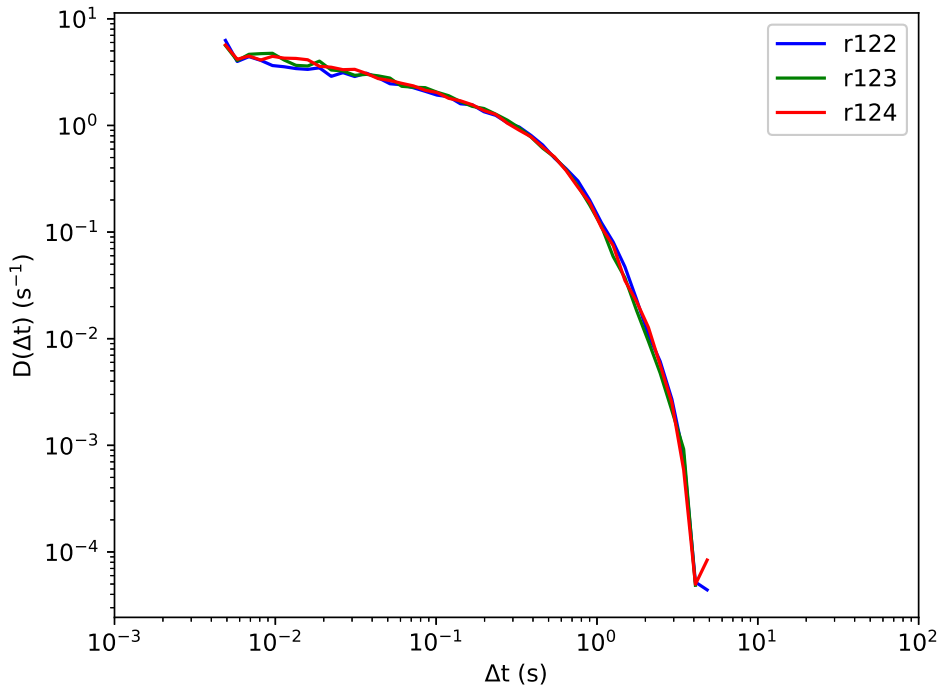


**Figure 3.9:** RT distributions of the experiments at:  $\sigma_n = 8$  MPa, rate of rotation =  $0.02$   $^\circ/\text{s}$ , high stiffness.

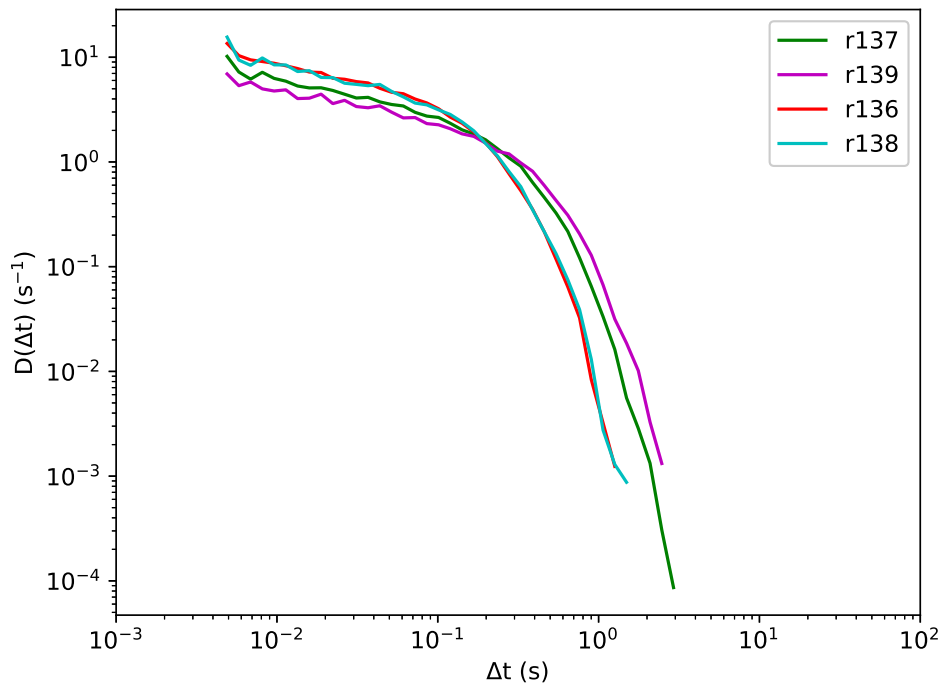


**Figure 3.10:** RT distributions of the experiments at:  $\sigma_n = 8$  MPa, rate of rotation =  $0.04$   $^\circ/\text{s}$  (r137 and r139), rate of rotation =  $0.08$   $^\circ/\text{s}$  (r136 and r138), high stiffness.



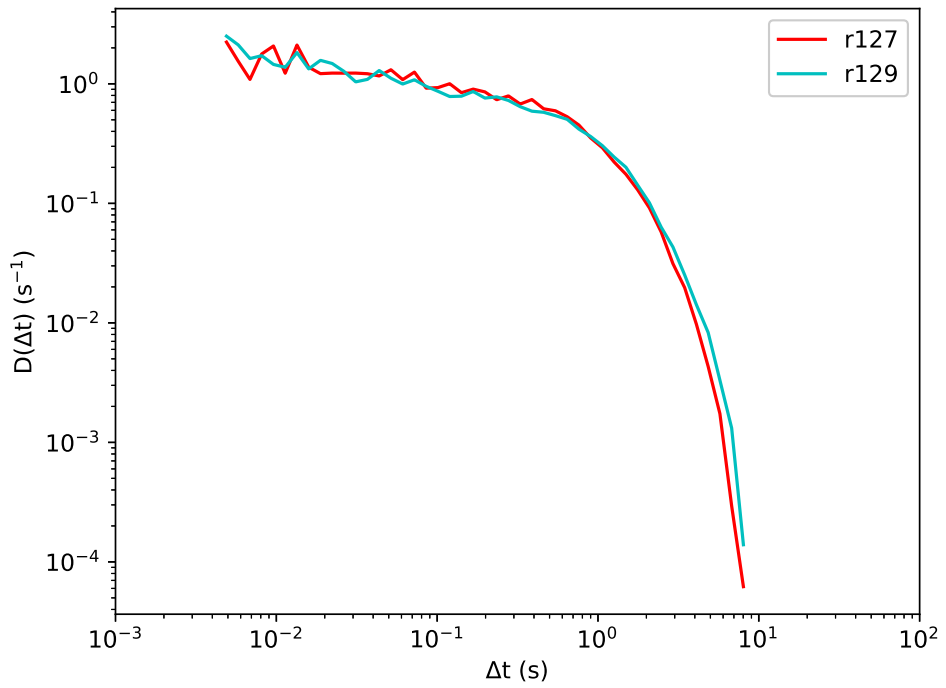


**Figure 3.11:** RT distributions of the experiments at:  $\sigma_n = 4$  MPa, rate of rotation =  $0.02$   $^\circ/s$ , high stiffness.

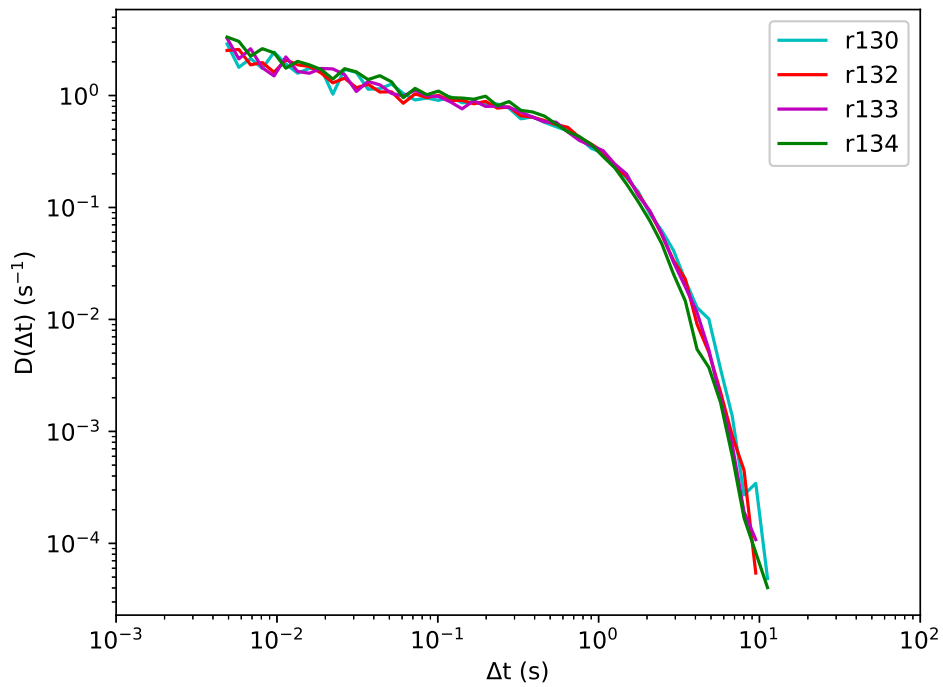


**Figure 3.12:** RT distributions of the experiments at:  $\sigma_n = 4$  MPa, rate of rotation =  $0.02$   $^\circ/\text{s}$ , intermediate stiffness (r130 and r132), and low stiffness (r133 and r134).

### 3.7.4 RT distributions of slices

Here we show more detailed results of the RT analysis performed on various slices of r122 (8 MPa) and r126 (2 MPa), as discussed in section 3.5. We compare the normalized RT distributions of the entire sample, its halves, its quadrants and two unions of remote quadrants.

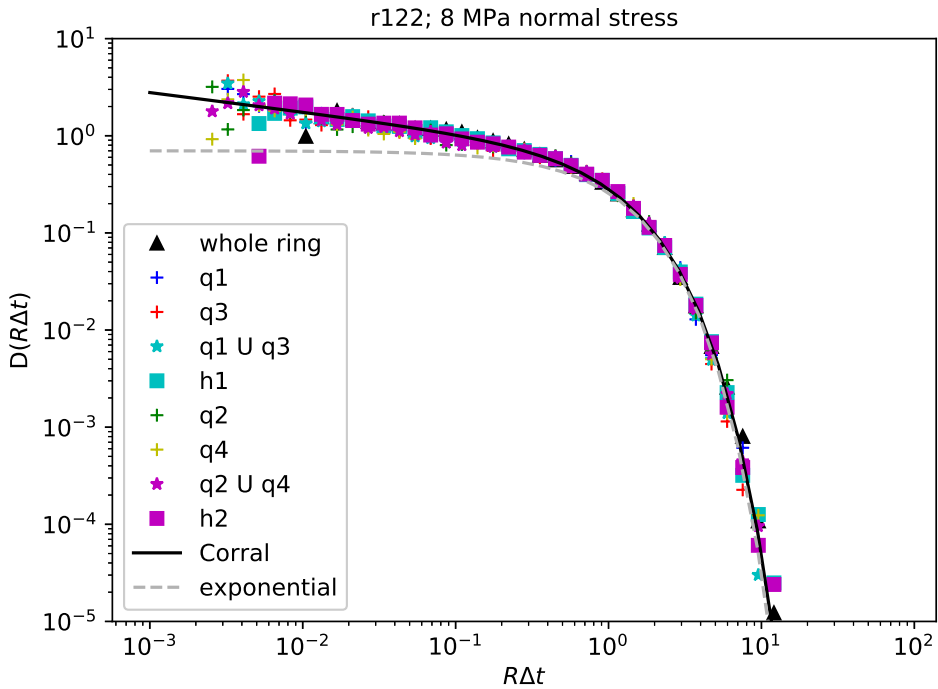


**Figure 3.13:** Normalized probability density plots of various slices of sample r122. h1 and h2: halves. q1, q2, q3, q4: quadrants. The black line is the Corral distribution, with  $(1 - \gamma) = 0.20$ .

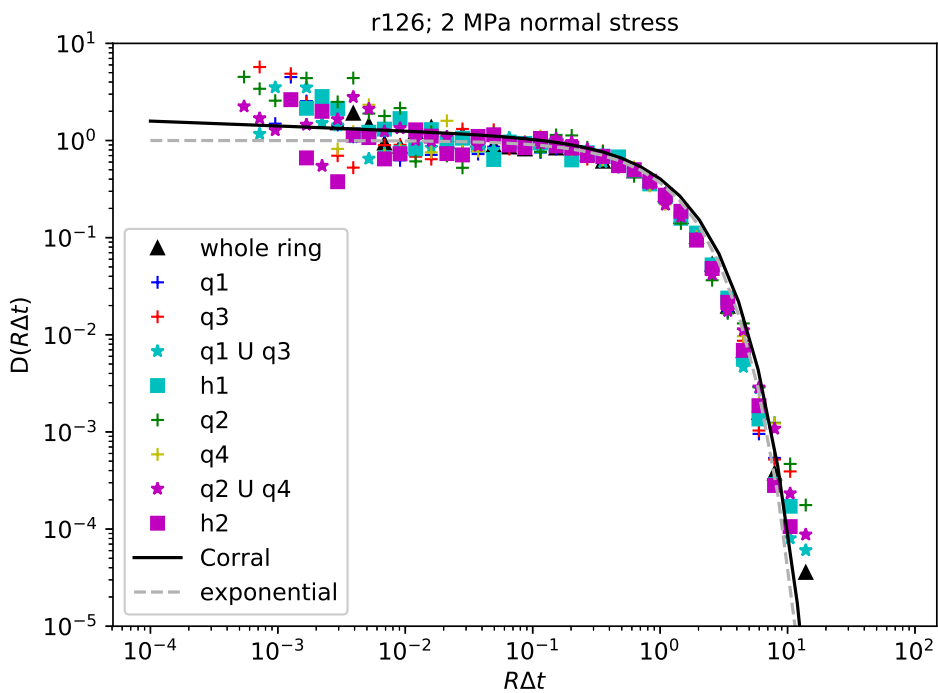


**Figure 3.14:** Normalized probability density plots of various slices of sample r126. h1 and h2: halves. q1, q2, q3, q4: quadrants. The black line is the Corral distribution, with  $(1 - \gamma) = 0.05$ .

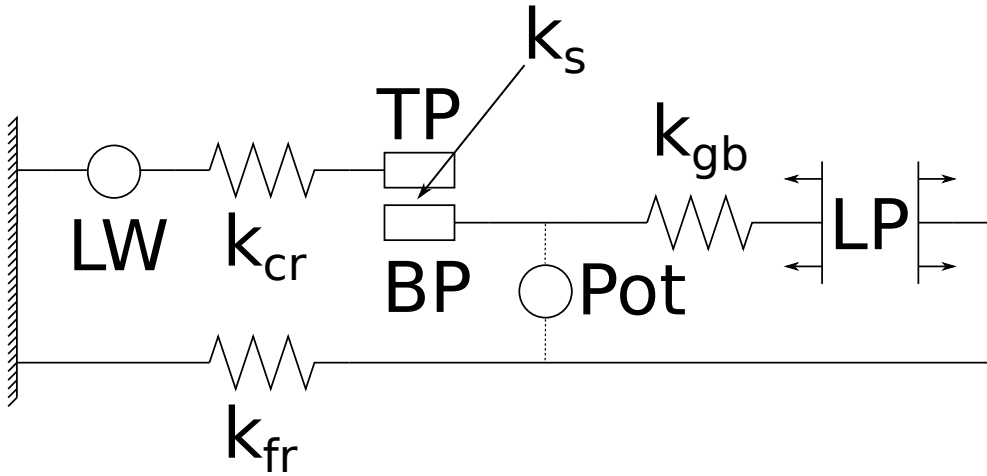
### 3.7.5 Controlling the torsional stiffness of the apparatus

Figure 3.15 shows a simplified analog model of the apparatus, focusing on those elements that are responsible for its torsional stiffness. We replace the torsional system with a linear one to better illustrate its principle of operation and where we intervened to change the stiffness of the apparatus. These elements are: 1. the motor (LP, for load point); 2. the harmonic drive, with spring constant  $K_{gb}$ ; 3. the top and bottom pistons, TP and BP respectively; we assume they have a very high stiffness due to their design; 4. the sample, with spring constant  $K_s$ ; 5. the crosshead with spring constant  $K_{cr}$ ; and 6. the frame with spring constant  $K_{fr}$ . LW represents the instruments (two load washers) used to measure force. These instruments are hosted in two special sockets found in the crosshead at the two points where it jams against the frame due to the rotation imposed by the motor. This allows us to measure the reaction force of the frame at two locations that are equidistant from the axis of rotation and subsequently convert it to torque and shear stress on the sample. In the model we represent the two instruments, which are operating in parallel, with a single “device”. “Pot” is the potentiometer that measures the amount of rotation of the platter that the bottom piston is connected to.

When the sample is loaded at a constant displacement rate, the upper part of the model is under compression, whereas the lower part, i.e. the frame, is under tension. As soon as the sample fails, there is slip between TP and BP, while the harmonic drive and the crosshead unwind a little. The system has been calibrated by using a steel dummy as “sample” and performing several loading-unloading cycles. The stiffness of the apparatus can be reduced by placing sets of Belleville washers between LW and the crosshead. This approach was implemented for the first time by our colleague Martijn van den Ende. When the Belleville springs are not used, they are replaced by steel bolts; this is the default, high stiffness configuration of the apparatus. The effective spring constant of the pair of bolts used in the default, stiff configuration is approximately 1800 kN/mm. The effective spring constant  $k_{eff}$  of a stack of Belleville washers can be approximated using the formula:

$$k_{eff} = \frac{k}{g \frac{1}{n}} \quad (3.6)$$

where  $k$  is the spring constant of a single washer,  $g$  is the number of groups, and  $n$  is the number of washers per group. Stacking washers in the same direction (thus forming a “group”) increases  $k_{eff}$  because they act as springs in parallel, whereas stacking them in opposing directions, acting as springs in series, decreases  $k_{eff}$  and increases the maximum amount of deflection possible. The intermediate stiffness was achieved by replacing the bolts with



**Figure 3.15:** Simplified model of the apparatus that shows the elements responsible for the torsional stiffness of our system. See text for elaboration.

two stacks of Belleville washers, each in a 4x4 configuration (4 groups with 4 washers each). The two stacks in this configuration have an effective spring constant of 3.28 kN/mm. The most compliant setting of the apparatus was achieved with two stacks of washers in 8x2 configurations. The effective spring constant of the two stacks is 0.82 kN/mm. Therefore, the ratio of high to intermediate effective spring constant is approximately 550:1 and the ratio of intermediate to low effective spring constant is 4:1.

## Chapter 4

# Influence of pore water and shear configuration on the mechanical behavior of glass bead aggregates

### 4.1 Abstract

Glass beads have long been employed in laboratory studies related to fault friction and landslides as an idealized analog for soil or fault gouge. Due to the important role of pore fluids in frictional processes in nature, experimentalists often use water in order to investigate the mechanical effects of effective normal stress. Additionally, because of the large displacements involved in faulting and landslides, several studies have employed rotary shear apparatus. Here, we demonstrate that in the presence of water and at effective stresses between 4 MPa and 8 MPa, the mechanical behavior of glass beads at large displacements deviates significantly from the dry case. We report on the results of drained rotary shear experiments with controlled pore water pressure, in which we observed dramatic changes in the frictional stability, as well as more and faster compaction compared to the dry case. Our results show that the presence of water enhances compaction substantially with a concomitant change in frictional behavior. We infer that subcritical crack growth in glass beads accelerates material wear and layer compaction, thus modulating the frictional behavior of the layers. We conclude that future studies that aim to simulate strictly mechanical interactions within sheared glass beads aggregates should consider using pore fluids that are chemically inert with respect to glass, as opposed to water.

## 4.2 Introduction

The frictional strength and stability of granular aggregates sheared to large displacements and in the presence of pressurized pore fluids is of central interest to understanding geohazards such as liquefaction, landslides, and earthquakes. The complexity in terms of mechanical behavior that these phenomena exhibit is due to a large number of parameters such as applied stress, loading rate, temperature but also medium properties such as particle shape and size distribution. Several laboratory studies of granular flow have employed glass beads, due to the simple, spherical shape of the particles, which makes comparison with conceptual and numerical models more effective (Anthony and Marone, 2005; Fulton and Rathbun, 2011; Johnson et al., 2013; Lherminier et al., 2019; Mair et al., 2002; Nasuno et al., 1997). Few laboratory studies have attempted to decouple the mechanical interactions from the chemical effects of the presence of water on the frictional strength and stability of sheared aggregates of glass beads (e.g. Scuderi et al. 2014, 2015).

The mechanical importance of effective normal stress has been acknowledged in soil and rock mechanics since the work of Terzaghi in the first half of the 20th century. The effective stress principle states that:

$$\sigma_{eff} = \sigma_n - \alpha P \quad (4.1)$$

where  $\sigma_{eff}$  is the effective normal stress,  $\sigma_n$  is the total normal stress, and  $P$  is the pore fluid pressure. We assume Biot's coefficient  $\alpha = 1$ . Furthermore, the Mohr-Coulomb failure criterion states that:

$$\tau = c + \mu\sigma_{eff} \quad (4.2)$$

where  $\tau$  is the shear stress,  $\mu$  is the coefficient of friction, and  $c$  is cohesion. From 4.1 and 4.2 it is obvious that pore fluid pressure exerts an important control on the shear strength of sheared granular layers, or geologic faults.

Field investigations of exhumed faults revealed the existence of wear material along the slipping interface of crustal blocks (see Scholz 2002), and therefore provide geophysical context and motivation for a series of studies on the mechanical behavior of sheared granular aggregates. In order to reduce complexity and to focus on the micromechanics of shear, several experimentalists have employed glass beads as an idealized analog material. Sheared layers of glass beads in room temperature conditions are known to exhibit stick slip behavior (Chapter 2; also e.g. Anthony and Marone 2005; Mair et al. 2002).



The presence of water is known to affect the frictional strength of glass bead aggregates. At low normal stress ( $\sim$  kPa), when the aggregate is not fully saturated, water increases strength due to the formation of liquid bridges between particles (Bocquet et al., 1998; Losert et al., 2000). Scuderi et al. (2014, 2015) studied the mechanical and chemical effects of humidity and water on the frictional strength and stability of sheared aggregates of glass beads at increased normal stress (5 to 10 MPa). Increasing humidity resulted in increased “preseismic” (meaning during the “stick” phase) slip and dilation, as well as increased “coseismic” (meaning during the “slip” phase) stress drop. Scanning electron microscope observations revealed that the size of contacts between particles increased with increasing humidity, which they claimed is evidence for the operation of time-dependent chemically assisted processes, such as pressure solution, during the stick phase. Similar results were obtained in the presence of pressurized water. Note that the experiments in these studies were performed using a double-direct shear configuration, with a maximum displacement of approximately 20 to 30 mm.

The mechanical effects of pressurized pore fluids have also been investigated numerically using coupled computational fluid dynamics and discrete element method simulations (Dorostkar et al., 2017a,b). Comparisons between dry and wet runs show that in the presence of fluid, “coseismic” friction (stress) drop and compaction increase, due to momentum exchange between the particles and the fluid. These authors also report increased recurrence intervals between stress drops, compared to the dry case.

The effect of chemically assisted processes can be made more obvious by using a combination of a soluble granular medium and a pore fluid with faster chemical kinetics at room temperature. Bos et al. (2000) found that granular halite layers transitioned from stick-slip to stable sliding and compacted more, as a function of increasing water content in the pore fluid (mixtures of methanol and water). Dry and silicone oil saturated samples exhibited stick-slip behavior. The results of the experiments by Bos and colleagues show that porosity changes due to compaction enhanced by pressure solution can alter the frictional behavior of sheared granular halite dramatically. This finding highlights the effect of material solubility and pressure solution kinetics (in the case of halite) on the mechanical behavior of the gouge.

Another application of friction experiments on layers of glass beads is in the context of complex systems. It has been argued that sheared granular aggregates exhibit aspects of self-organized criticality, as do earthquakes (Dalton and Corcoran, 2001; Kanamori and Brodsky, 2004; Shcherbakov et al., 2015). In Chapters 2 and 3, the goal was to reconcile the existing

body of work on the micromechanics of granular shear with the statistical descriptions of the macroscopic behavior of the system (e.g. scaling of AE amplitudes, stress drop magnitudes, and interevent times). For this, we want to minimize the number of unknown parameters in order to establish the “baseline” behavior and subsequently track complexity in the macroscopic behavior as the amount of controlled parameters is increased, or as existing parameters are manipulated. From this point of view, performing experiments on fully saturated samples eliminates humidity as a variable.

Here we demonstrate the complex mechanical behavior that aggregates of soda-lime glass beads exhibit during prolonged shearing in the presence of water, for comparison with their dry counterparts (Chapter 2, 3). The mechanical and acoustic emission (AE) data from three rotary shear experiments on layers of glass beads saturated with pressurized water show significant variations in frictional strength and stability, as well as larger and faster compaction. We infer that the observed complexity is due to chemically assisted sub-critical crack growth that enhances mechanical wear dramatically and changes the particle size distribution and the porosity of the sample. This suggests that water is probably not the ideal pore fluid when one aims to study the mechanical aspects of the interaction between a sheared glass beads aggregates and a pressurized pore fluid.

### 4.3 Methods

We performed rotary shear experiments on thin layers of soda-lime glass beads, using the sample material, methods, and the apparatus described in Chapter 2. The list of experiments is shown in Table 4.1.

We followed the sample preparation procedure described in Chapter 2 to prepare our samples. A fixed quantity of glass beads, equal to 30.20 g, was used each time. Each sample layer was approximately 4.4 mm thick at the beginning of the experiment. For the tests described here, one of the diametrically opposed fluid ports of the outer confining ring was capped, while the other port was connected to a Teledyne 65D ISCO pump via a small diameter steel tube. First, the target total normal stress was applied. Low vacuum was applied to

**Table 4.1:** *Table of experiments.  $\rho_b$  stands for bulk density.*

Experiment ID	$\sigma_n$ (MPa)	$P$ (MPa)	$\sigma_{eff}$ (MPa)	Starting $\rho_b$ ( $g/cm^3$ )
r089	8	4	4	1.72
r091	10	4	6	1.69
r090	10	2	8	1.71

the sample chamber to evacuate the air and subsequently de-ionized water was introduced as pore fluid and kept pressurized at the target value by the pump. Approximately 5.3 mL of water would have been required to fully saturate a sample with starting packing ratio of 0.7 and initial thickness of 4.4 mm. The sample was then sheared by rotating the bottom piston at 0.02 °/s (equivalent to  $\sim 15 \mu\text{m/s}$  at the mean radius of the sample, i.e. 42.5 mm). There was no sample extrusion. For r089 and r091, after the end of shearing the shear stress was removed via a brief counter-rotation of the bottom ring for approximately  $1^\circ$ , the pore fluid was depressurized, and then the actuator was retracted to remove the normal stress. For r090, the pore fluid was depressurized in steps and the sample was sheared for a few more degrees, for reasons unrelated to the scope of this chapter. No water leaks were observed during r089 and r090. Traces of water were found onto the rotating stage during disassembly of r091. Since the water volume in the pump reservoir did not change significantly, we consider that leak insignificant.

The quantities monitored were the same as in Chapter 2, with the addition of pore fluid pressure. Here we focus on apparent friction, actuator position, pore fluid pressure, and acoustic emission (AE) amplitude. We define apparent friction, henceforth simply friction,  $\mu$  as the ratio of shear to effective normal stress  $\sigma_{eff}$ :

$$\mu = \frac{\tau}{\sigma_n - P} \quad (4.3)$$

where  $\tau$  is the shear stress,  $\sigma_n$  the total normal stress, and  $P$  the pore fluid pressure. Glass beads of the size used in this study ( $\sim 0.5$  mm) show no cohesion as aggregates, therefore  $c = 0$  in equation (4.2). Because both of the parameters in the denominator are servo-controlled,  $\mu$  is proportional to  $\tau$ . The representative size of an AE event is the squared median of the maximum amplitude recorded in each of the 16 AE transducers that were used in the experiments.

## 4.4 Results

The three samples showed complex mechanical behavior (Figure 4.1). Each sample transitioned from a stick-slip phase to strain hardening with decreasing stress drops, followed by substantial weakening and a brief reappearance of stick-slip. Further shearing resulted in significant strain-weakening and hardening episodes, accompanied by relatively small stress drops. The major weakening phase occurred at different displacement in each experiment (r089:  $\sim 123^\circ$  or 91 mm; r091:  $\sim 42^\circ$  or 31 mm; r090:  $\sim 17^\circ$  or 12.5 mm) and coincided with a period of relatively fast dilation.

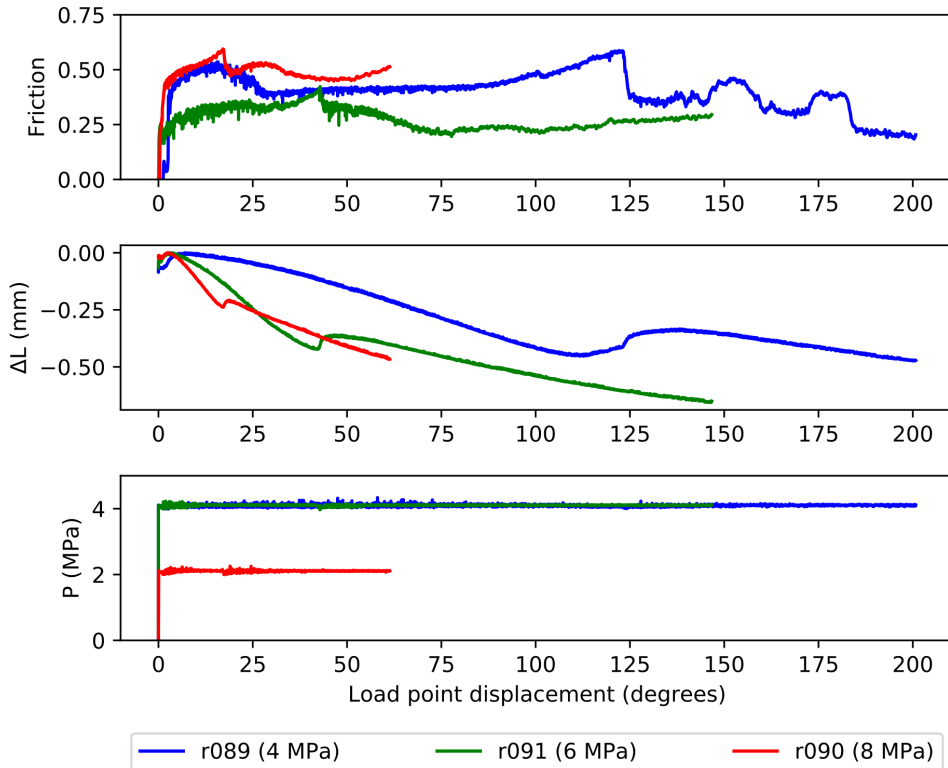


**Figure 4.1:** Friction, actuator displacement ( $\Delta L$ ), and pore fluid pressure ( $P$ ) versus displacement. Negative  $\Delta L$  corresponds to shortening (compaction). The stress values in the legend indicate the value of effective normal stress. The unloading procedure is not shown.

The long-term compaction rate appears to have decreased after the dilative episode.

There is a strong correlation between individual stress drops and spikes in pore fluid pressure during pronounced stick-slip, as can be seen in Figure 4.2. As the magnitude of stress drops decreases, so does the magnitude of excursions of the pore fluid pressure. Due to the insufficient resolution of the position of the actuator, it is not clear whether a similar correlation exists between stress drop, pore fluid pressure, and changes in sample thickness.

Similar to what has been shown in Chapter 2, acoustic emission amplitudes were, on average, proportional to stress drops. The evolution of peak stress drop values as a function of displacement was reflected in the size of acoustic emissions, particularly for the experiments at  $\sigma_{eff} = 6$  MPa (r091) and  $\sigma_{eff} =$

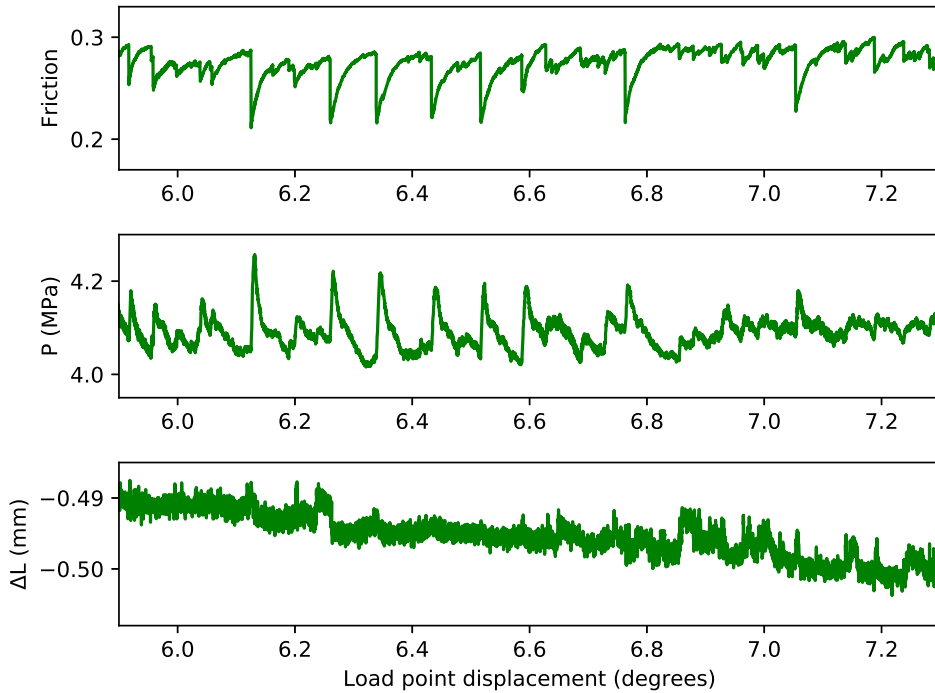


**Figure 4.2:** Data excerpt from experiment r091 ( $\sigma_{eff} = 6$  MPa). Stress drops (top panel) are associated with rapid increases in pore fluid pressure (bottom panel). The sample was compacting, as evidenced by the change in the actuator position (middle panel), but transient changes are difficult to resolve due to the noise level.

8 MPa (r090), as shown in Figure 4.3.

The sample material from the experiments was recovered in good condition. Post-mortem visual examination of sample r089 ( $\sigma_{eff} = 4$  MPa) revealed a slurry containing larger beads mixed with finer particles. Visual examination of r090 ( $\sigma_{eff} = 8$  MPa; Figure 4.4 A) and r091 ( $\sigma_{eff} = 6$  MPa) revealed the presence of a relatively cohesive boundary layer on the bottom piston (the bottom piston is connected to the motor during the experiment), overlain by a thicker layer of glass beads and water slurry. We were able to sample parts of the cohesive layer as well as of the bulk material above it individually, and we submitted them to a post-mortem particle size analysis (Figure 4.5). The analysis revealed that the abundance of fines was higher in the boundary layer compared to the bulk. Note that fine particles, albeit with more limited size distribution, were generated in the dry experiments as well, as shown in

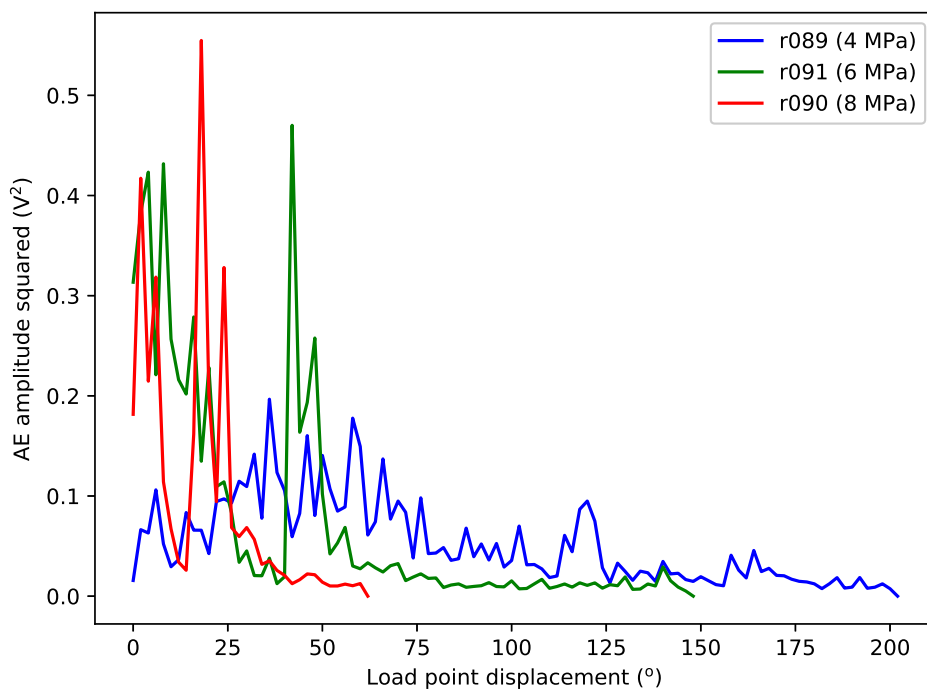


**Figure 4.3:** Evolution of peak AE sizes (squared median amplitude) as a function of load point displacement. Note that the peak sizes seen in r089 (blue) are clearly smaller than those seen in r091 (green) and r090 (red). In all three cases, an increase in peak sizes can be seen at approximately the same displacement as the major weakening event seen in Figure 4.1

Chapter 2. Scanning electron microscope (SEM) images of the boundary layer from r090, taken approximately one year after the experiment, during which time the water evaporated and the sample became cohesive, show that the larger beads were “floating” in a fine grain matrix (Figure 4.4 B). Beads from the bulk have varying amounts of damage, if any. All of them are partially coated by fines. Some beads have chipped surfaces. Upon closer examination of these surfaces we found evidence of plumose cracking (Figure 4.4 C, D).

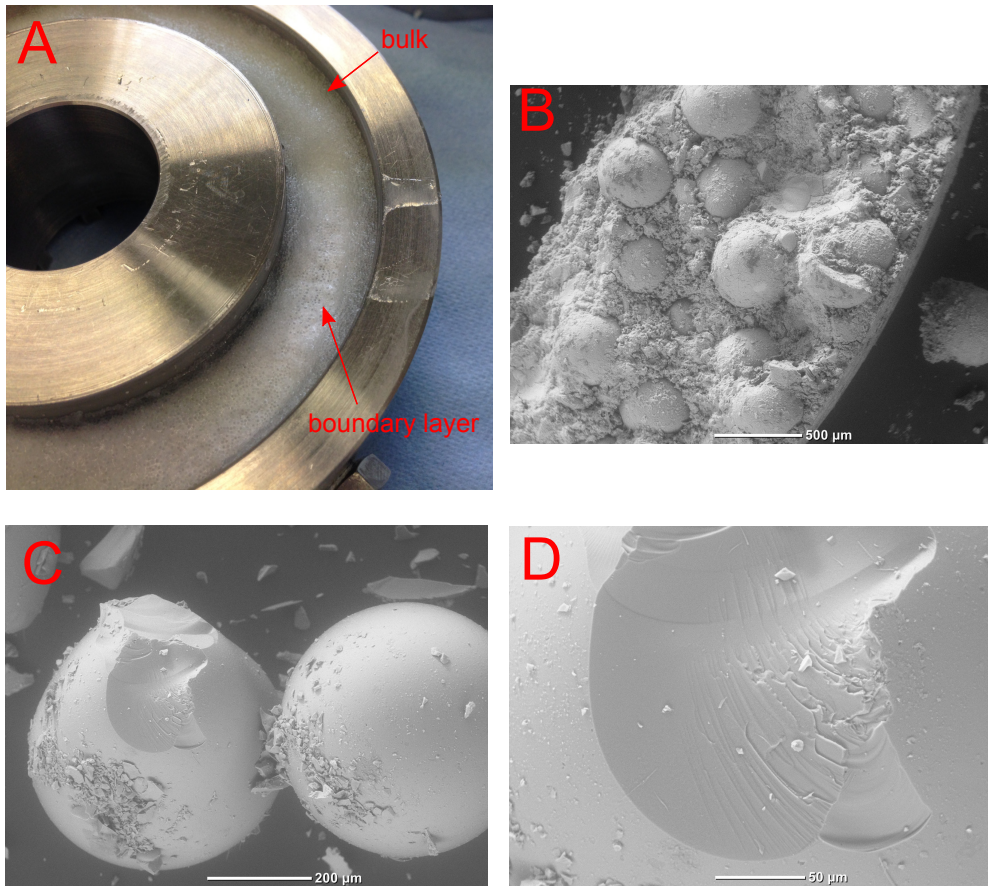


**Figure 4.4:** A: Post-mortem view of sample r090 with the top piston removed. A "bulk" layer of glass beads can be seen resting on top of a cohesive boundary layer abutting the bottom piston. Visual examination revealed that the boundary layer consisted of isolated large glass beads stuck in a fine grain matrix (white). The inner radius of the sample was 35 mm and the outer radius was 50 mm. B: SEM photomicrograph of the boundary layer material. C: glass beads from the bulk layer. D: detail of a mixed-mode plumose crack or conchoidal fracture on the left particle shown in C.

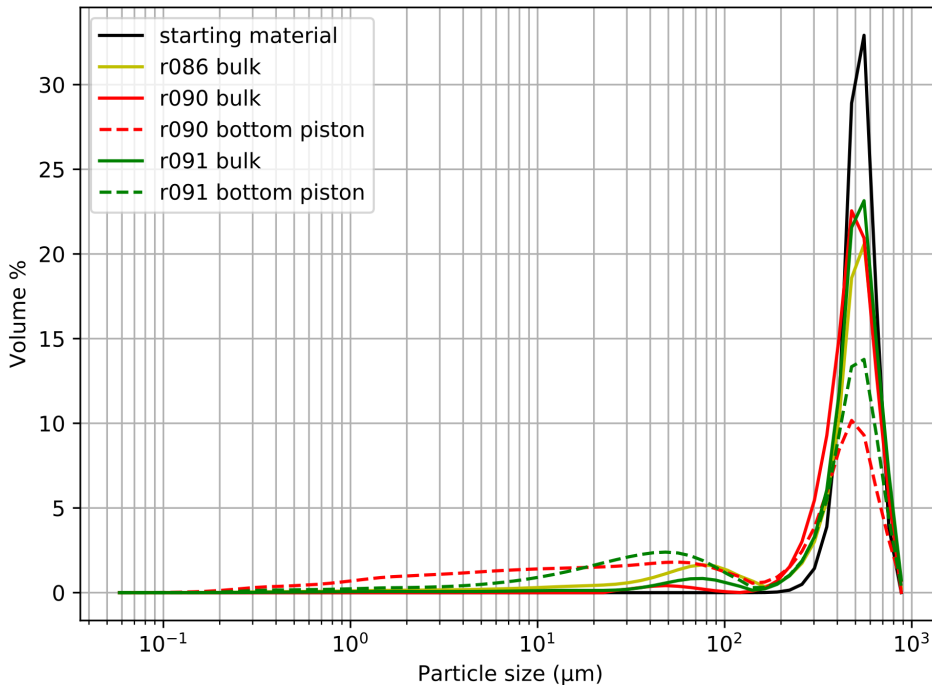


**Figure 4.5:** Post-mortem particle size analysis of parts of the r090 and r091 samples. The particle size analyses of the starting material and the post-mortem analysis from a dry experiment (r086) are shown for comparison. Note the different size distribution of the wear particles generated under different effective normal stress values and dry versus wet conditions.

## 4.5 Discussion

The aim of this chapter is to examine the effect of water on the mechanical behavior of aggregates of glass beads under shear. Our data show that water can drastically alter the mechanical behavior of sheared glass bead aggregates by enhancing particle wear and the production of fines. This has important implications for studies that use glass beads as an analog material, as discussed at the end of this section. In this chapter we have reported two key observations: 1. evolution of frictional strength and stability, sample volume, and peak AE size (squared amplitude) as a function of displacement (Figure 4.1 and Figure 4.3); and 2. evolution of the particle size distribution during the experiments (Figure 4.5).

In Chapter 2, we attributed the repetitive stick-slip behavior of the samples



to the formation and failure of force chains within the granular layers, in agreement with the findings of similar studies (e.g. Anthony and Marone 2005; Jiang et al. 2017; Mair et al. 2002). We observed the generation of fine particles as the byproduct of frictional wear between the glass beads, presumably as a function of shear displacement. Despite numerical (Abe and Mair, 2009; Morgan and Boettcher, 1999) and experimental (Anthony and Marone, 2005; Mair et al., 2002) evidence that suggests that a wider particle size distribution promotes stable sliding (by increasing the number of particles participating in force chains) and that the generation of angular particles strengthens the sample, in most of the experiments discussed in Chapter 2 the frictional behavior remained largely constant, i.e. the AE distributions (used as proxies for stress drop distributions) remained constant throughout the experiments. This suggests that the amount of fines that was produced did not affect the operation of force chains significantly, i.e. the fines did not participate in the load-bearing framework of the aggregates. The experiments discussed in Chapter 2 were performed at an effective normal stress of 8 MPa, well below the 25 MPa threshold of pervasive particle fracturing (Mair et al., 2002).

The mechanical data in Figure 4.1 show an evolution which was absent from the experiments discussed in Chapter 2. This suggests that the presence of pressurized pore water altered the volumetric and therefore the frictional behavior of the glass bead aggregates. We quantify the difference between dry and wet experiments by focusing on two consistent features: 1. the relative amount of compaction between a dry and a wet experiment at similar effective normal stress, and 2. the amount of displacement required until the critical point (CP) where frictional weakening and layer dilation occurred.

Figure 4.1 shows that the rate of displacement of the axial (normal) actuator prior to the CP was positively correlated with increasing effective normal stress. In other words, the sample under the highest effective normal stress compacted faster than the sample under the lowest normal stress. Figure 4.6 shows the relative amount of compaction for experiments r086 (dry; Chapter 2) and r090 (wet) at the same effective normal stress (8 MPa) and load point velocity ( $0.02^\circ/\text{s}$  or approximately  $15 \mu\text{m}/\text{s}$ ). Layer thickness  $h$  has been normalized to the layer thickness  $h_o$  just prior to the start of shearing at  $t = 0$  s. For r086  $h_o = 4.14$  mm, and for r090  $h_o = 4.28$  mm; these values include the pre-compaction. During the initial  $\sim 210$ s (equivalent to  $4.2^\circ$  or  $3.1$  mm) the volumetric behavior of the two samples was comparable. However, beyond the initial 210s of shearing, the wet sample compacted much more than the dry one. The equivalent average strain rates from the data shown in Figure 4.6 are  $6 \times 10^{-6} \text{ s}^{-1}$  for the dry

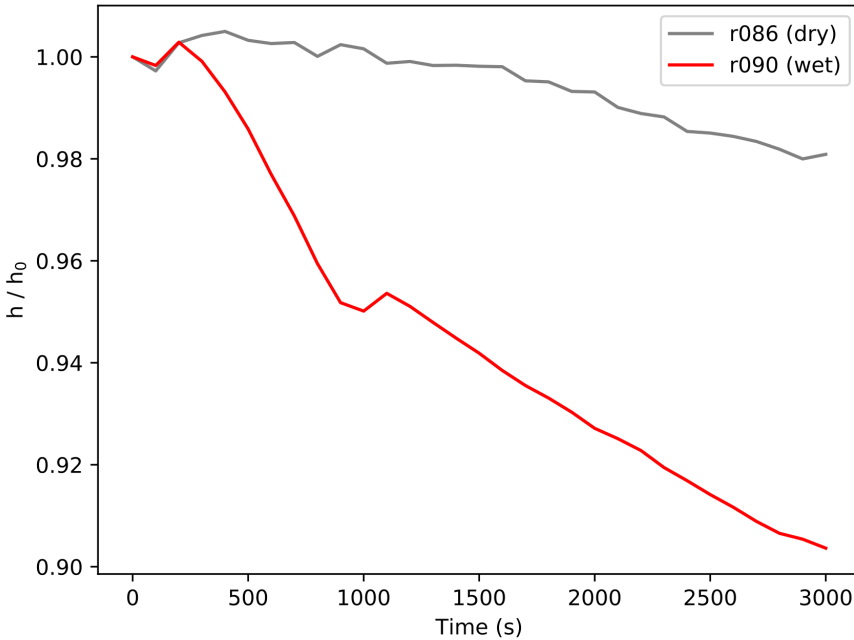


**Figure 4.6:** Relative sample compaction over the initial 3000 seconds of shearing ( $60^\circ$  or approximately 44 mm) for experiments r086 ( $\sigma_{eff} = 8$  MPa, dry; see Chapter 2) and r090 ( $\sigma_{eff} = 8$  MPa, wet). Both samples had a starting bulk density of approximately  $1.71$  g/cm<sup>3</sup> and were sheared at  $0.02$  °/s.

and  $3 \times 10^{-5} \text{ s}^{-1}$  for the wet experiment; a factor of 5.

Our data suggest that the enhanced layer compaction in the presence of pressurized pore water was the result of physico-chemical processes that increased the incidence of conchoidal fracture/pitting of contacts and associated particle comminution (production of fines). On the basis of measurements of preseismic layer dilation, waiting time between slip events, and microstructural evidence, Scuderi et al. (2014, 2015) inferred that a time-dependent physico-chemical process similar to pressure solution was responsible for increasing the contact area between particles during the quasi-stationary “stick” phase. However, Rossi et al. (2007) reported that the rate of pressure solution measured over the course of two weeks in water saturated glass beads at a temperature of  $150^\circ$  was practically negligible. Thus we conclude that pressure solution does not explain the rate of

compaction we observed in our tests. However, it is likely that particle contact fracturing/spalling (conchoidal fracture) and particle wear was enhanced by water via sub-critical crack growth along the contacts of load-bearing particles. Soda-lime glass is susceptible to environment assisted cracking, due to stress corrosion (François et al., 2013; Ronchetti et al., 2013; Wiederhorn, 1967; Wiederhorn et al., 1982; Wiederhorn and Bolz, 1970). Figure 4.4 (C, D) shows evidence of mixed-mode cracking, which is known to occur in soda-lime glass under conditions favoring sub-critical crack growth (e.g. Ritter et al. 2000). As mentioned earlier, the production of a substantial number of finer particles is expected to cause a gradual reduction of stick slip magnitude and strain hardening behavior, because the produced fines would reduce the brittleness of force chains. This is exactly what our mechanical (Figure 4.1) and AE size data (Figure 4.3) suggest.

The second consistent feature of our experiments was the weakening/dilatant event, as a function of shear displacement and effective normal stress, that was accompanied by the reappearance of large stress drops. Figure 4.7 shows the amount of load point displacement achieved until the start of the weakening/dilatant event seen in the wet experiments. The monotonically decreasing relationship between the two quantities, suggests that the samples' microstructure had to reach a critical configuration for such a transition to occur. Because of this relationship, we infer that responsible for the transition were the particle wear rate, which should be proportional (but not necessarily linearly related) to the effective normal stress, and some inherent characteristics of the rotary shear configuration that we will discuss below. Scuderi et al. (2015) did not report a similar critical point in their experiments under  $\sigma_{eff} = 10$  MPa, even though Figure 4.7 suggests that such a transition should be observable within the amount of displacement that can be achieved by their double-direct shear (DDS) configuration. There are three important differences between the experiments by Scuderi et al. (2015) and ours. First, Scuderi and colleagues used glass beads of smaller initial particle size (approximately  $125 \mu\text{m}$  versus  $550 \mu\text{m}$ ) and distribution, which may have had an influence on the wear rate, as larger particles may be more likely to sustain fractures compared to smaller ones. Second, the DDS pistons confine the sample horizontally, whereas the rotary shear pistons confine the sample vertically. If gravitational forces were important, any wear material produced would have eventually settled onto the bottom, rotating piston. The coalescence of fines at large quantities (larger than in the dry case; Chapter 2) along the rotating boundary would likely alter the frictional behavior of the sample. A boundary layer stronger than the bulk would likely act as an

extension of the steel piston, whereas a boundary layer weaker than the bulk should lead to strain localization and macroscopic frictional weakening. Post-mortem particle size analysis of the boundary layers confirmed the presence of significant amount of fines compared to the bulk (Figure 4.5) and post-mortem SEM photomicrographs of wet (Figure 4.4) as well as dry samples (Chapter 2) show wear material attached to larger beads. Note that the latter observation may be influenced by how the samples were salvaged (i.e. via scooping material and placing it into containers for preservation until particle size and microstructural analyses could be performed). In the DDS configuration, any wear material settling under the influence of gravity would not necessarily settle along the moving piston. Furthermore, as the moving piston slides downward, the exact area of contact with the sample is renewed. By contrast, the rotary shear boundary resembles the periodic boundary condition frequently used in DEM simulations (Morgan and Boettcher, 1999). Third, the DDS piston surfaces contain porous elements and the sides of the sample layers are exposed to the “ambient” pressure inside the rubber jacket. In our configuration the piston surfaces are impermeable and there is only one fluid port, located along the outer confining ring (the second fluid port was closed).

We posit that the existence of the critical point in our experiments is primarily due to the different properties (namely its periodicity and position relative to the sample) of the moving boundary between the rotary shear and the DDS configurations. Upon applying a load point velocity, the initial mechanical response of the layers must have been the result of force chain collapse and formation, resulting in stick-slip behavior. However, due to the increased (compared to the dry case) wear and compaction rate due to the presence of water, the initially narrow particle size distribution gradually became wider, stabilizing the force chains and reducing the magnitude of stress drops. Meanwhile, the increased abundance of angular fragments lead to macroscopic hardening. The critical point might have been reached when a sufficient amount of wear material had been generated and allowed to coalesce along the rotating boundary, perhaps covering it completely and acting as the effective new piston surface. Upon such an event, deformation would have to be accommodated by the rest of the glass beads (“bulk”) again, which could explain the dilation and the temporary reappearance of large stress drops. Eventually more water-enhanced wear due to sub-critical crack growth in the particles may have been responsible for the subsequent suppression of large stress drops by increasing the number of load-bearing particles in the sample. Throughout shearing it is possible that silica amorphization, if present, would alter the frictional strength of particle contacts (Nakamura et al., 2012).

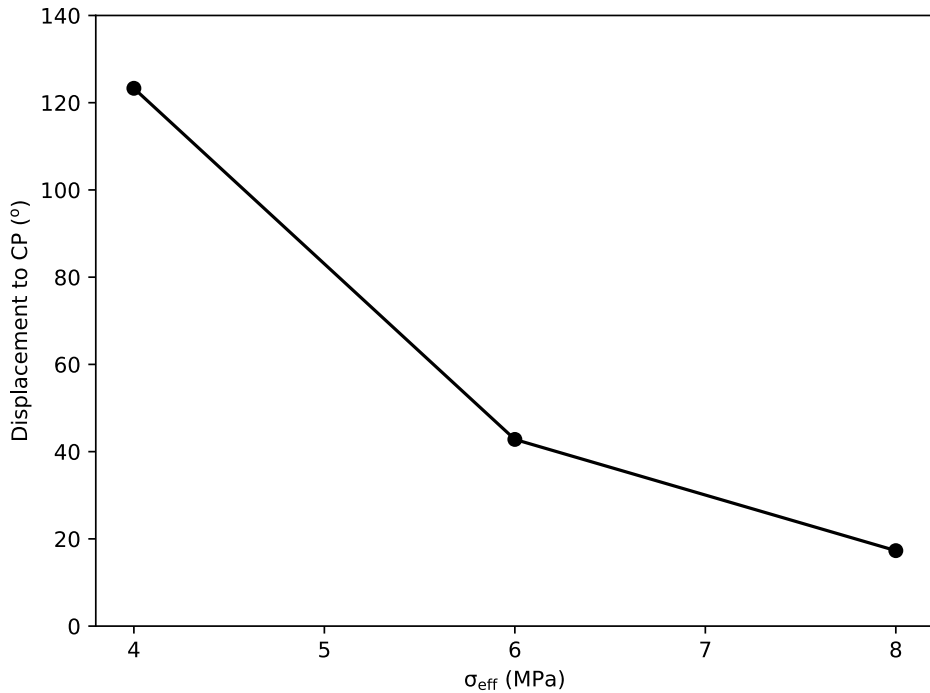


**Figure 4.7:** Amount of load point displacement (in degrees; multiply by 0.74 for mm) required to reach the critical point (CP), as a function of effective normal stress ( $\sigma_{\text{eff}}$ ).

The discussion above does not compare the absolute strength of the wet and dry samples, nor the magnitude of stress drops and peak AE sizes. We have avoided comparing the strength of wet and dry samples due to the uncertainty in absolute values of shear stress (Chapter 2). Tighter constraints on the absolute values of shear strength would likely provide further insight on the role of water in the frictional interactions between particles. Another observation is that the peak AE amplitudes recorded in the water saturated samples were smaller than in the dry case (Chapter 2). As AE amplitudes and stress drop magnitudes were roughly proportional (Chapter 2), this suggests that the maximum value of stress drop became smaller in the presence of water. From our data it is difficult to discern whether this is due to source or path effects. An investigation of the effect of water on the attenuation of elastic waves in our apparatus would help us understand whether the difference in peak AE amplitudes is due to wave propagation effects, or whether it reflects a change in the source of elastic waves (i.e. the frictional interaction between

particles). Accounting for path contributions is necessary to compare our findings with those of Scuderi et al. (2014, 2015) and Dorostkar et al. (2017a,b).

## 4.6 Conclusion

The systematic transitions in the mechanical behavior and peak AE amplitudes that we observe between the three experiments presented here, as well as the dramatic contrast with the data presented in Chapter 2, suggest that the presence of water greatly enhances the compaction of glass bead aggregates undergoing shear, thereby affecting their frictional behavior. To constrain the nature of these effects further, we propose that future experiments should instead employ a pore fluid that is chemically inert with respect to soda-lime glass, or that has greatly reduced reaction kinetics, to suppress chemically assisted processes as much as possible. Ideally, it should have similar wetting behavior and compressibility as water. Potential candidates are silicone oil, decane, or an inert gas like dry argon (e.g. Brzesowsky et al. 2014b,a; Hangx and Brantut 2019; Zhang and Spiers 2005). The use of such a fluid should allow us to assess the ratio between mechanical and chemically assisted particle interactions and perhaps constrain the nature of the exact mechanisms. If the mechanical behavior and acoustic signature of the samples saturated with “chemically inert” fluids is indeed similar to the dry ones (Chapter 2), we could 1. eliminate humidity as a variable, and 2. investigate the potential influence of effective stress on the scaling of AE amplitudes and interevent times. This would greatly benefit our efforts to establish a microphysical basis for the statistics of avalanches in sheared granular media. Our results also suggest that differences between experimental configurations may lead to drastically different evolution of the sample’s mechanical behavior.

## Acknowledgements

We would like to thank Thony van der Gon Netscher for preparing the necessary adapters and tubing required for circulating and pressurizing pore fluids in the apparatus.

## Chapter 5

# A laboratory perspective on the Gutenberg-Richter and Characteristic Earthquake models

### 5.1 Abstract

After several high profile failures of probabilistic seismic hazard analysis (PSHA) maps in recent years, some of the basic concepts of PSHA have become the subject of criticism. Central to this discussion is the debate on the validity of the characteristic earthquake (CE) versus the Gutenberg-Richter (G-R) model. These models rely on limited instrumental and paleoseismological data, that do not lend themselves to robust statistical testing. Here we demonstrate how a friction experiment on aggregates of glass beads can be tuned to produce either characteristic or truncated power law distributed avalanches. Central to the idea of using a laboratory experiment is the generation of large catalogs of events to overcome the main limitation that confronts observational seismology, namely data scarcity. The use of a rotary shear apparatus allows us to achieve large displacements and thus generate large numbers of acoustic emissions related to unstable slip events. Long-term probability density distributions of size and recurrence time of acoustic emission activity were found to be sensitive to the particle size distribution and the applied normal stress, and, to a lesser degree, the stiffness of the loading apparatus. In addition, the distributions based on long-term data were found to be insensitive to the fact that samples experienced mode switching between regular and irregular stick-slip. Our

work shows that CE and truncated power law behavior can be the result of different medium properties and boundary conditions, but also a matter of observation period. In the context of PSHA, our results imply that determining whether a fault follows the CE or G-R model may not be possible, because the conditions that produce either model can change dynamically.

## 5.2 Introduction

Probabilistic seismic hazard analysis (or assessment; PSHA) is currently the standard method used in the design phase of new infrastructure or the retrofit of existing ones. Some concepts used in seismic hazard analysis, i.e. characteristic earthquakes, and seismic gaps, have come under increased scrutiny in recent years after several high profile cases of unexpected earthquakes, in terms of location and/or magnitude, with the prime example being the 2011  $M_w$  9.1 Tohoku earthquake in Japan (Geller et al., 2015; Mulargia et al., 2017; Stein et al., 2012; Stein and Friedrich, 2014). The disparity between the magnitude and epicenter of several destructive earthquakes and the expectations based on seismic hazard maps may have been due to chance, i.e. aleatory variability, in which case the aforementioned earthquakes were “black swans”, or due to epistemic uncertainty, i.e. the result of poor understanding of the physical processes that lead to seismicity (Stein et al., 2011).

One type of epistemic uncertainty is the focus of the debate between the Characteristic Earthquake and the modified Gutenberg-Richter (G-R) model regarding the frequency-magnitude distribution (FMD) of earthquakes. Seismologists face the problem of having to identify the real FMD using empirical FMDs that are based on data collected since the dawn of instrumental seismology, approximately 100 years ago, and supplemented by paleoseismological studies (Kagan, 1996; Wesnousky, 1994). Using an incorrect FMD in seismic hazard analysis could easily lead to under- or over-estimation of the maximum expected magnitude and the rate of large earthquakes, as we will see below.

According to the modified G-R model, the logarithm of the cumulative number of earthquakes above a certain magnitude is a linear function of magnitude with a slope of approximately -1 (Kanamori and Brodsky, 2004). In practice the probability density of seismic moment can be described by a gamma distribution, i.e. a power law with an exponential right tail (Kagan, 1994; Main, 1996; Sornette and Sornette, 1999). The G-R model is well supported by data on global and regional seismicity, but its universality is



disputed by some authors, who posit that large earthquakes on individual faults and plate boundary segments occur quasi-periodically and/or with a small range of magnitudes (Schwartz and Coppersmith, 1984; Wesnousky, 1994). The concepts of characteristic earthquakes and of seismic gaps are intimately linked. Seismic gaps are a corollary of plate tectonics and elastic rebound: if most of the slip along plate boundaries occurs seismically, then earthquakes are likely to occur in regions where there is slip deficit. Furthermore, assuming constant plate motion, i.e. a constant loading rate on the “locked” boundaries, seismic slip should occur quasi-periodically and with “fixed” magnitude so as to cover the slip deficit in that particular “gap” or segment of the plate boundary, followed by a “reloading” period and another characteristic earthquake, to form what is known as the seismic cycle.

The concepts of characteristic earthquakes and seismic gaps have been applied to various hotspots of natural seismicity, both terrestrial and offshore. A classic application has been the North Anatolian Fault in Turkey (Barka, 1996; Toksöz et al., 1979). Seismicity on Gofar, a mid-ocean ridge transform fault in the East Pacific Rise, has been interpreted as an example of seismic cycles. This motivated the timely deployment of ocean bottom seismometers to capture a 2008  $M_w$  6.0 earthquake along with its foreshocks and aftershocks (Boettcher and McGuire, 2009; McGuire, 2008; McGuire et al., 2012; Wolfson-Schwehr et al., 2014). A similar attempt in Parkfield, California, where earthquakes had been occurring every approximately 20 years since the mid 20th century, was unsuccessful (Bakun and Lindh, 1985; Kagan et al., 2012; Savage, 1993). Nevertheless, the characteristic earthquake model appears to be a key ingredient of modern rupture forecasts for California (Field et al., 2017; Parsons et al., 2018) and has been used to calculate earthquake probabilities in Japan (Parsons et al., 2012). The idea of quasi-periodic earthquakes of a characteristic magnitude understandably has gained traction with seismic hazard analysis because it puts constraints on “where”, “when”, and “how big” for large earthquakes. However, the characteristic earthquake model has been found to perform poorly in comparison to the G-R model (and even random chance) when submitted to statistical testing, and the forecasts based on it have been criticized for being largely untestable (Kagan, 1993; Kagan and Jackson, 1991b, 1995, 1999; Parsons and Geist, 2009; Rong et al., 2003). Also, the 2011  $M_w$  9.1 Tohoku and 2016  $M_w$  7.8 Kaikoura earthquakes challenge a crucial assumption of seismic gaps and characteristic earthquakes, i.e. that only one fault or plate boundary segment can rupture in an earthquake (Furlong and Herman, 2017; Kagan and Jackson, 2013; Lamb et al., 2018; Shi et al., 2017). Considering

the long recurrence time of large earthquakes, often in the hundreds of years, the length of the instrumental record of earthquakes (approximately 100 years) and the limitations of paleoseismological research (Weldon et al., 2004), it is not clear whether characteristic earthquakes and seismic gaps are actual features or an artifact of limited observations. The problem is worse for intraplate regions, where the time between large earthquakes is longer than at plate boundaries (Stein et al., 2012). For example, synthetic tests using randomly generated earthquakes along the eastern coast of Canada or the North Africa plate margin have shown that a limited window of observation (order of  $10^3$  years) can lead to the false impression of seismic gaps and characteristic earthquakes (Swafford and Stein, 2007).

The epistemic uncertainty regarding earthquake physics and the problem of data sparsity have motivated theoretical and laboratory studies that aim to simulate the complex behavior seen in natural seismicity as an emergent feature of the interaction of many simple constituents (Shcherbakov et al., 2015). Characteristic events or G-R type behavior can be reproduced by Burridge-Knopoff type spring-block models (Brown et al., 1991; Carlson and Langer, 1989), cellular automata and rupture mechanics models (Ben-Zion and Rice, 1993, 1995; Dahmen et al., 1998; Klein et al., 2017), discrete element method simulations (van den Ende et al., 2018; Ferdowsi et al., 2013), and laboratory experiments (Baró et al., 2013; Dalton and Corcoran, 2001, 2002; Hamilton and McCloskey, 1997; Johnson et al., 2013). In Chapter 2 of this thesis we reported G-R type statistics of stress drop and AE amplitudes from large displacement rotary shear experiments on thin layers of glass beads. Large displacements imply that the experiments generate large numbers ( $\sim 10^4$ ) of acoustic emission (AE) events, that are related to instances of unstable slip (also known as granular avalanches). Unlike catalogs of natural earthquakes, that are relatively short compared to the recurrence intervals of large earthquakes in many regions, catalogs generated via our laboratory experiments can be evaluated for reproducibility and thus for how complete they are in terms of rare, large events. Here we show that by tuning certain parameters of the experiments, namely the particle size distribution and the normal stress, we were able to produce characteristic event (CE) behavior, rather than the Gutenberg-Richter type distributions shown in Chapter 2.

### 5.3 Methods

We generated laboratory quake catalogs by shearing thin layers of glass beads in a rotary shear configuration at room temperature and relative

humidity, using the apparatus and methods described in Chapter 2. The sample material consisted of two batches of soda-lime glass beads with size ranges of 150 to 212  $\mu\text{m}$  and 400 to 500  $\mu\text{m}$  respectively (the second batch was also used for the experiments in Chapters 2, 3 and 4). For convenience, we will refer to samples using the former size range as type A, and those using the latter size range as type B.

We followed the experimental procedure described in Chapter 2, to shear thin layers (approximately 4.5 mm thick) of glass beads at 0.02  $^\circ/\text{s}$  (equivalent to approximately 15  $\mu\text{m}/\text{s}$  at 42.5 mm distance from the center of rotation) and a constant normal stress (4 or 8 MPa) for more than 180 $^\circ$ . The starting experimental parameters of each experiment, ten in total, are shown in Table 5.1. Apart from using two different particle size distributions and normal stresses, as mentioned above, we also performed experiments at two different machine stiffness configuration. We lowered the torsional stiffness of the machine by replacing certain steel elements with a combination of Belleville washers (see section 3.7.5). Decreasing the torsional stiffness of the apparatus allows it to store more elastic energy at a given torque compared to its stiff configuration. During a frictional instability, part of the stored energy is released in the form of elastic waves and heat, while some small amount is also consumed by processes that cause mechanical wear on the glass particles.

The data acquisition parameters were kept constant throughout the experimental campaign. To evaluate the real detection threshold of acoustic emission events we increased the sensitivity of the recording system for experiment r080 (also see section 5.7). The increase in sensitivity was achieved by using a hysteresis value of 0.2 V instead of the standard 0.4 V for the rising and falling edge trigger used in the AE channels. In this chapter we focus on the recorded time series of shear and normal stress, as well as on the size, source location, and recurrence times of the recorded acoustic emission events. We define friction as the ratio of shear to normal stress, assuming cohesion is negligible. The assumption of zero cohesion is reasonable because the experiments were performed at room conditions (<75% relative humidity) and the starting particles were relatively large; thus there were no significant attractive forces between them. Because the normal stress was set to a constant value for each experiment, friction is equivalent to shear stress. The algorithm described in Chapter 2 was used to calculate the source location of AE events. To calculate the size  $S$  for each AE event we used the following formula:

$$S = \sum_{i=1}^{16} E_s^i \quad (5.1)$$

where  $E_s^i$  is the area under the AE signal  $x(t)$  recorded by the  $i$ -th piezoelectric transducer, and is given by:

$$E_s = \int_0^T |x(t)|^2 dt \quad (5.2)$$

where  $x(t)$  is the time series of voltage, with duration  $T$ . The units of  $E_s$  (and  $S$ ) are  $V^2s$ , therefore dividing it by the characteristic impedance  $Z_0$  of the transducer circuit, which is measured in Ohm, will yield the actual energy in J. Here, we use the size as equivalent to seismic moment, rather than magnitude. We assume that  $Z_0$  does not vary significantly in the range of frequencies of our signals (103 to 106 Hz). The distributions of recurrence times were calculated using the procedure described in Chapter 3. In the rest of the chapter we used catalogs that do not include AE events that occurred during the first 1000 s (approximately  $20^\circ$ ) of shearing, in order to minimize any undesirable effects of initial sample variability (e.g. initial porosity differences due to sample preparation) on AE productivity. Based on the findings of Chapter 2, we assume that  $20^\circ$  of shearing are sufficient to homogenize the sample in that sense.

**Table 5.1:** Table of experiments. Load point velocity for all experiments was  $0.02^\circ/\text{s}$ , which is approximately  $15\ \mu\text{m}/\text{s}$  at the mean radius of the sample. Experiments r086 and r097 from Chapter 2 have been included for comparison. Repeat experiments are shown in the same colors. PS: particle size.  $\sigma_n$ : normal stress.  $\kappa$ : torsional stiffness of the apparatus.  $h_0$ : initial sample height.  $\rho_0$ : initial bulk density of the sample.

Experiment ID	PS range ( $\mu\text{m}$ )	$\sigma_n$ (MPa)	$\kappa$	Sample mass (g)	$h_0$ (mm)	$\rho_0$ (g/cm <sup>3</sup> )
r054	150 - 212	8	high	30.00	4.35	1.7
r080	150 - 212	8	high	30.11	4.41	1.7
r082	150 - 212	8	high	30.15	4.28	1.8
r055	150 - 212	8	low	30.00	4.30	1.7
r068	150 - 212	4	high	30.00	4.41	1.7
r066	150 - 212	4	low	30.00	4.46	1.7
r107	400 - 500	4	high	30.20	4.41	1.7
r114	400 - 500	8	low	30.20	4.41	1.7
r086	400 - 500	8	high	30.20	4.40	1.7
r097	400 - 500	8	high	30.20	4.75	1.6

## 5.4 Results

Table 5.2 lists the maximum load point displacement achieved in each experiment, including r086 and r097 from Chapter 2. Also listed are the number of acoustic emission events recorded during shearing (excluding 1000 s or  $20^\circ$  of the run-in period), as well as their mean rate of occurrence, i.e. the number of events divided by the total amount of time over which they occurred.

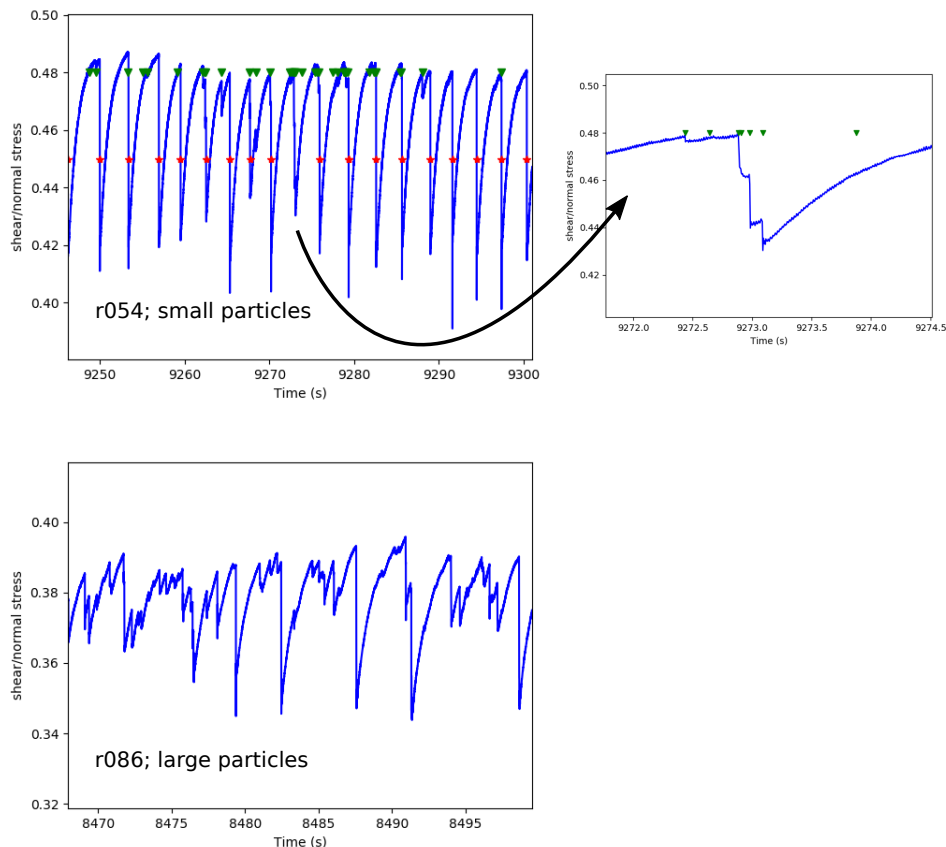


**Figure 5.1:** Friction data from two experiments performed under the same conditions but using different particle size ranges (r054: type A, 150-212  $\mu\text{m}$ ; r086: type B, 400-500  $\mu\text{m}$ ). In the case of r054, red dots represent the timing of AE events with a characteristic size, while all other events are indicated by green inverted triangles (see text). Some stress drops occurred in discrete steps, as shown by the top right graph.

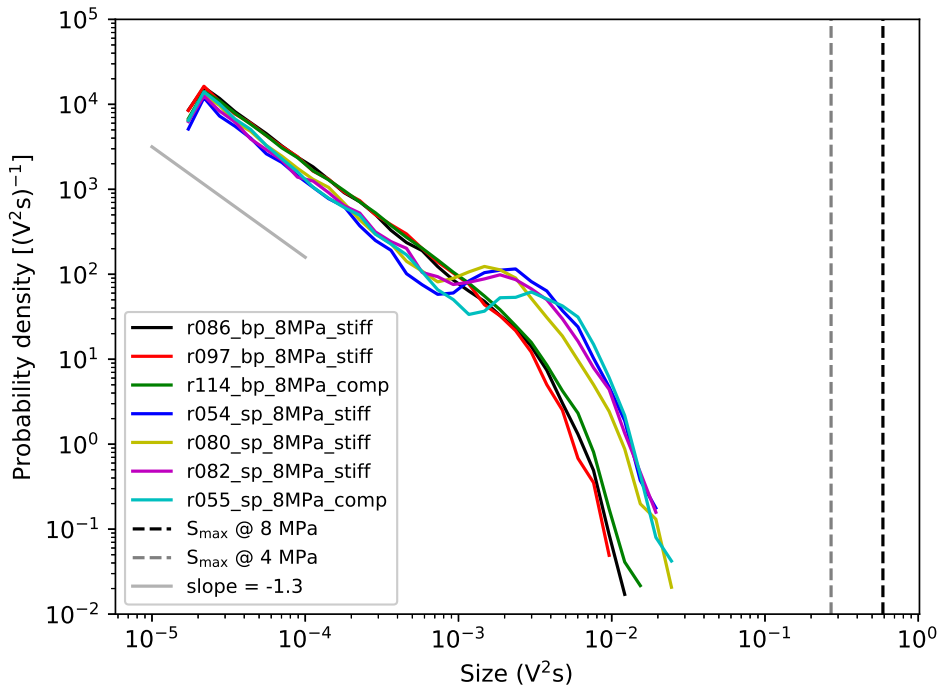


**Figure 5.2:** Probability density distributions of AE sizes recorded in the experiments at 8 MPa normal stress. The grey and black vertical dashed lines represent the estimated size for a total stress drop, assuming that friction is 0.45 and the normal stress is 4 or 8 MPa respectively.

The time series of friction show regular stick-slip with Type A samples (small beads) and irregular stick-slip with type B samples (large beads). Typical examples are shown in Figure 5.1. Our measurements show that stress drops were partial, i.e. the aggregates retained a portion of their strength during slip. In some experiments we observed episodes of strain weakening or hardening. We observed isolated, brief (tens of seconds) periods of atypical activity in both samples, i.e. type A samples occasionally experienced irregular stick-slip, whereas similarly brief periods of regular stick-slip could be observed with type B samples. The greatest variability in the peak frictional strength and stress drop was observed in the experiments using small particles, under 4 MPa normal stress.

For the experiments at 8 MPa, the difference in style of stick-slip between type A and type B samples is clearly reflected in the shape of the probability density distributions of AE event sizes (Figure 5.2). The data shown in Figure

**Table 5.2:** Maximum load point displacement (LPD), number of AE events  $N$  during shearing (excluding the run-in period of 1000 s or  $30^\circ$ ), and mean recurrence rate  $R$ . Also shown are the corrected values of  $N$  and  $R$  after taking into account the size of completeness of the catalogs,  $S_c = 2 \times 10^{-5} V^2 s$ . Repeat experiments are shown in the same colors.

Experiment ID	Maximum LPD ( $^\circ$ ; mm)	$N$	$R$ ( $s^{-1}$ )	$N_{corrected}$	$R_{corrected}$ ( $s^{-1}$ )
r054	193.0; 143.2	10316	1.1	6604	0.7
r080	193.2; 143.3	19048	2.0	7453	0.8
r082	195.4; 144.9	12207	1.3	7414	0.8
r055	195.2; 144.8	13392	1.4	7325	0.8
r068	202.4; 150.1	9201	1.7	5553	0.6
r066	200.3; 148.6	9452	1.0	6239	0.6
r107	229.4; 170.2	8246	0.8	6096	0.6
r114	225.9; 167.6	34040	3.5	22792	2.3
r086	195.0; 144.6	38699	4.1	18260	1.9
r097	222.2; 164.8	48699	5.0	24025	2.5



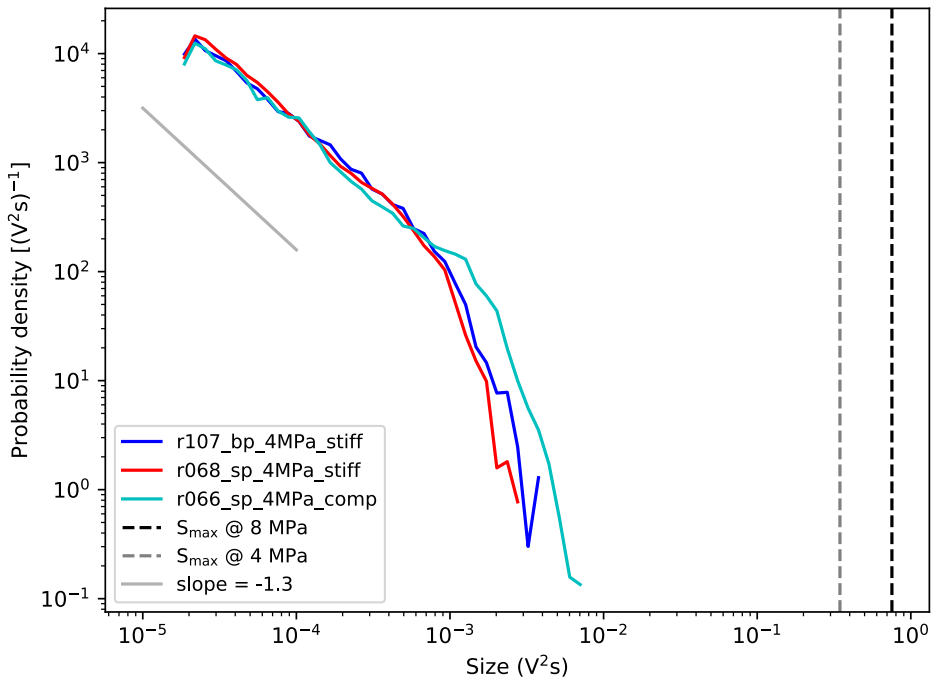


**Figure 5.3:** Probability density distributions of AE sizes recorded in the 4 MPa experiments. The grey and black vertical dashed lines represent the estimated size for a total stress drop, assuming that friction is 0.45 and the normal stress is 4 or 8 MPa respectively.

5.2 have been corrected for catalog completeness, that was estimated to be  $S_c = 2 \times 10^{-5} \text{ V}^2\text{s}$ . Type A samples have a linear, dipping (slope  $\approx -1.3$ ) segment between approximately  $2 \times 10^{-5} \text{ V}^2\text{s}$  and  $4 \times 10^{-4} \text{ V}^2\text{s}$  followed by a distinctive peak. For r055 (compliant configuration) the start of the peak is slightly “delayed” until  $10^{-3} \text{ V}^2\text{s}$ . Comparison between the curves from r054, r082 and r080 (higher sensitivity) shows that the shape of the distributions for sizes less than approximately  $2 \times 10^{-5} \text{ V}^2\text{s}$  is sensitive to catalog completeness, that in turn depends on the trigger settings of the data acquisition system. Overall, the shape of type A distributions is indicative of a mix of characteristic events together with power law distributed smaller size events. The data collapse is notable, considering that it involves experiments performed using the high as well as the low torsional stiffness configuration. Type B samples have a linear, dipping (slope  $\approx -1.3$ ) segment that is truncated at large sizes. The data collapse of r086, r097 (stiff configuration) and r114

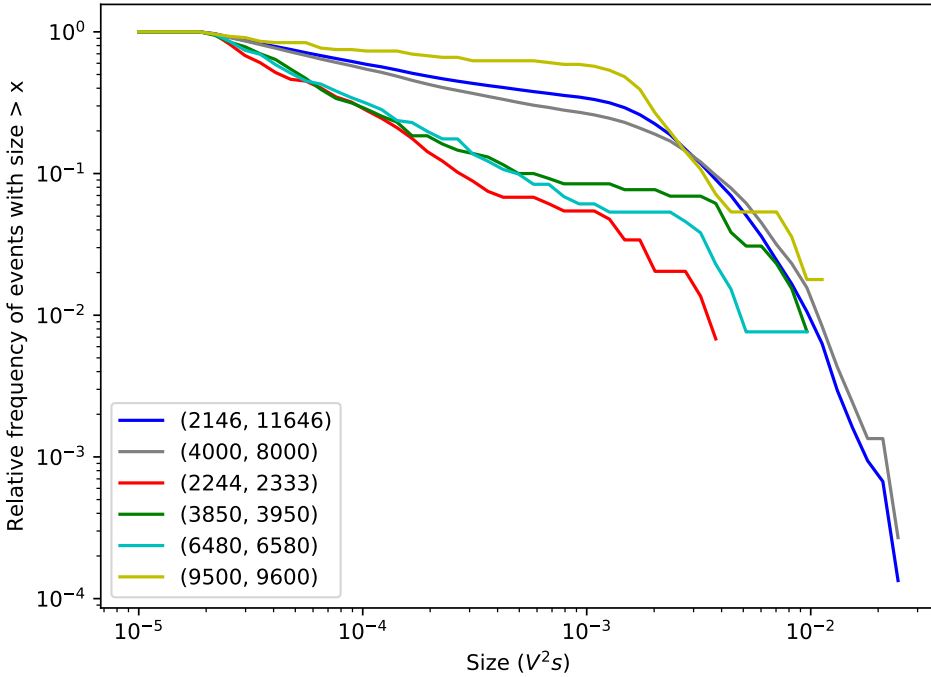


**Figure 5.4:** Complementary cumulative distributions of AE sizes from different time windows from experiment *r080* (type A sample; stiff configuration). The time windows are given in the legend; values in seconds. The blue curve represents the entire shearing period minus run-in. The red curve has a deficit of large size events compared to every other curve.

(compliant configuration) is notable as well. The overall shape of sample B curves indicates catalogs consisting of events with a truncated power law distribution of sizes compared to sample A. Both sample A and B distributions have approximately similar slope values in the size range between  $2 \times 10^{-5}$  V<sup>2</sup>s and  $4 \times 10^{-4}$  V<sup>2</sup>s and a similar cut-off on the right side.

The relative frequency-size distributions of both type A and type B samples sheared at 4 MPa have a linear, dipping (slope  $\sim -1.3$ ) segment that is exponentially truncated at large sizes (Figure 5.3). There is no distinctive peak that would indicate the presence of characteristic events in the catalog. The probability densities scale linearly in the size range between  $2 \times 10^{-5}$  and  $4 \times 10^{-4}$  V<sup>2</sup>s, and with approximately similar slope values as their 8 MPa counterparts.

Figure 5.4 and 5.5 illustrate the point made earlier about occasional mode

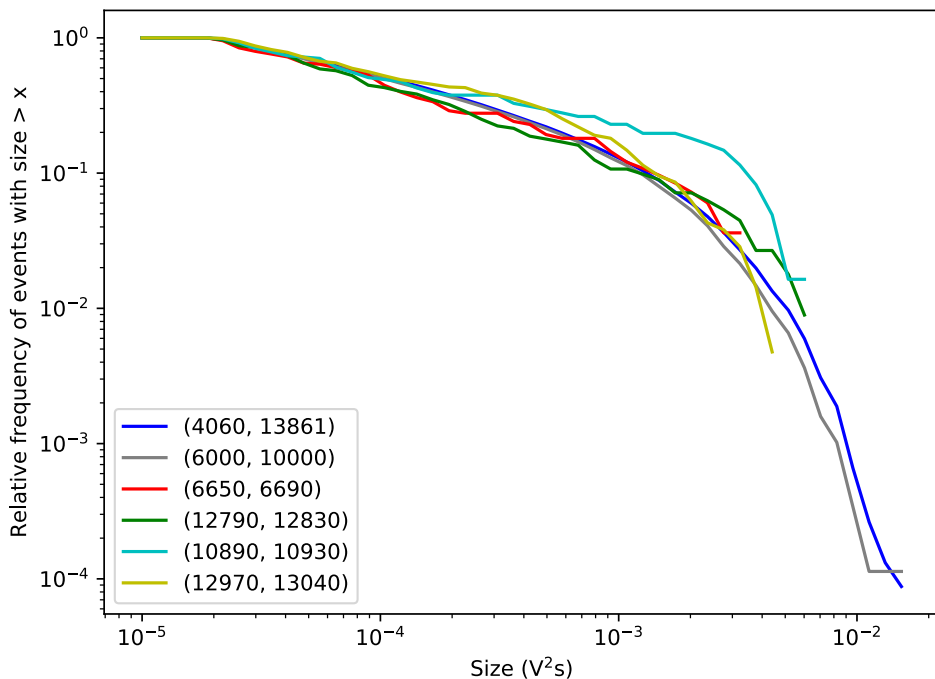


**Figure 5.5:** Complementary cumulative distributions of AE sizes from different time windows from r114 (type B sample; compliant configuration). The time windows are given in the legend; values in seconds. The blue curve represents the entire shearing period minus run-in. The cyan curve has a surplus of large size events compared to the other curves.

switching in the stick-slip behavior, as it is reflected in the complementary cumulative size distributions (CCD) of e.g. experiments r080 (type A sample; stiff configuration) and r114 (type B sample; compliant configuration). We use complementary cumulative instead of probability density distributions due to the small number of events included in the smaller observation periods. The blue curves show the CCDs of the entire shearing periods, minus run-in. In grey, we show the CCDs of a smaller window of observation that more or less matches the blue curve. The rest of the curves show the CCDs of arbitrarily selected, smaller time windows that may or may not show a surplus or deficit of large size events compared to the blue and grey curves. All of the time windows are larger than the adjusted mean rate of occurrence of AEs,  $R_{corrected}$ , listed in Table 5.2.

To determine whether there is clustering of AE source locations, we

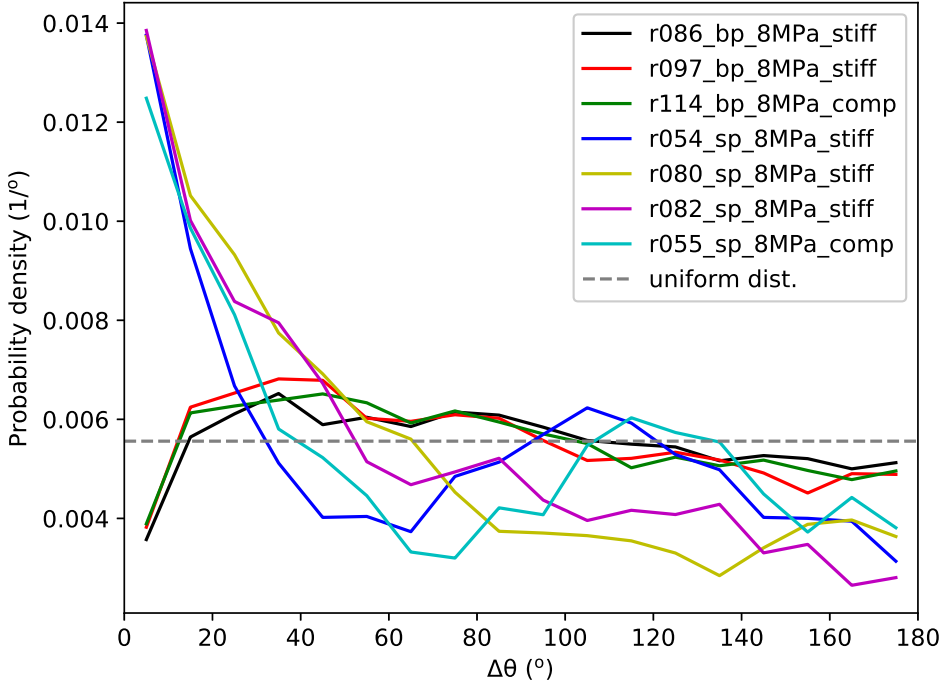


**Figure 5.6:** Probability density distributions of  $\Delta\theta$  for the experiments at 8 MPa normal stress. Bin size is  $10^\circ$ . The gray dashed line shows the probability density of the uniform distribution.

computed the distance  $\Delta\theta = (\theta_{i+1} - \theta_i)$ , in degrees ( $^\circ$ ), between the source locations  $\theta_i$  and  $\theta_{i+1}$  of consecutive AE events  $i$  and  $i + 1$ . Then we calculated the probability density distribution  $P(\Delta\theta)$ . The results vary depending on the sample size distribution and normal stress. At 8 MPa normal stress, type A samples have higher  $P(\Delta\theta)$  for  $\Delta\theta < 20^\circ$  compared to type B samples (Figure 5.6). At 4 MPa normal stress, type A samples show significantly more clustering than type B samples, but for  $\Delta\theta < 45^\circ$  (Figure 5.7). Irrespective of normal stress and apparatus stiffness,  $P(\Delta\theta)$  of type B samples are closer to the probability density of the uniform distribution:

$$P(\Delta\theta) = \begin{cases} \frac{1}{180} \\ 0 \end{cases} \quad (5.3)$$

The probability density distributions of interevent or recurrence time  $\Delta t$  of type A and type B samples at 8 MPa normal stress are strikingly different (Figure 5.8, upper panel). Type A samples show a distinctive peak centered at

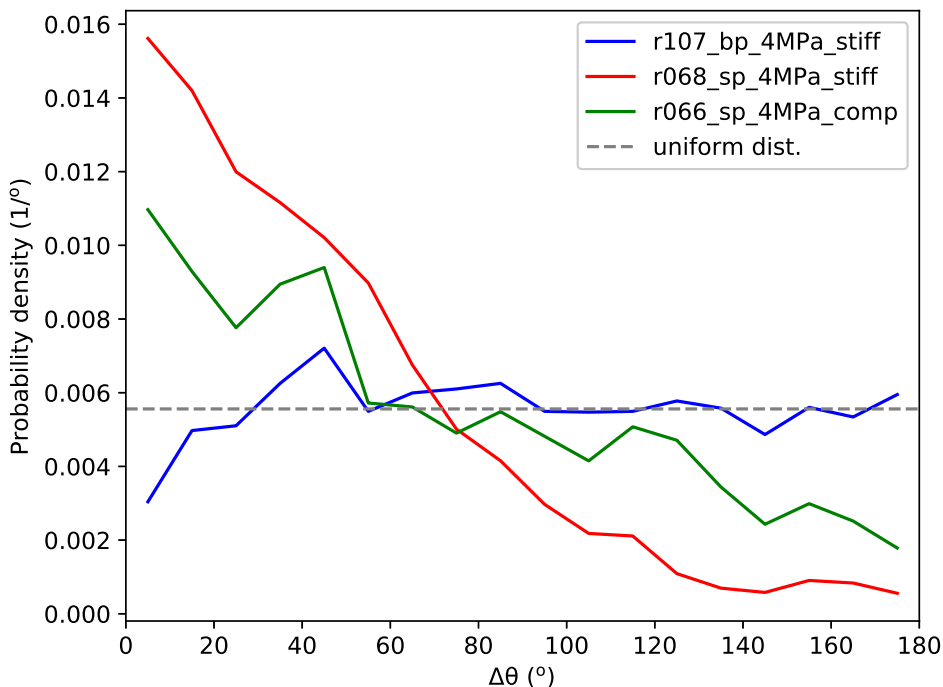


**Figure 5.7:** Probability density distributions of  $\Delta\theta$  for the experiments at 4 MPa normal stress. Bin size is  $10^\circ$ . The gray dashed line shows the probability density of the uniform distribution.

$\Delta t \sim 2.5$  s which appears to be superimposed on a gamma-type distribution. The peak is indicative of a characteristic recurrence interval. Type B samples follow the scaling described in Chapter 3, i.e. a gamma-type distribution. Contrary to type A, the distributions of type B samples do not feature a peak.

There is partial overlap in the probability density distribution of recurrence times for type A and type B samples at 4 MPa normal stress (Figure 5.8, lower panel). The linear segments for  $\Delta t < 10^{-1}$  s have different slopes for sample type A and B. There is some data collapse for  $10^{-1}$  s  $\leq \Delta t \leq 9$  s, regardless of sample type and machine stiffness. A small peak centered at 3 s can be seen in the curves of type A samples.

We did not observe sample extrusion during or after our experiments, which means that the samples remained completely confined. While most particles retained their original size, experiments at 8 MPa normal stress generated more fine particles than those at 4 MPa.

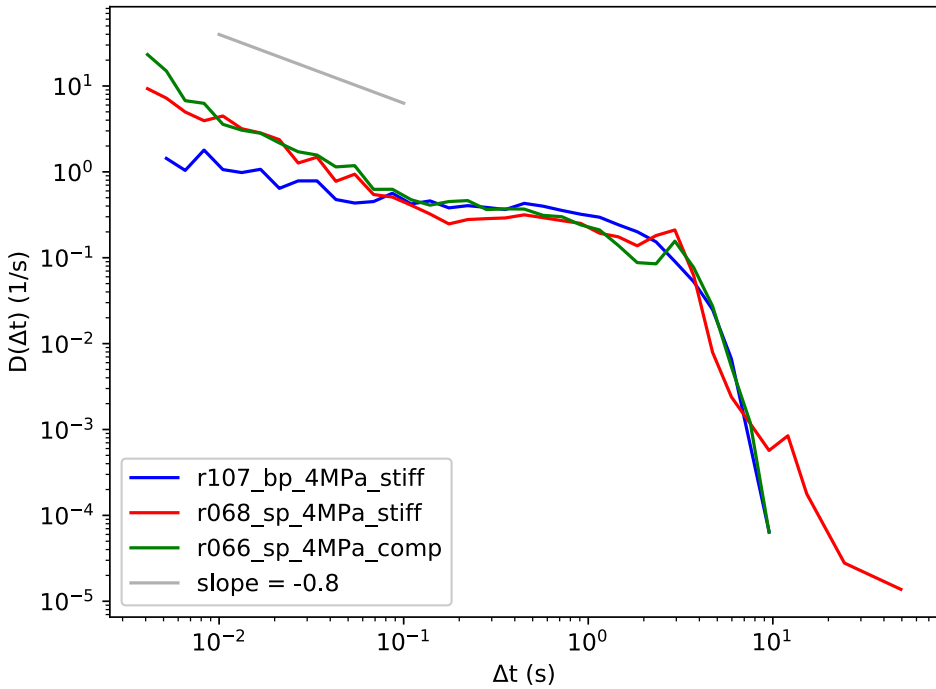
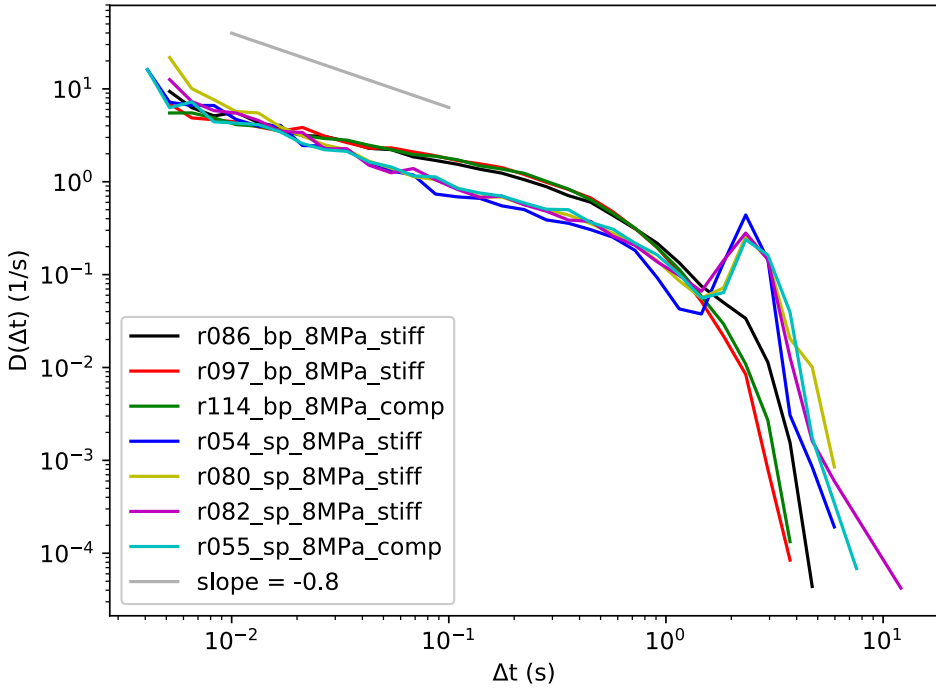


Figure 5.8

**Figure 5.8:** Probability density distributions of recurrence times  $\Delta t$ . "sp": small particles (type A samples). "bp": big particles (type B samples). Upper panel: 8 MPa normal stress. Lower panel: 4 MPa normal stress.

## 5.5 Discussion

The choice between the characteristic earthquake and the Gutenberg-Richter model is critical to the effectiveness of probabilistic seismic hazard analysis maps: it reveals the expectation of the map makers about the rate of large earthquakes. If the characteristic earthquake model is the correct one, but the G-R model is chosen instead, PSHA will underestimate the rate of large earthquakes, perhaps resulting in a costly recovery should a disaster occur. If, however, seismicity follows the G-R law, but the characteristic earthquake model is chosen instead, PSHA will overestimate the rate of large earthquakes, which may result in unnecessary upfront costs for disaster prevention. The complex nature of natural seismicity and geologic faults, combined with the limited instrumental seismicity record, and the limitations of paleoseismology, make it difficult to assess which model is the correct one.

We have studied a mechanical system which exhibits features that are similar to faulting and earthquakes: a frictional interface that produces complex mechanical behavior when loaded at a "slow" constant rate. The data presented in this chapter show that by using smaller particles for the thin granular layer that forms the frictional interface, and choosing an appropriate normal stress value, we can obtain either characteristic event or truncated power law distributions of avalanche sizes, measured by analyzing their acoustic signature. The shape of the distributions is also sensitive to the amount of data available, i.e. the window of observation. Throughout this discussion, our main assumption is that AEs are generated at the nucleation sites of slip instabilities, when sudden displacements, translations, or limited fracturing of particles result in the generation of elastic waves (Chapter 2). Furthermore, we assume that the particles involved in the nucleation of these instabilities are members of force chains, i.e. the load-bearing microstructures in stressed granular media (Jaeger et al., 1996). This is a reasonable assumption because these particles are under the highest amount of stress, compared to spectator particles.

The approximately similar slope of the linear portion of AE size distributions suggests that energy dissipation is self-similar up to  $10^{-3}$  V<sup>2</sup>s, regardless of sample type (A or B) and normal stress (4 or 8 MPa). The

exponent, approximately -1.3, is relatively close to  $-3/2$  that is predicted by mean-field theory (Dahmen et al., 2011) and observed in cellular automata models (Klein et al., 2017). Similar power law scaling of event sizes has been reported by several experimentalists using a variety of sample materials and apparatus (Baró et al., 2013; Dalton and Corcoran, 2001, 2002; Uhl et al., 2015). Extrapolating the scaling of sizes beyond  $10^{-3}$  V<sup>2</sup>s based on the shape of the probability density curves is not trivial, as it would underestimate type A sizes and overestimate type B sizes. The matter is further complicated by the lack of a mechanistically defined maximum possible event size. The absolute upper size limit allowed by the system is equivalent to a complete stress drop. Calculations of the equivalent maximum AE size, assuming an average peak friction value of 0.45 and a constant apparent stiffness at failure, suggest that it is approximately an order of magnitude larger than the observed maximum size (Figure 5.2 and 5.3). This applies to experiments performed at 4 as well as 8 MPa.

Correlations exist not only in the avalanche size domain but also in their recurrence times. Figure 5.8 shows that recurrence times are systematically distributed depending on the particle size distribution used. We submitted the recurrence time data to the analysis described in Chapter 3, by calculating the probability density of  $R\Delta t$ , where  $R$  is the number of events divided by the duration of the time window in which they occurred. The shape of the probability density distributions for type B samples (Figure 5.9, lower panel) is familiar from Chapter 3. It is clearly different from exponential distribution, at least for the 8 MPa experiments, due to the log-log linearly increasing values for  $R\Delta t < 1$ . Overall, the data can be fit by the modified gamma distribution introduced by Corral (2004) and discussed further in Chapter 3. The implication of the type of gamma distribution applicable here is that the hazard rate is highest immediately after an avalanche and decreases with increasing  $R\Delta t$  until it reaches the background rate of the exponential part. This is fundamentally different from what the characteristic earthquake model predicts. Figure 5.9 (upper panel) contains the probability density distributions of  $R\Delta t$  for type A samples. These distributions have three distinctive segments. The first one, for  $R\Delta t < 0.5$  at 8 MPa and  $R\Delta t < 0.2$  at 4 MPa, is linear in log-log space, with a slope of approximately -0.8. This is followed by a second segment which extends up to about  $R\Delta t = 1$ . The third segment is dominated by a prominent peak in probability density at  $R\Delta t = 2$  approximately, followed by a sharp decrease. Experiment r068 does not show a prominent peak and its extreme  $R\Delta t$  values extend further to the right. The data collapse observed in the first segment suggests that the events that fall in this range are similarly correlated, regardless of normal stress and apparatus



stiffness. The main difference between experiments at 4 and 8 MPa is the lower probability density observed for  $0.5 < R\Delta t < 1$  at 8 MPa compared to 4 MPa. The shapes of the complete curves suggest that the distribution of  $R\Delta t$  is in fact a mixture distribution, with one of the underlying distributions being a power law. Further statistical analysis is required to constrain the parameters of the mixture distribution and calculate the hazard function.

Because of the characteristic nature of the size distribution for type A samples, we can compare the features of the size and  $R\Delta t$  PDFs with the mechanical data. Figure 5.1 shows that in the type A sample at 8 MPa, the non-characteristic events (green inverted triangles) occurred primarily during the non-linear portion of the loading curve (recall that friction is proportional to shear stress, and that the normal stress and load point displacement were servo-controlled to constant values), prior to the characteristic slip events (red stars). Therefore these closely spaced, non-characteristic events have power law distributed sizes and  $R\Delta t$ , and are equivalent to what has been observed in experiments using the double-direct configuration (Johnson et al., 2013), as well as in discrete element method simulations (Ferdowsi et al., 2013). Clearly, the peak at  $R\Delta t = 2$  is due to consecutive events that, apparently often, happen to be characteristic in terms of size. The stiffness of the apparatus does not seem to affect the location of the peak on the horizontal axis, which suggests that the system is slip-predictable. The variability seen for  $0.5 < R\Delta t < 1$  at both normal stress levels is probably due to irregularities in the stick-slip cycle. A similar analysis for type B events is riskier, due to the self-similar nature of the avalanche sizes.

Why would samples of one particle size distribution (PSD), namely type A samples, preferentially experience frictional instabilities of a narrow range of sizes and recurrence times, whereas samples of a different PSD, B, generate truncated power law distributed event sizes? Since the sample material is common between type A and type B samples, i.e. soda-lime glass, let us assume that the same physico-chemical mechanisms are operating at the microscale (up to two interacting particles scale) in both cases. Then, the differences between experiments with type A and type B samples are 1. the different number of particles across the layer's thickness, 2. the different initial PSDs, and 3. the relation between mean particle size and piston teeth height and spacing. In the following paragraphs we will examine these in detail.

From the initial PSDs (A: 150-212  $\mu\text{m}$ ; B: 400-500  $\mu\text{m}$ ) we see that the average particle size of B is approximately 2.5 times larger than the average particle in A. Since larger objects are likely to have more weak points than smaller objects, it is possible that type B particles accumulate wear more

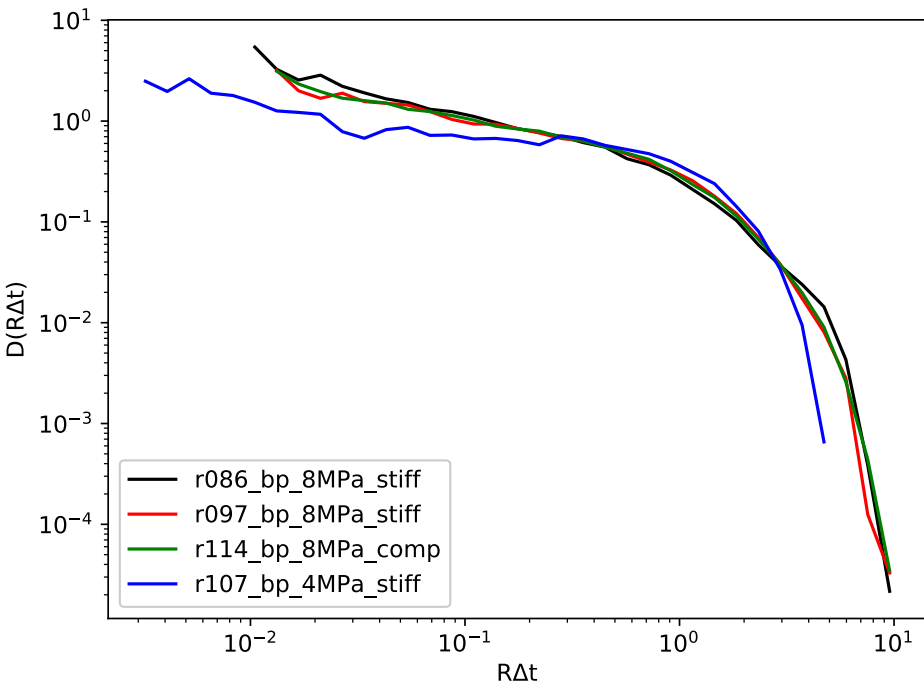
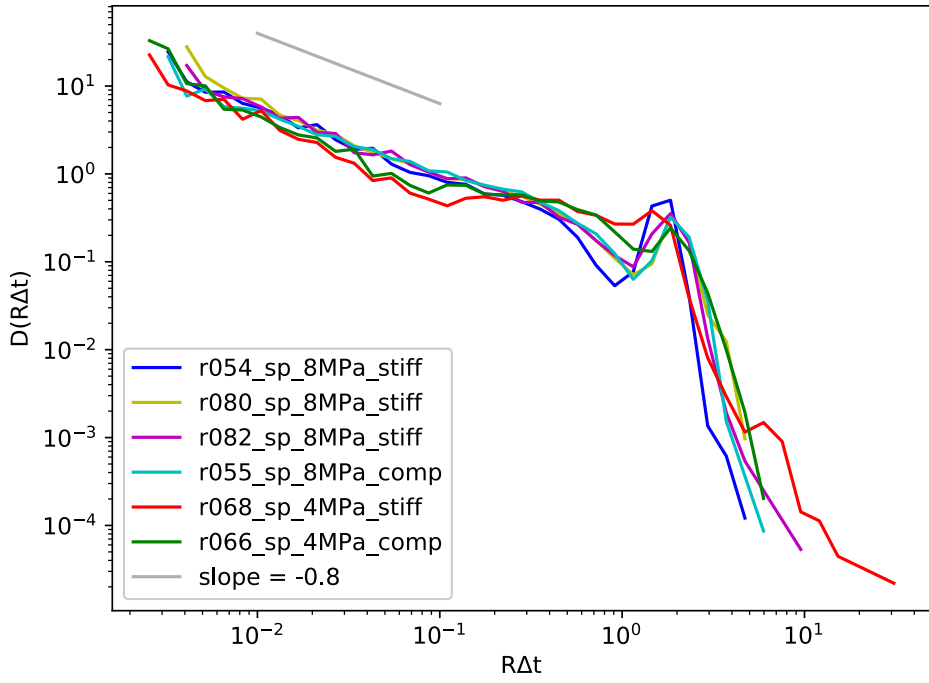


Figure 5.9

**Figure 5.9:** *Probability density distributions of normalized recurrence times  $R\Delta t$ . "sp": small particles (type A samples). "bp": big particles (type B samples). Upper panel: type A samples (180-212  $\mu\text{m}$ ). Lower panel: type B samples (400-500  $\mu\text{m}$ ).*

easily and thus their average strength is lower than that of type A particles. By lowering the threshold for failure via weaker particles, characteristic events (CE) near the system's upper size limit become less likely. If the difference in the probability density distributions (PDF) of type A and B samples in our case was due to differences in particle strength as a function of mean size, we would expect that the CE behavior of type A would be clearly dominant at 4 MPa normal stress also. This is not the case. Note that Sammis et al. (1987) proposed that particle cracking is more prevalent in narrow PSDs, such as ours. However, our experiments were performed under the pervasive fracture threshold for soda-lime glass beads (Mair et al., 2002).

Another possible scenario that could explain the difference in the AE size distributions as a function of mean particle size is related to the packing ratio of the samples. Hayman et al. (2011) observed more quasi-periodic events as a function of increasing solid volume fraction past the jamming transition (Aharonov and Sparks, 1999). This behavior is due to the increase in long range correlations with increasing packing (Howell et al., 1999). It is likely that due to their smaller size, type A beads were able to attain higher packing ratios during shearing compared to the larger type B beads. This could explain why CE behavior was seen only with type A samples and only at 8 MPa normal stress, but not at 4 MPa.

Could the difference be due to the width of the particle size distributions? Sammis et al. (1987) showed theoretically that a self-similar mixture of small and large particles would have a stabilizing effect on force chains by distributing the load more evenly, compared to an arrangement of like sized particles. This idea is supported by DEM simulations on self-similar 2D disks (Morgan and Boettcher, 1999; Morgan, 1999) and laboratory experiments on glass bead gouges (Mair et al., 2002), that showed that stress drop values decrease as a function of increasing PSD width. More specifically, Mair and colleagues observed stick-slip with narrow PSD (105-149  $\mu\text{m}$ ) and stable sliding with 1-800  $\mu\text{m}$  samples under 5 MPa normal stress and load point velocities between 0.1  $\mu\text{m/s}$  and 1000  $\mu\text{m/s}$ . In our case, both type A and type B samples have relatively narrow initial PSDs. Therefore both type A and type B should have exhibited quasi-periodic frictional instabilities at least in the early stages of shearing; however this was not the case.

A third option is that because of the different mean particle size between type A and B samples, the macroscopic behavior is a function of the coupling between the aggregate and the pistons. The piston surfaces have teeth that are approximately 200  $\mu\text{m}$  tall and have irregular spacing of about 0.5 mm on average. Therefore, the valleys' depth between consecutive teeth was comparable in size to the mean particle diameter of type A, but smaller than the mean particle diameter of type B. Anthony and Marone (2005) have shown that increasing the surface roughness of the pistons in a biaxial configuration, by introducing regularly spaced teeth, increased the peak strength of the aggregate, while promoting stick-slip. They suggested that this was due to the emergence of force chains in the case of rough boundaries, as opposed to localized shearing along smooth boundaries. Following the ideas of Anthony and Marone (2005), we believe that type A samples fall in the category of "rough" boundaries, whereas type B samples lie between the "mirror-smooth" and "rough" cases.

Figure 5.6 and 5.7 show that for type A samples, AE source locations tend to cluster, whereas for type B samples that bias is smaller. In Chapter 2 we interpreted AE source locations as the loci of the onset of frictional instabilities. Following this interpretation, type A samples appear to have been prone to forming one or more spatially distinct "asperities". The inferred higher packing fraction of these samples would have been conducive to this. Breaking these asperities could have caused the surplus of characteristic events. Nucleation points of frictional instabilities in type B samples were instead distributed rather evenly. This explanation for the two types of samples could have been the reason for the observed probability densities of AE size (Figure 5.2 and 5.3) and normalized recurrence time (Figure 5.9).

To assess the validity of the ideas described here, it is necessary to have accurate and precise measurements of absolute shear strength and stress drop, which we lack, as discussed in Chapter 2. In some cases, as in Figure 5.1, type A samples appear stronger than type B samples. However we do not discern a systematic behavior across all of our experiments. Accurate measurements of shear stress would allow us to compare our results with other studies. For example, double-direct shear experiments by Anthony and Marone (2005) at 10 MPa normal stress, 10  $\mu\text{m/s}$  load point velocity, and 3 mm initial layer thickness showed that the average stress drop value for 508 – 590  $\mu\text{m}$  size particles was approximately 1.2 MPa, whereas for 105 – 149  $\mu\text{m}$  and 250 – 297  $\mu\text{m}$  size particles approximately 1 MPa. The AE size distributions suggest that at 8 MPa normal stress, type A samples generated larger events than type B samples (Figure 5.2). However the situation at 4 MPa is less clear in that regard (Figure 5.3). Future work on this topic requires constraints

on the effect of normal stress and PSD on the acoustic properties of glass bead aggregates in our experimental configuration. Owens and Daniels (2011) demonstrated that elastic wave propagation is sensitive to the microstructure of granular aggregates.

A striking feature of our experiments is mode switching between characteristic and power law avalanche sizes. Mode switching has been observed in similar experiments involving granular materials (Dalton and Corcoran, 2001; Geller et al., 2015; Hayman et al., 2011), numerical simulations of fault rupture (Ben-Zion and Rice, 1993), and exhumed faults (Williams et al., 2017). It is also predicted by the analytic theory for avalanche statistics proposed by Dahmen et al. (2011) for high packing ratios. Klügel (2005, 2010) argued that in the case of natural seismicity such behavior is due to the stochastic nature of the system; characteristic events are a temporarily “absorbing state”. Regarding this study, mechanistic inferences of the packing and rigidity of the microstructure during shear, such as the one provided earlier, typically fail to explain transient phenomena, such as brief mode switching from regular to irregular stick-slip and vice versa (Figure 5.4 and 5.5). While the end member behaviors can be explained separately, fast (order of  $10^1$  R) transitions between them would also require radical but quickly reversible changes in the microstructure of the samples. Post-mortem visual inspection of the samples show that fine particles were generated during the experiments, likely as a result of abrasive wear (Chapter 2). However the bulk of the sample material remained intact. Therefore, one plausible mechanistic explanation for transient mode switching is that local accumulations of fine particles temporarily dominate, or at least modulate, the interactions between load-bearing particles and thus the macroscopic frictional behavior of the aggregate. “Local” accumulations may be understood either in the sense of a spatially limited heterogeneity in material properties along strike, e.g. a patch of granular aggregate with altered PSD, or in the sense of a layer parallel to the frictional interface, e.g. a boundary shear. We have also considered the possibility that wear material trapped between the sidewalls that provide the sample with lateral support and the forcing pistons may have affected our measurements. However, the seals between the various components that the sample chamber is comprised of were thoroughly lubricated prior to each experiment. Furthermore, these seals were not under significant stress, especially compared to the values of normal stress used in our experiments.

## 5.6 Conclusions

To conclude, we have presented a laboratory system that can produce regular or irregular stick-slip depending on particle size distribution of the sample and the applied normal stress. This system is clearly far removed from the natural conditions prevailing in natural fault zones, in terms of stress, strain rate and chemical composition. Nevertheless, it is a slowly driven system consisting of simple agents (glass particles) that exhibits complex behavior, similar to natural seismicity. Furthermore, the system itself contains a frictional interface, similar to natural faults between two blocks of lithosphere. Our first key finding in relation to natural seismicity is that a single frictional interface can produce either CE or power-law or truncated power law distributed instability sizes. Second, stick-slip behavior can switch, or appear to switch, during limited periods of observation (i.e. comparable to the long-term mean rate of occurrence) for both sample types tested. Taken together, these two results suggest that periods of observation comparable to the long-term rate of occurrence, as is the case with natural fault zones, may very well lead to false impressions about the style of moment release, i.e. Characteristic or Gutenberg-Richter. The frictional strength and stability along a fault will likely change over time, via material wear during earthquakes and via healing during interseismic periods. Therefore we posit that for the purpose of PSHA, the question of whether a particular fault produces Characteristic or Gutenberg-Richter type of seismicity may actually be impossible to answer, unless a method of detecting mode-switching transitions (G-R to CE and vice versa) is discovered.

## 5.7 Supplementary material

We estimated the size of completeness of the our catalogs by examining the left side of the probability density distributions. Figure 5.10 shows the uncorrected data from the experiments performed at 8 MPa (the same procedure was followed for the 4 MPa data). Approaching  $10^{-5}$  V<sup>2</sup>s from the right, r054, r055, r082 (type A), and r114 (type B, compliant) begin to deviate from the linear trend seen in larger sizes. The probability density curves for r086, r097 (type B, stiff), and r080 (type A, increased sensitivity of recording system) deviate from linearity in the next lower decade. Based on this difference we set the size of completeness  $S_c = 2 \times 10^{-5}$  V<sup>2</sup>s (the same value applies to the 4 MPa data as well). Figure 5.2 shows the result after discarding all events with size smaller than  $2 \times 10^{-5}$  V<sup>2</sup>s.

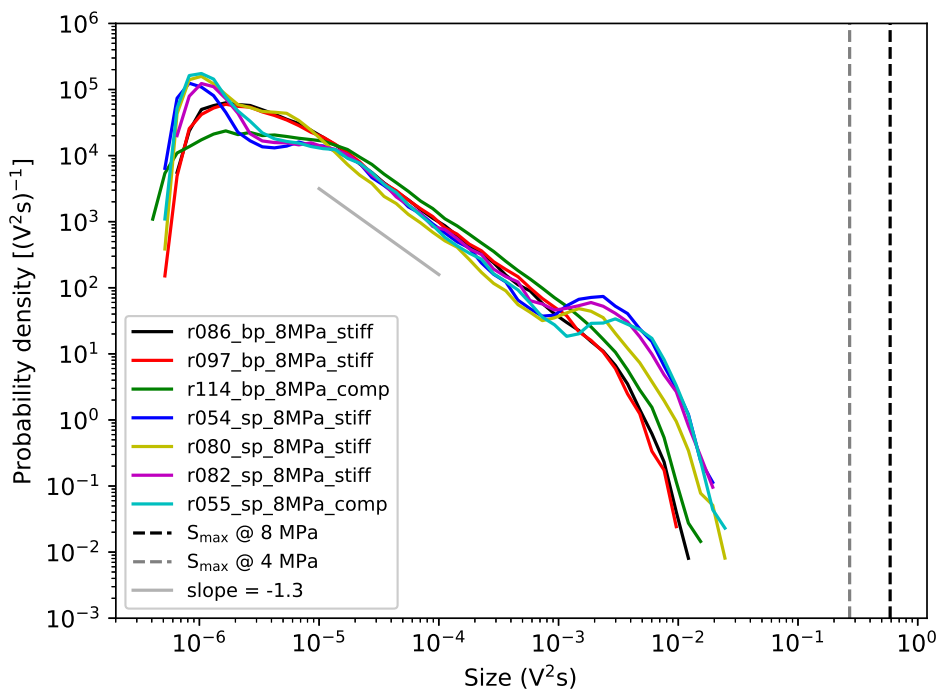


**Figure 5.10:** Probability densities of AE sizes from the experiments at 8 MPa normal stress. "sp": small particles (type A samples). "bp": big particles (type B samples). The data have not been corrected for catalog completeness.





## Chapter 6

# Concluding remarks and outlook

Are the avalanche statistics of sheared granular aggregates sensitive to large shear displacements under elevated normal stress? If yes, what are the mechanisms that cause this sensitivity? The data presented in this thesis extend the envelope of conditions tested experimentally in previous studies up to 8 MPa normal stress and approximately 165 mm of displacement (40 units of shear strain), *simultaneously*. Here we compile the findings of the preceding chapters in order to answer the questions above, and to suggest improvements and topics for further research.

### 6.1 Key findings

As the data from Chapters 2 and 5 show, acoustic emission sizes  $S$  are not randomly distributed; their probability density distribution  $D(S)$  is linear in log-log space over approximately two orders of magnitude. We found that  $D(S) \sim S^k$ , where  $k \approx -1.3$ , which is close to the exponent  $k = -1.5$  obtained from compression or shear experiments on nanocrystals and microcrystals, bulk metallic glasses, rocks, and granular media, and from earthquake catalogs (Uhl et al., 2015). Similar values have been reported in studies employing cellular automata models (Klein et al., 2017). Using smaller particles (150 to 212  $\mu\text{m}$  range instead of 400 to 500  $\mu\text{m}$  range) we measured a surplus of “characteristic” events, i.e. big events of a narrow size range (Chapter 5). The probability density distributions of source location distance between consecutive AE events suggest that the sites where characteristic events nucleate were clustered, whereas the nucleation sites for power law AEs were more evenly distributed (Chapter 5). The clustering of nucleation

points suggests that failure of one or more asperities along the ring-shaped sample could explain the surplus of large size events. Note that in the Olami-Feder-Christensen (OFC) model asperity failures do not coincide with the largest events (Klein et al., 2017). This suggests that characteristic events in the OFC model are not the result of structural heterogeneities alone and that dynamic effects are also in play. This difference between our system and the OFC model shows that the information contained in the scaling of avalanche sizes is not sufficient to explain the underlying mechanisms that produce instabilities.

Several studies (Aharonov and Sparks, 1999; Dahmen et al., 2011; Howell et al., 1999; Uhl et al., 2015) have shown the existence of a critical packing fraction  $\phi_c$  for granular materials; below  $\phi_c$ , the aggregate behaves as a fluid; above  $\phi_c$  it behaves as a solid because the particles jam against each other. In Chapter 3 we showed that the power law exponent of the gamma distribution that describes normalized waiting times increases with increasing normal stress  $\sigma_n$ . The transition from an exponential to a gamma distribution implies the emergence of correlations in the system, likely because of increasing mechanical coupling between particles. In this context, our findings suggest that at  $\sigma_n = 2$  MPa the sample was below  $\phi_c$ ; at  $\sigma_n = 4$  MPa, the samples were at or very close to the jamming transition; and at  $\sigma_n = 8$  MPa above  $\phi_c$ . Higher normal stress results in more abrasive wear and production of fines that help fill the voids between the larger beads, thus increasing the packing fraction. The correlations persist even across remote slices of the samples (Chapter 3). This surprising result allows us to use temporal correlations to infer spatial ones. Nevertheless, the exact nature of the mechanisms that enable such long range interactions remains unknown.

Another prominent feature of our stick-slip data is mode switching, i.e. quasi-periodic, “characteristic” size events to power law distributed sizes and vice versa (Chapter 5). This behavior has been observed in similar studies involving granular media (Dalton and Corcoran, 2001; Hayman et al., 2011). We propose that this phenomenon occurs due to localized, temporary accumulations of fine particles that alter the interactions of the larger particles belonging to the load-bearing framework of the sample. Because of the accumulation of fines in the aggregate, load is distributed over a larger number of particles (Morgan and Boettcher, 1999; Sammis et al., 1987). This would likely decrease the magnitude of stress drop at failure and thus the AE size (Mair et al., 2002). We did not examine whether the frequency of mode-switching increases as a function of shear displacement. Note that with enhanced particle wear, for example via the addition of water as pore fluid (Chapter 4), the size of the frictional instabilities decreases drastically with

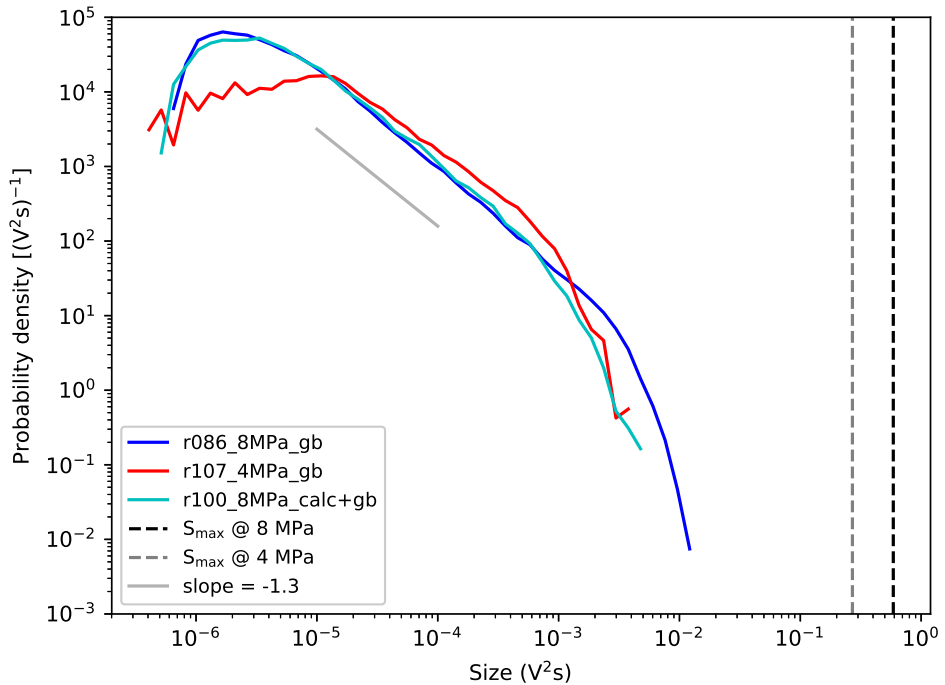


**Figure 6.1:**  $D(S)$  from experiments r086 ( $\sigma_n = 8$  MPa) and r107 ( $\sigma_n = 4$  MPa) from Chapter 5, and r100 ( $\sigma_n = 8$  MPa). For r100, three quarters of the sample annulus (in terms of azimuth) were filled with calcite and the remaining quarter with glass beads, that had the same particle size distribution as r086 and r107. The truncation of  $D(S)$  occurs at a smaller  $S$  for r100 and r107 compared to r086, although for smaller sizes the data from r086 and r100 collapse onto each other. All three experiments were performed using the same rate of rotation ( $0.02$  °/s).

increasing shear displacement.

The right tail of the AE size distributions is truncated as a function of the applied normal stress, which may imply sensitivity to packing fraction (Chapter 5). A similar effect has been observed after removing different fractions of cells from the OFC model (Kazemian et al., 2015). The sensitivity of the truncation (or “cutoff”) size to the packing fraction is predicted by mean-field theory (Dahmen et al., 2011). The truncation is also due to the finite size of the samples. This idea is supported by the preliminary results of experiments using circumferentially varying sample materials, namely a patch of glass beads surrounded by a frictionally stable material such as calcite. As

shown in Figure 6.1, the truncation of  $D(S)$  occurs at larger  $S$  when higher normal stress is applied or when the sample consists of glass beads only.

Based on all of the above, we conclude that the key factor affecting the avalanche statistics of our system is the packing of the glass beads, which is in turn a function of normal stress, wear rate, and particle size distribution.

## 6.2 Contribution to understanding natural seismicity

Natural faults do not consist of glass beads with tightly controlled size range, confined by stiff blocks of steel. Natural strain rates are much slower than what we can reasonably simulate in the laboratory, and the wide range of lithologies and fluid compositions found in the lithosphere give rise to phenomena (Niemeijer et al., 2012) that our system does not capture. How then do the findings of this thesis help improve the practice of seismic hazard assessment and perhaps bring earthquake forecasting and prediction closer to reality?

Starting with the improvement of seismic hazard assessment, a longstanding debate between experts revolves around the applicability of the Characteristic Earthquake and Gutenberg-Richter models to describing seismicity on individual faults. The former model dictates that faults produce earthquakes of a narrow size range at regular, quasi-periodic intervals, while the latter suggests that faults produce a wide range of earthquakes whose sizes are distributed according to a power law (Kagan, 1996; Rong et al., 2003; Wesnousky, 1994). We have shown that the frictional interface in our system can reproduce both models, not only by changing the initial conditions but also “on the fly” during shearing. There is evidence that natural faults too could be prone to mode-switching (Williams et al., 2017). Seismic hazard maps based on the concept of time-dependent seismicity could be seriously affected by the over- or under-estimation of the seismic potential of individual faults (Stein et al., 2012). To overcome this problem, methods for detecting imminent mode-switching should be developed.

Regarding earthquake prediction, the holy grail of seismology, and earthquake forecasting, the contribution of this work lies in understanding the physical mechanisms that produce the correlations we observe in systems at or near a phase transition. This can be achieved in the framework proposed by Uhl et al. (2015). Note that our experiments are not suitable for simulating precursory phenomena, such as Gutenberg-Richter  $b$ -value changes prior to big slip events (Rivière et al., 2018), which would require continuous recording of AE signals so as to produce robust statistics over

individual stick-slip cycles.

## 6.3 Improvements and suggestions

We hope that our findings can serve as guidelines for improvements to the apparatus and the methods developed in the framework of this study, and to motivate further research. The following paragraphs give suggestions to this end.

### 6.3.1 Apparatus improvements

In Chapter 2 we discussed the limitations of the torque measurements. Rethinking the way the measurements are performed is necessary to improve the accuracy and precision of shear stress and friction values. These values are important because they can be used to 1. quantify the amount of energy released during every frictional instability; 2. study the scaling of stress drop and AE size, an important topic in earthquake research (Cocco et al., 2016); 3. measure the stiffness of the apparatus and of the sample. The cause of erroneous torque measurements is the sensitivity of the (compressive) force transducers to off-axis loading (sideloading). In light of this we performed several measurements using a redesigned crosshead that allows the measurement of the force responsible for torque in tension instead of in compression. While this new configuration allows for much more accurate measurement of force, it requires very fine adjustments to ensure even distribution of normal load, as evidenced by the clustering of AE source locations (Figure 6.2).

Energy and stiffness measurements will also benefit from improved measurements of rotation (shear displacement) across the piston rings, rather than at the rotating plate under the bottom piston which is the case now (see section 3.6.5 under Chapter 3). Note that slip and stiffness can be used to calculate the “seismic” moment of an instability, using equation (1.2). Preliminary tests using a digital rotary encoder that measured the relative rotation of the top and bottom pistons have been successful in resolving slip during avalanches.

High sampling rate measurements of sample thickness, closer to the sample, e.g. at the inner part of the ring, can help identify whether the volumetric behavior of the sample changes during episodes of mode-switching. Finally, introducing redundancy to the measurements of forces and displacements will enable safer, quantitative discrimination between apparatus- and sample-response.

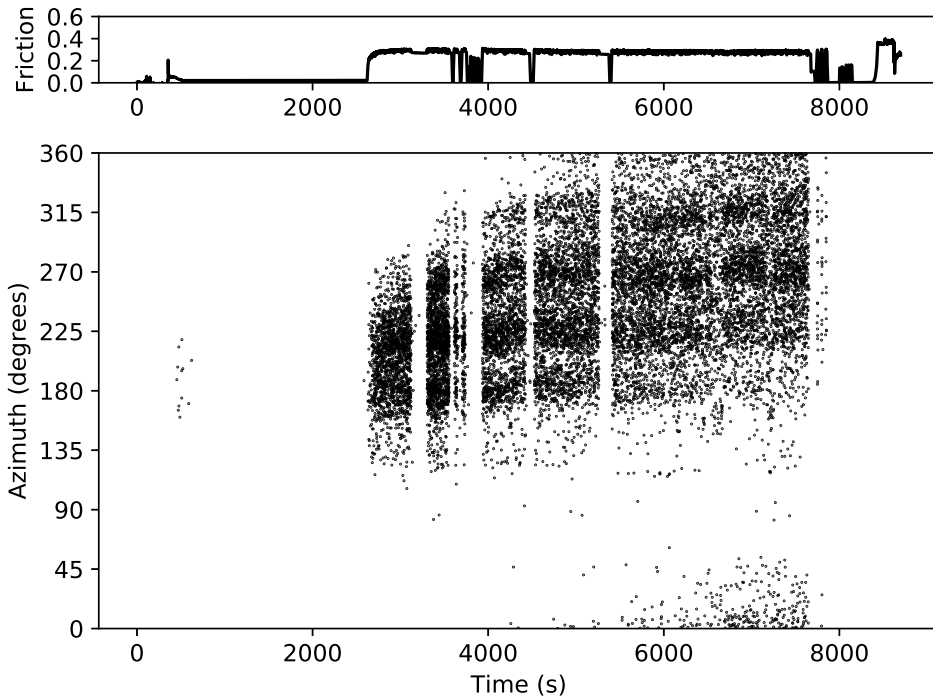


**Figure 6.2:** Friction and AE source locations as a function of time. Data from experiment r163 ( $\sigma_n = 5$  MPa). For this particular experiment, the measurement of reaction torque was performed in tension. The crosshead was arrested from one side only, which resulted in the uneven application of normal load, as evidenced by the clustering of AE source locations in one half of the ring.

### 6.3.2 Method improvements

As shown in Chapter 4, the combination of soda-lime glass beads and water as pore fluid produced undesirable results by suppressing stick-slip. To investigate the mechanical effects of pressurized pore fluids we have proposed the use of alternative pore fluids, such as decane, silicone oil, or dry argon. Using such fluids will help eliminate humidity as a variable. It will also allow the study of phenomena such as locally varying pore pressure and thus effective normal stress, that could alter the mechanical behavior of the aggregate. From the perspective of apparatus capabilities, the results of Chapter 4 suggest that the sample chamber remains watertight during prolonged shearing. Therefore it is suitable for studies on fluid-rock interaction, although rock analogs such

as halite are recommended (Bos et al., 2000; Bos and Spiers, 2002) due to the limitation of room temperature conditions.

Avalanche catalog completeness is important for fitting the right statistical distributions to our data. In the preceding Chapters we have assumed that every AE waveform contains a single event. While this is often the case, there are exceptions. For example in a data block with 5 ms duration, there could be two events, each with a 2 ms duration. Since we measured only one arrival time and maximum amplitude (or size) per waveform, discrepancies could arise. The matter could be complicated even further if some small events have been recorded only by a handful of transducers. Improving the event detection algorithm to account for hitherto ignored events will lower the threshold of catalog completeness. For example, let us consider a block of 16 waveforms recorded after the data acquisition system has been triggered. If the shape of the picked arrival times in a time versus distance plot deviates from the shape one would expect for a signal generated at a point along the sample ring, the block can be flagged for manual inspection, or the automatic picking algorithm can be applied to a time window around the arrival time of the outlier(s). A similar filter can check for whether the maximum amplitude is not within a few hundred microseconds of the picked arrival time, indicating the presence of another event.

The AE size metric used in Chapter 5 can be converted to energy by multiplying the size with the impedance of the transducer, which is a function of frequency. It will then be possible to calculate the amount of energy  $E_r$  radiated as elastic waves in every avalanche. This can be combined with the measurement of the total strain energy  $\Delta W$  released per avalanche (using the measurements of stress drop and slip), to estimate the ratio  $E_r/\Delta W$  known as seismic efficiency  $\eta$  (Madariaga, 2009). The total strain energy is given by the formula (Fulton and Rathbun, 2011):

$$\Delta W = E_f + E_r + E_h \quad (6.1)$$

where  $E_f$  is the amount of energy used to fracture, damage, and translate particles, and  $E_h$  is the amount of energy dissipated as heat. If, for example,  $\eta$  increases gradually during an experiment, then over time less energy will be spent on damaging and displacing particles and generating heat, and more energy will be radiated in the form of elastic waves. Changes in seismic efficiency may allow us to foretell transitions between characteristic and power law event sizes, if transient, localized particle wear is responsible for mode-switching. Independent of this approach, the duration of AE signals could also be used as a measure of event size (Dalton and Corcoran, 2001).

### 6.3.3 Suggestions for further research

Based on the discussion in Chapter 5 about the origins of the regular versus irregular stick-slip as a function of particle size distribution, a series of experiments can be performed to determine the relative contributions of sample thickness (normalized by mean or median particle size) and the shape and pattern of piston teeth. These experiments will also provide a solid basis for comparison with the results obtained using the Double Direct Shear configuration (Anthony and Marone, 2005), considering that the strain rate in the Rotary Shear configuration varies radially.

The truncation of the seismic moment distribution of earthquakes is important because it provides empirical constraints to the maximum expected magnitude. Similarly, the truncation of the AE size and stress drop distributions may hold information about the dynamics of the granular aggregate. As shown in Figure 6.1, preliminary results from experiments on bimaterial samples suggest that the truncation scales with the size of the frictionally unstable patch (glass beads). A systematic investigation of the size, and perhaps number, of glass bead patches will provide more information about the shape of the right tail of the  $D(S)$  distributions.

Quantifying the source properties of AEs could allow us to determine whether the generating mechanisms are dependent on normal stress, particle size distribution, and the presence of a pore fluid other than air. Because of the complex structure of the piston rings and the sample, numerical simulations of wave propagation can be used to help discriminate source from path effects. Figure 6.3 shows an example of a 2D simulation with three acoustic layers (piston-sample-piston), a dipole point source, and 6 point receivers, implemented in SPECFEM2D (Tromp et al., 2008). Progressively more complicated simulations could employ elastic layers for the piston rings and a poroelastic layer for the sample, a (rotated) quadrupole source, receivers with finite aperture, and more realistic structure (even in 3D) for the layers that represent the piston rings. These simulations should be used in combination with the existing knowledge on sound propagation in granular media (Bassett et al., 2012; Langlois and Jia, 2015; Lherminier et al., 2014; Owens and Daniels, 2011; Somfai et al., 2005; Tinti et al., 2016), to enhance the interpretation of laboratory data.

The data presented in this thesis can be used to test other proposed styles of earthquake recurrence, such as the time- and slip-predictable models (Turcotte, 1991; Scholz, 2002). The long-period weakening and strengthening trends as a function of shear displacement, together with the short-period variability of stress drops (e.g. Chapter 2 and 5), suggest that neither of these models is directly applicable to our system, at least under the conditions



tested. A quantitative approach based on conditional probabilities, such as the one used by Corral (2006), can be employed to investigate this matter further. However, accurate measurements of shear stress and slip are essential.

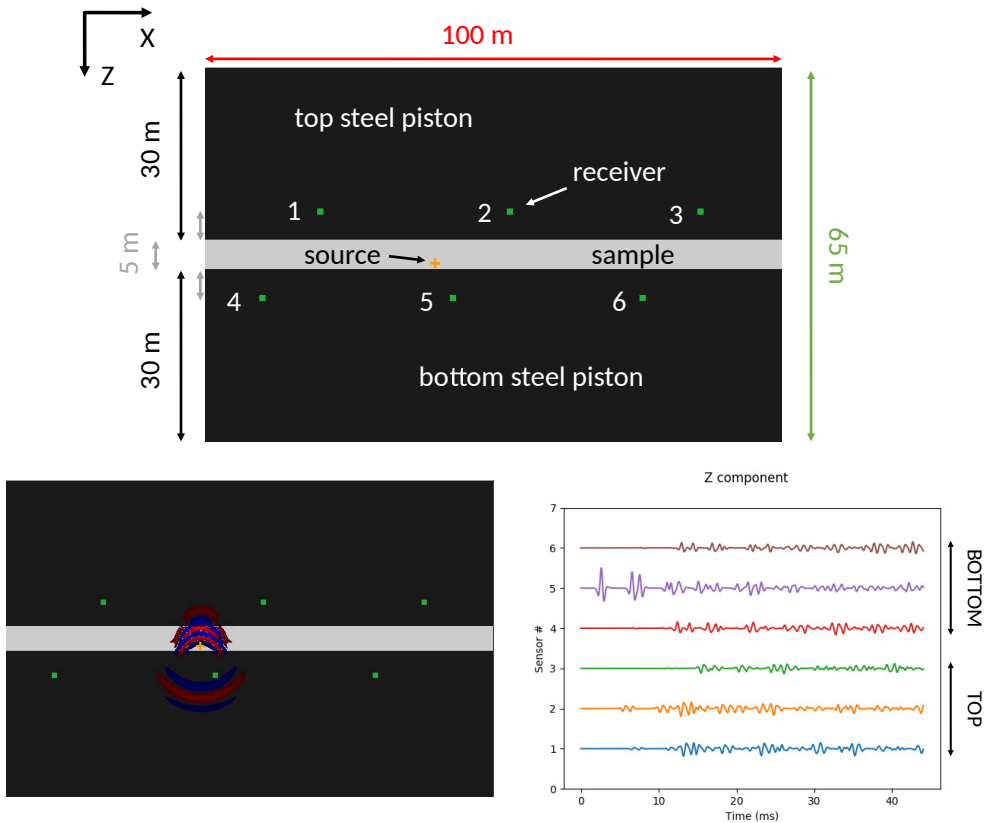


**Figure 6.3:** Example of a 2D numerical model of a small chord of the ring. The black layers represent to the top and bottom piston rings. The gray layer represents the sample. AE transducers are represented by point receivers (green squares). A point source (dipole; 1kHz Ricker wavelet) has been placed inside the sample. For faster computation, the model has been rescaled from millimeters to meters. A snapshot of the displacement wavefield (blue is “down” and red is “up”) is shown on the bottom left panel and the waveforms from the entire simulation on the bottom right panel.

An important open question of practical significance is whether the time of mode-switching can be predicted. This question is difficult to answer for natural faults because existing catalogs of seismicity are short compared to the recurrence interval of the largest earthquakes, and paleoseismological

methods may be inconclusive (Weldon et al., 2004). Therefore, studies on large synthetic catalogs, generated in the laboratory under a wide range of experimental conditions, is a practical alternative, even considering the caveats of simulating nature. This thesis demonstrates that the combination of the rotary shear configuration together with granular aggregates is well suited for this task. The application of tools from statistical mechanics and chaos theory (Martien et al., 1985; Sethna, 2006) to these laboratory-derived catalogs should allow us to extract more information regarding the emergence of spatial and temporal correlations between avalanches.

# References

- Abe, S. and Mair, K. (2009). Effects of gouge fragment shape on fault friction: New 3D modelling results. *Geophysical Research Letters*, 36(23):L23302.
- Aharonov, E. and Sparks, D. (1999). Rigidity phase transition in granular packings. *Physical Review E*, 60(6):6890–6896.
- Aharonov, E. and Sparks, D. (2002). Shear profiles and localization in simulations of granular materials. *Physical Review E - Statistical, Nonlinear, and Soft Matter Physics*, 65(5):1–12.
- Aharonov, E. and Sparks, D. (2004). Stick-slip motion in simulated granular layers. *Journal of Geophysical Research B: Solid Earth*, 109(9):1–12.
- Akaike, H. (1971). Autoregressive model fitting for control. *Annals of the Institute of Statistical Mathematics*, 23(1):163–180.
- Allen, R. V. (1978). Automatic earthquake recognition and timing from single traces. *Bulletin of the Seismological Society of America*, 68(5):1521–1532.
- Anthony, J. L. and Marone, C. (2005). Influence of particle characteristics on granular friction. *Journal of Geophysical Research B: Solid Earth*, 110(8):1–14.
- Bak, P., Christensen, K., Danon, L., and Scanlon, T. (2002). Unified Scaling law for Earthquakes. *Physical Review Letters*, 88(17):10–13.
- Bakun, W. H. and Lindh, A. G. (1985). The Parkfield, California, Earthquake Prediction Experiment. *Science*, 229(4714):619–624.
- Barka, A. (1996). Slip distribution along the North Anatolian fault associated with the large earthquakes of the period 1939 to 1967. *Bulletin of the Seismological Society of America*, 86(5):1238–1254.

- Baró, J., Corral, Á., Illa, X., Planes, A., Salje, E. K. H., Schranz, W., Soto-Parra, D. E., and Vives, E. (2013). Statistical Similarity between the Compression of a Porous Material and Earthquakes. *Physical Review Letters*, 110(8):088702.
- Bassett, D. S., Owens, E. T., Daniels, K. E., and Porter, M. A. (2012). Influence of network topology on sound propagation in granular materials. *Physical Review E - Statistical, Nonlinear, and Soft Matter Physics*, 86(4):1–17.
- Ben-Zion, Y. (2008). Collective behavior of earthquakes and faults: Continuum-discrete transitions, progressive evolutionary changes, and different dynamic regimes. *Reviews of Geophysics*, 46(4):RG4006.
- Ben-Zion, Y. and Rice, J. R. (1993). Earthquake failure sequences along a cellular fault zone in a three-dimensional elastic solid containing asperity and nonasperity regions. *Journal of Geophysical Research: Solid Earth*, 98(B8):14109–14131.
- Ben-Zion, Y. and Rice, J. R. (1995). Slip patterns and earthquake populations along different classes of faults in elastic solids. *Journal of Geophysical Research: Solid Earth*, 100(B7):12959–12983.
- Bocquet, L., Charlaix, E., Ciliberto, S., and Crassous, J. (1998). Moisture-induced ageing in granular media and the kinetics of capillary condensation. *Nature*, 396(6713):735–737.
- Boettcher, M. S. and McGuire, J. J. (2009). Scaling relations for seismic cycles on mid-ocean ridge transform faults. *Geophysical Research Letters*, 36(21):2–6.
- Bommer, J. J. (2002). Deterministic vs. probabilistic seismic hazard assessment: An exaggerated and obstructive dichotomy. *Journal of Earthquake Engineering*, 6(sup001):43–73.
- Bormann, P. (2012). Magnitude calibration formulas and tables, comments on their use and complementary data. In Bormann, P., editor, *New Manual of Seismological Observatory Practice (NMSOP-2)*, pages 1–19. IASPEI, GFZ German Research Centre for Geosciences, Potsdam, 2nd edition.
- Bos, B., Peach, C. J., and Spiers, C. J. (2000). Slip behavior of simulated gouge-bearing faults under conditions favoring pressure solution. *Journal of Geophysical Research: Solid Earth*, 105(B7):16699–16717.

- Bos, B. and Spiers, C. J. (2002). Fluid-assisted Healing Processes in Gouge-bearing Faults: Insights from Experiments on a Rock Analogue System. *Pure and Applied Geophysics*, 159(11-12):2537–2566.
- Brown, S. R., Scholz, C. H., and Rundle, J. B. (1991). A simplified spring-block model of earthquakes. *Geophysical Research Letters*, 18(2):215–218.
- Brzesowsky, R. H., Hangx, S. J. T., Brantut, N., and Spiers, C. J. (2014a). Compaction creep of sands due to time-dependent grain failure: Effects of chemical environment, applied stress, and grain size. *Journal of Geophysical Research: Solid Earth*, 119(10):7521–7541.
- Brzesowsky, R. H., Spiers, C. J., Peach, C. J., and Hangx, S. J. T. (2014b). Time-independent compaction behavior of quartz sands. *Journal of Geophysical Research: Solid Earth*, 119(2):936–956.
- Carlson, J. M. and Langer, J. S. (1989). Mechanical model of an earthquake fault. *Physical Review A*, 40(11):6470–6484.
- Cates, M. E., Wittmer, J. P., Bouchaud, J.-P., and Claudin, P. (1998). Jamming, Force Chains, and Fragile Matter. *Physical Review Letters*, 81(9):1841–1844.
- Chester, F. M. and Chester, J. S. (1998). Ultracataclasite structure and friction processes of the Punchbowl fault, San Andreas system, California. *Tectonophysics*, 295(1-2):199–221.
- Cocco, M., Tinti, E., and Cirella, A. (2016). On the scale dependence of earthquake stress drop. *Journal of Seismology*, 20(4):1151–1170.
- Corral, Á. (2004). Long-Term Clustering, Scaling, and Universality in the Temporal Occurrence of Earthquakes. *Physical Review Letters*, 92(10):108501.
- Corral, Á. (2005). Time-decreasing hazard and increasing time until the next earthquake. *Physical Review E*, 71(1):017101.
- Corral, Á. (2006). Dependence of earthquake recurrence times and independence of magnitudes on seismicity history. *Tectonophysics*, 424(3-4):177–193.
- Dahmen, K. A., Ben-Zion, Y., and Uhl, J. T. (2011). A simple analytic theory for the statistics of avalanches in sheared granular materials. *Nature Physics*, 7(7):554–557.

- Dahmen, K. A., Ertas, D., and Ben-Zion, Y. (1998). Gutenberg-Richter and characteristic earthquake behavior in simple mean-field models of heterogeneous faults. *Physical Review E*, 58(2):1494–1501.
- Dalton, F. and Corcoran, D. (2001). Self-organized criticality in a sheared granular stick-slip system. *Physical Review E*, 63(6):061312.
- Dalton, F. and Corcoran, D. (2002). Basin of attraction of a bounded self-organized critical state. *Physical Review E*, 65(3):031310.
- Daniels, K. E. and Hayman, N. W. (2008). Force chains in seismogenic faults visualized with photoelastic granular shear experiments. *Journal of Geophysical Research*, 113(B11):B11411.
- Davidson, J. and Kwiatek, G. (2013). Earthquake interevent time distribution for induced micro-, nano-, and picoseismicity. *Physical Review Letters*, 110(6):1–5.
- Davidson, J., Stanchits, S., and Dresen, G. (2007). Scaling and universality in rock fracture. *Physical Review Letters*, 98(12):10–13.
- Denisov, D. V., Lörincz, K. A., Uhl, J. T., Dahmen, K. A., and Schall, P. (2016). Universality of slip avalanches in flowing granular matter. *Nature Communications*, 7(1):10641.
- Dorostkar, O., Guyer, R. A., Johnson, P. A., Marone, C., and Carmeliet, J. (2017a). On the micromechanics of slip events in sheared, fluid-saturated fault gouge. *Geophysical Research Letters*, 44(12):6101–6108.
- Dorostkar, O., Guyer, R. A., Johnson, P. A., Marone, C., and Carmeliet, J. (2017b). On the role of fluids in stick-slip dynamics of saturated granular fault gouge using a coupled computational fluid dynamics-discrete element approach. *Journal of Geophysical Research: Solid Earth*, 122(5):3689–3700.
- Engelder, J. T. (1974). Cataclasis and the Generation of Fault Gouge. *Geological Society of America Bulletin*, 85(10):1515.
- Faulkner, D. R., Jackson, C. A., Lunn, R. J., Schlische, R. W., Shipton, Z. K., Wibberley, C. A., and Withjack, M. O. (2010). A review of recent developments concerning the structure, mechanics and fluid flow properties of fault zones. *Journal of Structural Geology*, 32(11):1557–1575.
- Ferdowsi, B., Griffa, M., Guyer, R. A., Johnson, P. A., Marone, C., and Carmeliet, J. (2013). Microslips as precursors of large slip events in the stick-slip dynamics of sheared granular layers: A discrete element model analysis. *Geophysical Research Letters*, 40(16):4194–4198.

- Field, E. H., Jordan, T. H., Page, M. T., Milner, K. R., Shaw, B. E., Dawson, T. E., Biasi, G. P., Parsons, T., Hardebeck, J. L., Michael, A. J., Weldon, R. J., Powers, P. M., Johnson, K. M., Zeng, Y., Felzer, K. R., van der Elst, N., Madden, C., Arrowsmith, R., Werner, M. J., and Thatcher, W. R. (2017). A Synoptic View of the Third Uniform California Earthquake Rupture Forecast (UCERF3). *Seismological Research Letters*, 88(5):1259–1267.
- Fisher, D. S., Dahmen, K. A., Ramanathan, S., and Ben-Zion, Y. (1997). Statistics of Earthquakes in Simple Models of Heterogeneous Faults. *Physical Review Letters*, 78(25):4885–4888.
- Fowler, C. M. R. (2004). *The Solid Earth*. Cambridge University Press, Cambridge, 2nd edition.
- François, D., Pineau, A., and Zaoui, A. (2013). *Mechanical Behaviour of Materials Vol 2*.
- Frank, S. A. (2009). The common patterns of nature. *Journal of Evolutionary Biology*, 22(8):1563–1585.
- Frank, S. A. (2014). How to Read Probability Distributions as Statements about Process. *Entropy*, 16(11):6059–6098.
- Fulton, P. M. and Rathbun, A. P. (2011). Experimental constraints on energy partitioning during stick-slip and stable sliding within analog fault gouge. *Earth and Planetary Science Letters*, 308(1-2):185–192.
- Furlong, K. P. and Herman, M. (2017). Reconciling the deformational dichotomy of the 2016 M<sub>w</sub> 7.8 Kaikoura New Zealand earthquake. *Geophysical Research Letters*, 44(13):6788–6791.
- Geller, D. A., Ecke, R. E., Dahmen, K. A., and Backhaus, S. (2015). Stick-slip behavior in a continuum-granular experiment. *Physical Review E*, 92(6):060201.
- Geller, R. J. (1997). Predictable publicity. *Astronomy & Geophysics*, 38(1):16–18.
- Godet, M. (1990). Third-bodies in tribology. *Wear*, 136(1):29–45.
- Goebel, T. H., Becker, T. W., Schorlemmer, D., Stanchits, S., Sammis, C., Rybacki, E., and Dresen, G. (2012). Identifying fault heterogeneity through mapping spatial anomalies in acoustic emission statistics. *Journal of Geophysical Research: Solid Earth*, 117(3):1–18.

- Goodfellow, S. D. and Young, R. P. (2014). A laboratory acoustic emission experiment under in situ conditions. *Geophysical Research Letters*, 41(10):3422–3430.
- Grosse, C. U. and Ohtsu, M. (2008). *Acoustic emission testing: Basics for Research-Applications in Civil Engineering*.
- Guo, Y. and Morgan, J. K. (2007). Fault gouge evolution and its dependence on normal stress and rock strength—Results of discrete element simulations: Gouge zone properties. *Journal of Geophysical Research*, 112(B10):B10403.
- Hainzl, S., Scherbaum, F., and Beauval, C. (2006). Estimating Background Activity Based on Interevent-Time Distribution. *Bulletin of the Seismological Society of America*, 96(1):313–320.
- Hamilton, T. and McCloskey, J. (1997). Breakdown in power-law scaling in an analogue model of earthquake rupture and stick-slip. *Geophysical Research Letters*, 24(4):465–468.
- Hangx, S. J. T. and Brantut, N. (2019). Micromechanics of High-Pressure Compaction in Granular Quartz Aggregates. *Journal of Geophysical Research: Solid Earth*.
- Hanks, T. C. and Kanamori, H. (1979). A moment magnitude scale. *Journal of Geophysical Research B: Solid Earth*, 84(B5):2348–2350.
- Hayman, N. W., Ducloué, L., Foco, K. L., and Daniels, K. E. (2011). Granular Controls on Periodicity of Stick-Slip Events: Kinematics and Force-Chains in an Experimental Fault. *Pure and Applied Geophysics*, 168(12):2239–2257.
- Hill, D. P. (2008). Dynamic Stresses, Coulomb Failure, and Remote Triggering. *Bulletin of the Seismological Society of America*, 98(1):66–92.
- Howell, D., Behringer, R. P., and Veje, C. (1999). Stress Fluctuations in a 2D Granular Couette Experiment: A Continuous Transition. *Physical Review Letters*, 82(26):5241–5244.
- Jaeger, H. M., Nagel, S. R., and Behringer, R. P. (1996). Granular solids, liquids, and gases. *Reviews of Modern Physics*, 68(4):1259–1273.
- Jiang, Y., Wang, G., and Kamai, T. (2017). Acoustic emission signature of mechanical failure: Insights from ring-shear friction experiments on granular materials. *Geophysical Research Letters*, 44(6):2782–2791.



- Johnson, P. A., Ferdowsi, B., Kaproth, B. M., Scuderi, M., Griffa, M., Carmeliet, J., Guyer, R. A., Le Bas, P.-Y., Trugman, D. T., and Marone, C. (2013). Acoustic emission and microslip precursors to stick-slip failure in sheared granular material. *Geophysical Research Letters*, 40(21):5627–5631.
- Johnson, P. A., Savage, H., Knuth, M., Gomberg, J., and Marone, C. (2008). Effects of acoustic waves on stick-slip in granular media and implications for earthquakes. *Nature*, 451(7174):57–60.
- Kagan, Y. Y. (1993). Statistics of characteristic earthquakes. *Bulletin of the Seismological Society of America*, 83(1):7–24.
- Kagan, Y. Y. (1994). Observational evidence for earthquakes as a nonlinear dynamic process. *Physica D: Nonlinear Phenomena*, 77(1-3):160–192.
- Kagan, Y. Y. (1996). Comment on "The Gutenberg-Richter or Characteristic Earthquake Distribution, Which is it?" by Steven G. Wesnousky. *Bulletin of the Seismological Society of America*, 86(1A):274–285.
- Kagan, Y. Y. and Jackson, D. D. (1991a). Long-Term Earthquake Clustering. *Geophysical Journal International*, 104(1):117–134.
- Kagan, Y. Y. and Jackson, D. D. (1991b). Seismic Gap Hypothesis: Ten years after. *Journal of Geophysical Research: Solid Earth*, 96(B13):21419–21431.
- Kagan, Y. Y. and Jackson, D. D. (1995). New seismic gap hypothesis: Five years after. *Journal of Geophysical Research: Solid Earth*, 100(B3):3943–3959.
- Kagan, Y. Y. and Jackson, D. D. (1999). Worldwide doublets of large shallow earthquakes. *Bulletin of the Seismological Society of America*, 89(5):1147–1155.
- Kagan, Y. Y. and Jackson, D. D. (2013). Tohoku Earthquake: A Surprise? *Bulletin of the Seismological Society of America*, 103(2B):1181–1194.
- Kagan, Y. Y., Jackson, D. D., and Geller, R. J. (2012). Characteristic Earthquake Model, 1884-2011, R.I.P. *Seismological Research Letters*, 83(6):951–953.
- Kanamori, H. and Brodsky, E. E. (2004). The physics of earthquakes. *Reports on Progress in Physics*, 67(8):1429–1496.
- Kazemian, J., Dominguez, R., Tiampo, K. F., and Klein, W. (2015). Spatial Heterogeneity in Earthquake Fault-Like Systems. *Pure and Applied Geophysics*, 172(8):2167–2177.

- King, G. C. P., Stein, R. S., and Lin, J. (1994). Static stress changes and the triggering of earthquakes. *Bulletin of the Seismological Society of America*, 84(3):935–953.
- Klein, W., Gould, H., Tiampo, K. F., Silva, J. B., Gu, T., Kazemian, J., Serino, C., and Rundle, J. B. (2017). Statistical Mechanics Perspective on Earthquakes. In Salje, E., Saxena, A., and Planes, A., editors, *Avalanches in Functional Materials and Geophysics. Understanding Complex Systems.*, pages 1–18. Springer, Cham.
- Klügel, J.-U. (2005). Reply to the comment on J.U. Klügel’s: “Problems in the application of the SSHAC probability method for assessing earthquake hazards at Swiss nuclear power plants,” in *Engineering Geology*, vol. 78, pp. 285–307, by Lomnitz, by J.U. Klügel. *Engineering Geology*, 82(1):74–75.
- Klügel, J.-U. (2008). Seismic Hazard Analysis — Quo vadis? *Earth-Science Reviews*, 88(1-2):1–32.
- Klügel, J.-U. (2010). Comment on “Is There a Basis for Preferring Characteristic Earthquakes over a Gutenberg-Richter Distribution in Probabilistic Earthquake Forecasting” by Tom Parsons and Eric L. Geist. *Bulletin of the Seismological Society of America*, 100(2):896–897.
- Küperkoch, L., Meier, T., Lee, J., and Friederich, W. (2010). Automated determination of P-phase arrival times at regional and local distances using higher order statistics. *Geophysical Journal International*, 181(2):1159–1170.
- Lamb, S., Arnold, R., and Moore, J. D. P. (2018). Locking on a megathrust as a cause of distributed faulting and fault-jumping earthquakes. *Nature Geoscience*, 11(11):871–875.
- Langlois, V. and Jia, X. (2015). Sound pulse broadening in stressed granular media. *Physical Review E - Statistical, Nonlinear, and Soft Matter Physics*, 91(2):1–8.
- Lei, X. and Ma, S. (2014). Laboratory acoustic emission study for earthquake generation process. *Earthquake Science*, 27(6):627–646.
- Lherminier, S., Planet, R., dit Vehel, V. L., Simon, G., Vanel, L., Måløy, K. J., and Ramos, O. (2019). Continuously Sheared Granular Matter Reproduces in Detail Seismicity Laws. *Physical Review Letters*, 122(21):218501.

- Lherminier, S., Planet, R., Simon, G., Vanel, L., and Ramos, O. (2014). Revealing the structure of a granular medium through ballistic sound propagation. *Physical Review Letters*, 113(9):1–5.
- Liu, C. h., Nagel, S. R., Schecter, D. A., Coppersmith, S. N., Majumdar, S., Narayan, O., and Witten, T. A. (1995). Force Fluctuations in Bead Packs. *Science*, 269(5223):513–515.
- Lockner, D. (1993). The role of acoustic emission in the study of rock fracture. *International Journal of Rock Mechanics and Mining Sciences & Geomechanics Abstracts*, 30(7):883–899.
- Lorenz, E. N. (1963). Deterministic Nonperiodic Flow. *Journal of the Atmospheric Sciences*, 20(2):130–141.
- Losert, W., Géminard, J.-C., Nasuno, S., and Gollub, J. P. (2000). Mechanisms for slow strengthening in granular materials. *Physical Review E*, 61(4):4060–4068.
- Luen, B. and Stark, P. B. (2012). Poisson tests of declustered catalogues. *Geophysical Journal International*, 189(1):691–700.
- Madariaga, R. (2009). Earthquake Scaling Laws. *Encyclopaedia of Complexity and System Science*, pages 364–382.
- Main, I. (1996). Statistical physics, seismogenesis, and seismic hazard. *Reviews of Geophysics*, 34(4):433–462.
- Mair, K. and Abe, S. (2008). 3D numerical simulations of fault gouge evolution during shear: Grain size reduction and strain localization. *Earth and Planetary Science Letters*, 274(1-2):72–81.
- Mair, K., Frye, K. M., and Marone, C. (2002). Influence of grain characteristics on the friction of granular shear zones. *Journal of Geophysical Research: Solid Earth*, 107(B10):ECV 4–1–ECV 4–9.
- Mair, K. and Hazzard, J. F. (2007). Nature of stress accommodation in sheared granular material: Insights from 3D numerical modeling. *Earth and Planetary Science Letters*, 259(3-4):469–485.
- Mair, K., Marone, C., and Young, R. P. (2007). Rate Dependence of Acoustic Emissions Generated during Shear of Simulated Fault Gouge. *Bulletin of the Seismological Society of America*, 97(6):1841–1849.

- Majmudar, T. S. and Behringer, R. P. (2005). Contact force measurements and stress-induced anisotropy in granular materials. *Nature*, 435(7045):1079–1082.
- Mandl, G., Jong, L. N. J., and Maltha, A. (1977). Shear zones in granular material. *Rock Mechanics Felsmechanik Mecanique des Roches*, 9(2-3):95–144.
- Martien, P., Pope, S., Scott, P., and Shaw, R. (1985). The chaotic behavior of the leaky faucet. *Physics Letters A*, 110(7-8):399–404.
- Marzocchi, W. and Zechar, J. D. (2011). Earthquake Forecasting and Earthquake Prediction: Different Approaches for Obtaining the Best Model. *Seismological Research Letters*, 82(3):442–448.
- McGuire, J. J. (2008). Seismic Cycles and Earthquake Predictability on East Pacific Rise Transform Faults. *Bulletin of the Seismological Society of America*, 98(3):1067–1084.
- McGuire, J. J., Collins, J. A., Gouédard, P., Roland, E., Lizarralde, D., Boettcher, M. S., Behn, M. D., and van der Hilst, R. D. (2012). Variations in earthquake rupture properties along the Gofar transform fault, East Pacific Rise. *Nature Geoscience*, 5(5):336–341.
- Michlmayr, G., Cohen, D., and Or, D. (2012). Sources and characteristics of acoustic emissions from mechanically stressed geologic granular media - A review. *Earth-Science Reviews*, 112(3-4):97–114.
- Molchan, G. (2005). Interevent Time Distribution in Seismicity: A Theoretical Approach. *Pure and Applied Geophysics*, 162(6-7):1135–1150.
- Morgan, J. K. (1999). Numerical simulations of granular shear zones using the distinct element method: 2. Effects of particle size distribution and interparticle friction on mechanical behavior. *Journal of Geophysical Research: Solid Earth*, 104(B2):2721–2732.
- Morgan, J. K. (2004). Particle dynamics simulations of rate- and state-dependent frictional sliding of granular fault gouge. *Pure and Applied Geophysics*, 161(9-10):1877–1891.
- Morgan, J. K. and Boettcher, M. S. (1999). Numerical simulations of granular shear zones using the distinct element method: 1. Shear zone kinematics and the micromechanics of localization. *Journal of Geophysical Research: Solid Earth*, 104(B2):2703–2719.

- Mulargia, F., Stark, P. B., and Geller, R. J. (2017). Why is Probabilistic Seismic Hazard Analysis (PSHA) still used? *Physics of the Earth and Planetary Interiors*, 264:63–75.
- Nakamura, Y., Muto, J., Nagahama, H., Shimizu, I., Miura, T., and Arakawa, I. (2012). Amorphization of quartz by friction: Implication to silica-gel lubrication of fault surfaces. *Geophysical Research Letters*, 39(21):1–6.
- Nasuno, S., Kudrolli, A., and Gollub, J. P. (1997). Friction in granular layers: Hysteresis and precursors. *Physical Review Letters*, 79(5):949–952.
- Niemeijer, A., Di Toro, G., Griffith, A. W., Bistacchi, A., Smith, S. A., and Nielsen, S. (2012). Inferring earthquake physics and chemistry using an integrated field and laboratory approach. *Journal of Structural Geology*, 39:2–36.
- Nocedal, J., Wright, S. J., and SpringerLink (Online service). (2006). *Numerical Optimization*.
- Owens, E. T. and Daniels, K. E. (2011). Sound propagation and force chains in granular materials. *EPL (Europhysics Letters)*, 94(5):54005.
- Parsons, T., Console, R., Falcone, G., Murru, M., and Yamashina, K. (2012). Comparison of characteristic and Gutenberg-Richter models for time-dependent  $M \geq 7.9$  earthquake probability in the Nankai-Tokai subduction zone, Japan. *Geophysical Journal International*, 190(3):1673–1688.
- Parsons, T. and Geist, E. L. (2009). Is There a Basis for Preferring Characteristic Earthquakes over a Gutenberg-Richter Distribution in Probabilistic Earthquake Forecasting? *Bulletin of the Seismological Society of America*, 99(3):2012–2019.
- Parsons, T., Geist, E. L., Console, R., and Carluccio, R. (2018). Characteristic Earthquake Magnitude Frequency Distributions on Faults Calculated From Consensus Data in California. *Journal of Geophysical Research: Solid Earth*, 123(12):2018JB016539.
- Radjai, F., Wolf, D. E., Jean, M., and Moreau, J.-J. (1998). Bimodal Character of Stress Transmission in Granular Packings. *Physical Review Letters*, 80(1):61–64.
- Ritter, J. E., Huseinovic, A., Chakravarthy, S. S., and Lardner, T. J. (2000). Subcritical Crack Growth in Soda-Lime Glass under Mixed-Mode Loading. *Journal of the American Ceramic Society*, 83(8):2109–2111.

- Rivière, J., Lv, Z., Johnson, P. A., and Marone, C. (2018). Evolution of b-value during the seismic cycle: Insights from laboratory experiments on simulated faults. *Earth and Planetary Science Letters*, 482:407–413.
- Ronchetti, C., Lindqvist, M., Louter, C., and Salerno, G. (2013). Stress-corrosion failure mechanisms in soda–lime silica glass. *Engineering Failure Analysis*, 35:427–438.
- Rong, Y., Jackson, D. D., and Kagan, Y. Y. (2003). Seismic gaps and earthquakes. *Journal of Geophysical Research: Solid Earth*, 108(B10).
- Rossi, M., Vidal, O., Wunder, B., and Renard, F. (2007). Influence of time, temperature, confining pressure and fluid content on the experimental compaction of spherical grains. *Tectonophysics*, 441(1-4):47–65.
- Rundle, J. B., Turcotte, D. L., Shcherbakov, R., Klein, W., and Sammis, C. (2003). Statistical physics approach to understanding the multiscale dynamics of earthquake fault systems. *Reviews of Geophysics*, 41(4):1019.
- Saichev, A. and Sornette, D. (2007). Theory of earthquake recurrence times. *Journal of Geophysical Research: Solid Earth*, 112(4):1–26.
- Sammis, C., King, G., and Biegel, R. (1987). The kinematics of gouge deformation. *Pure and Applied Geophysics PAGEOPH*, 125(5):777–812.
- Savage, J. C. (1993). The Parkfield prediction fallacy. Technical Report 1.
- Scholz, C. H. (2002). *The Mechanics of Earthquakes and Faulting*. Cambridge University Press, Cambridge, 2nd edition.
- Scholz, C. H. (2015). On the Stress Dependence of the Earthquake b-value. *Geophysical Research Letters*, 10964:1399–1402.
- Schwartz, D. P. and Coppersmith, K. J. (1984). Fault behavior and characteristic earthquakes: Examples from the Wasatch and San Andreas Fault Zones. *Journal of Geophysical Research: Solid Earth*, 89(B7):5681–5698.
- Scuderi, M. M., Carpenter, B. M., Johnson, P. A., and Marone, C. (2015). Poromechanics of stick-slip frictional sliding and strength recovery on tectonic faults. *Journal of Geophysical Research: Solid Earth*, 120(10):6895–6912.
- Scuderi, M. M., Carpenter, B. M., and Marone, C. (2014). Physicochemical processes of frictional healing: Effects of water on stick-slip stress drop and

- friction of granular fault gouge. *Journal of Geophysical Research: Solid Earth*, 119(5):4090–4105.
- Sethna, J. P. (2006). Crackling Noise and Avalanches: Scaling, Critical Phenomena, and the Renormalization Group. *Les Houches Summer School Proceedings*, 85:257–288.
- Sethna, J. P., Dahmen, K. A., and Myers, C. R. (2001). Crackling noise. *Nature*, 410(6825):242–250.
- Shcherbakov, R., Turcotte, D. L., and Rundle, J. (2015). Complexity and Earthquakes. In *Treatise on Geophysics*, volume 4, pages 627–653. Elsevier.
- Shi, X., Wang, Y., Liu-Zeng, J., Weldon, R. J., Wei, S., Wang, T., and Sieh, K. (2017). How complex is the 2016 M<sub>w</sub> 7.8 Kaikoura earthquake, South Island, New Zealand? *Science Bulletin*, 62(5):309–311.
- Snieder, R. and van Eck, T. (1997). Earthquake prediction: a political problem? *Geologische Rundschau*, 86(2):446–463.
- Somfai, E., Roux, J.-N., Snoeijer, J. H., van Hecke, M., and van Saarloos, W. (2005). Elastic wave propagation in confined granular systems. *Physical Review E*, 72(2):021301.
- Sornette, D. and Sornette, A. (1999). General theory of the modified Gutenberg–Richter law for large seismic moments. *Bulletin of the Seismological Society of America*, 89(4):1121–1130.
- Stark, P. B. (1997). Earthquake prediction: the null hypothesis. *Geophysical Journal International*, 131(3):495–499.
- Stein, R. S. (1995). Characteristic or haphazard? *Nature*, 378(6556):443–444.
- Stein, S. and Friedrich, A. M. (2014). How much can we clear the crystal ball? *Astronomy & Geophysics*, 55(2):2.11–2.17.
- Stein, S., Geller, R., and Liu, M. (2011). Bad Assumptions or Bad Luck: Why Earthquake Hazard Maps Need Objective Testing. *Seismological Research Letters*, 82(5):623–626.
- Stein, S., Geller, R. J., and Liu, M. (2012). Why earthquake hazard maps often fail and what to do about it. *Tectonophysics*, 562-563:1–25.
- Stein, S., Spencer, B. D., and Brooks, E. M. (2015). Metrics for Assessing Earthquake-Hazard Map Performance. *Bulletin of the Seismological Society of America*, 105(4):2160–2173.

- Stirling, M. W. (2014). The Continued Utility of Probabilistic Seismic-Hazard Assessment. In *Earthquake Hazard, Risk and Disasters*, pages 359–376. Elsevier.
- Swafford, L. and Stein, S. (2007). Limitations of the short earthquake record for seismicity and seismic hazard studies. In *Special Paper 425: Continental Intraplate Earthquakes: Science, Hazard, and Policy Issues*, volume 2425, pages 49–58. Geological Society of America.
- Tinti, E., Scuderi, M. M., Scognamiglio, L., Di Stefano, G., Marone, C., and Collettini, C. (2016). On the evolution of elastic properties during laboratory stick-slip experiments spanning the transition from slow slip to dynamic rupture. *Journal of Geophysical Research: Solid Earth*, 121(12):8569–8594.
- Toksöz, M. N., Shakal, A. F., and Michael, A. J. (1979). Space-time migration of earthquakes along the North Anatolian fault zone and seismic gaps. *Pure and Applied Geophysics PAGEOPH*, 117(6):1258–1270.
- Tranquillo, J. (2019). *An Introduction to Complex Systems*. Springer International Publishing, Cham.
- Tromp, J., Komatitsch, D., and Liu, Q. (2008). Spectral-element and adjoint methods in seismology. *Communications in Computational Physics*, 3(1):1–32.
- Turcotte, D. L. (1991). Earthquake Prediction. *Annual Review of Earth and Planetary Sciences*, 19(1):263–281.
- Turcotte, D. L. and Schubert, G. (2002). *Geodynamics*. Cambridge University Press, Cambridge, 2nd edition.
- Uhl, J. T., Pathak, S., Schorlemmer, D., Liu, X., Swindeman, R., Brinkman, B. A., LeBlanc, M., Tsekenis, G., Friedman, N., Behringer, R., Denisov, D., Schall, P., Gu, X., Wright, W. J., Hufnagel, T., Jennings, A., Greer, J. R., Liaw, P. K., Becker, T., Dresen, G., and Dahmen, K. A. (2015). Universal Quake Statistics: From Compressed Nanocrystals to Earthquakes. *Scientific Reports*, 5:1–10.
- Utsu, T. (2002). Statistical features of seismicity. In *International Geophysics*, pages 719–732.
- Utsu, T., Ogata, Y., S, R., and Matsu'ura (1995). The Centenary of the Omori Formula for a Decay Law of Aftershock Activity. *Journal of Physics of the Earth*, 43(1):1–33.



- van den Ende, M., Chen, J., Ampuero, J.-P., and Niemeijer, A. (2018). A comparison between rate-and-state friction and microphysical models, based on numerical simulations of fault slip. *Tectonophysics*, 733(December 2017):273–295.
- Wang, Z. (2011). Seismic Hazard Assessment: Issues and Alternatives. *Pure and Applied Geophysics*, 168(1-2):11–25.
- Weldon, R. J. (2005). Past and Future Earthquakes on the San Andreas Fault. *Science*, 308(5724):966–967.
- Weldon, R. J., Scharer, K., Fumal, T., and Biasi, G. (2004). Wrightwood and the earthquake cycle: What a long recurrence record tells us about how faults work. *GSA Today*, 14(9):4.
- Wesnowsky, S. G. (1994). The Gutenberg-Richter or characteristic earthquake distribution, which is it? *Bulletin of the Seismological Society of America*, 84(6):1940–1959.
- Wiederhorn, S. M. (1967). Influence of Water Vapor on Crack Propagation in Soda-Lime Glass. *Journal of the American Ceramic Society*, 50(8):407–414.
- Wiederhorn, S. M. and Bolz, L. (1970). Stress Corrosion and Static Fatigue of Glass. *Journal of the American Ceramic Society*, 53(10):543–548.
- Wiederhorn, S. M., Freiman, S. W., Fuller, E. R., and Simmons, C. J. (1982). Effects of water and other dielectrics on crack growth. *Journal of Materials Science*, 17(12):3460–3478.
- Williams, R. T., Goodwin, L. B., Sharp, W. D., and Mozley, P. S. (2017). Reading a 400,000-year record of earthquake frequency for an intraplate fault. *Proceedings of the National Academy of Sciences*, 114(19):4893–4898.
- Wolfson-Schwehr, M., Boettcher, M. S., McGuire, J. J., and Collins, J. A. (2014). The relationship between seismicity and fault structure on the Discovery transform fault, East Pacific Rise. *Geochemistry, Geophysics, Geosystems*, 15(9):3698–3712.
- Youngs, R. R. and Coppersmith, K. J. (1985). Implications of fault slip rates and earthquake recurrence models to probabilistic seismic hazard estimates. *Bulletin of the Seismological Society of America*, 75(4):939–964.
- Zaliapin, I. and Ben-Zion, Y. (2013). Earthquake clusters in southern California II: Classification and relation to physical properties of the crust. *Journal of Geophysical Research: Solid Earth*, 118(6):2865–2877.

- Zaliapin, I., Gabrielov, A., Keilis-Borok, V., and Wong, H. (2008). Clustering Analysis of Seismicity and Aftershock Identification. *Physical Review Letters*, 101(1):018501.
- Zhang, H., Thurber, C., and Rowe, C. (2003). Automatic P-wave arrival detection and picking with multiscale wavelet analysis for single-component recordings. *Bulletin of the Seismological Society of America*, 93(5):1904–1912.
- Zhang, X. and Spiers, C. (2005). Compaction of granular calcite by pressure solution at room temperature and effects of pore fluid chemistry. *International Journal of Rock Mechanics and Mining Sciences*, 42(7-8):950–960.

# Acknowledgements

I would like to begin by thanking André Niemeijer for the fantastic opportunity that he gave me, by recruiting me as a member of his SEISMIC team. While the contents of this thesis deviate from the original goals of the project, André's ideas can still be traced to the core of every single chapter. Jeannot Trampert has been a major source of motivation and support throughout these past few years. Among other things, his advice and enthusiasm helped me produce chapters 2, 3, and 5. Chris Spiers' contribution was invaluable with regard to tackling various scientific and technical challenges, particularly in chapters 2 and 4. Also, he went out of his way to support me during the final months of producing this thesis.

Several members of the research staff eagerly lent their expertise during various stages of my PhD project. Colin Peach helped me deal with many of the technical issues that arose in the process of making accurate measurements in the laboratory. Hanneke Paulssen and Peter Fokker helped me streamline the AE source location procedure, which is perhaps the main "software" innovation of this study. Luca Urpi and George Marketos contributed ideas to technical aspects of data reduction and processing. I am also indebted to Ivan Vasconcelos, who eagerly introduced me to the exciting field of imaging. Suzanne Hangx, Hans de Bresser, Arwen Deuss, Wim Spakman, and Jean-Paul Ampuero provided useful advice on various topics during the lab's weekly meetings, seismo-seminars, or private conversations. I thank Hans for his advice on teaching matters too.

I relied heavily on the work of the permanent technical and support staff of the HPT laboratory and of the Seismology group. Eimert de Graaff designed and built the elements that make up the original AE monitoring system. Thony van der Gon Netscher built pretty much everything else that was needed to start (and keep) doing experiments. Floris van Oort and Gerard Kuijpers joined the team later on, but their contributions were no less important than those of Eimert and Thony. Floris designed and built numerous critical mechanical parts throughout the last 2 years of the project. Gerard designed and built several electronic components that

greatly improved data collection. He also maintained the original AE hardware. Eimert, Gerard, Gert Kastelein, Han de Witte, and Henk van der Meer produced various components that I used to calibrate the AE monitoring system and perform ultrasound measurements. Peter van Krieken helped with some post-mortem sample analyses. Theo van Zessen provided IT support for running numerical simulations of wave propagation on the STIG. Magda Mathot-Martens oversaw the acquisition of the necessary scientific equipment and materials. Magda's role in the smooth operation of the lab, both in terms of practical matters but also in terms of people and morale, cannot be overstated. I would like to thank all of these people for their support and their invaluable contributions to my work, but also for creating a welcoming environment.

A big part of what made the past few years unforgettable was the presence of many talented, funny, nice to hang out with, and all-round interesting people (not that the individuals mentioned hitherto lack any of these qualities) such as: Martijn van den Ende, Ronald Pijnenburg, Mariska Schimmel, Luuk Hunfeld, Loes Buijze, Dawin Baden, Elisenda Bakker, Bart Verberne, Jianye Chen, Tim Wolterbeek, Sabine den Hartog, Zahra Amirzada, Wen Zhou, Maartje Houben, Maartje Hamers, Hadi Mehranpour, Yuntao Ji, Aditya Singh, Svenja Waldmann, Jeroen van Stappen, Anastasia Papaioannou, Nawaz Muhammad, Amin Karamnejad, Caspar Sinn, Piercarlo Giacomel, Anne Pluymakers, Miao Zhang, Nienke Blom, Suzanne Atkins, Maria Koroni, Simon Schneider, Sujania Talavera Soza, Arie van Wettum, Lisanne Jagt, Fatemeh Akbarashrafi, Elmer Ruigrok, Laura Cobden, Haorui Peng, Haydar Karaoglu, Yanadet Sripanich, Andrew Valentine, Agnieszka Plonka, Menno Fraters, Anne Glerum, Claudia Giese, Paul Mason, Pete PcPhee, Markus Ohl, Oliver Plümper, Helen King, Dan Palcu and many others. While I'm at it, I should also thank the 2018-19 AFC Ajax XI for the unforgettable times they offered me during the final months of writing this thesis. Floris and Ronald can relate.

Finally, I would like to thank my family for their love and support throughout the years.

# Curriculum Vitae

Born in Athens, Greece, on the 24<sup>th</sup> of March 1986.

## Education

2013 MS Geology

University of New Hampshire, Durham, NH, United States

2011 Undergraduate degree in Geology

National and Kapodistrian University of Athens, Greece